SCUOLA
NORMALE
SUPERIORE

TESI DI PERFEZIONAMENTO IN NEUROSCIENZE

ANNO ACCADEMICO 2019/2020

# NEW INSIGHTS INTO CREATINE TRANSPORTER DEFICIENCY SYNDROME:

## From the characterization of the mouse model of the pathology to the development of a pharmacological preclinical trial.

Candidato: Francesco Cacciante

Relatore: Tommaso Pizzorusso

# SUMMARY

# 1. INTRODUCTION

## 1.1 PHYSIOLOGY OF CREATINE AND ITS TRANSPORTER

### 1.1.1 Creatine Biochemistry

Creatine (Cr) is an organic compound with many physiologic functions. In particular, Cr is essential in energy metabolism acting as transient intracellular storage of high-energy phosphates and as a shuttle for high-energy phosphate bonds from the sites of production (mitochondria, glycolysis) to the sites of consumption inside the cells. The enzyme creatine kinase (CK), indeed, catalyses the following reversible enzymatic reaction (Fig. 1):

$$Cr + ATP \leftrightarrow PCr + ADP$$

The mitochondrial form of CK phosphorylates Cr to PCr reducing the ATP/ADP ratio and allowing ATP synthase to continue its work. Then, PCr is used in the cytoplasm at sites of high metabolic requirement. Here, high energy phosphates are transferred to convert ADP into ATP and dephosphorylated Cr produced in this last process diffuses back to mitochondria completing the creatine cycle. Cr and PCr, as molecules, are smaller and less negatively charged compared to ATP or ADP; these properties allow the reaching of higher concentration and then a more efficient flux of high-energy phosphates in cells strongly relying upon Cr cycle[1].

The major share of creatine (and phosphocreatine) in the human body is found in muscle, up to 30 mM. The brain, as expected by its metabolic rate, contains a concentration of creatine of about 10 mM[1]

Many other functions of Cr have been described. First, it is an osmolyte and has antioxidant and anti-apoptotic effects[2]. This work will highlights many other functions Cr exerts in the brain; the energy-buffer function exerted by Cr in the brain is in fact pivotal for the correct development of cognitive functions, neurovascular coupling and the correct maintenance of EEG rhythms. Moreover, the release of Cr into the synaptic

cleft has been observed[3], and a putative role as neuromodulator or even as true neurotransmitter has been envisaged, as suggested by the observation that in rat brain slices Cr was released in an action-potential dependent manner, abolished removing Ca++ from perfusion medium or blocking Na+ channels, and enhanced when K+ channels were blocked instead[3] .

### 1.1.2 Creatine Biosynthesis

In physiological conditions, Cr is obtained by diet and endogenous synthesis[4]. The synthesis of Cr is a two-step reaction requiring the amino acids arginine (Arg) and glycine (Gly) as initial reagents. The enzyme L-arginine:glycine amidinotransferase (AGAT) transfers the amidino group of Arg to Gly in order to produce L-ornithine and guanidinoacetic acid (GAA). In the second step, the enzyme S-adenosyl-L-methionine:N-guanidinoacetate methyltransferase methylates the amidino group of GAA to yield Cr (Fig. 2)[4].

Despite the seeming simplicity of the Cr cycle, the biochemical picture is complicated by the fact that many tissues seem to lack one of the enzymes involved in the synthesis of Cr. In most mammalian species, the kidney expresses high levels of AGAT and low levels of GAMT, while the liver contains low levels of AGAT and high amounts of GAMT. At the opposite sides of the spectrum, we have common laboratory mammals, such as rats and mice, which seem to be devoid of AGAT activity in the liver, and monkeys and humans that, in turn, show high amounts of AGAT in the liver as well[1]. Thus, the following outline about Cr synthesis in mammals has been proposed: the kidney would be the main site of GAA production; this metabolite is then transported through blood to the liver where it is methylated to Cr (Fig. 3). Eventually, Cr is again transported by blood and distributed to all tissues.

Cr and PCr are non-enzimatically converted into creatinine, which diffuses out of the cells and is excreted by the kidneys into the urine. By this catabolic pathway about 1.7% of the total creatine pool of the body is lost every day and needs to be replaced[1].

### 1.1.3 Creatine Transporter

Cr is a hydrophilic molecule requiring an active transport system to cross the plasmatic membranes. For this purpose, a cellular membrane Cr transporter (CrT) exists that is responsible for a saturable Na+ and Cl- dependent uptake into cells against a large concentration gradient[5].

The CrT is encoded by the *Slc6a8* gene that in humans is located on Xq28. The gene is made up of 13 exons, with a predicted protein of 635 amino acids and a molecular mass of 70.5 kDa[6].

Like the other members of the SLC6 family, CrT consists of 12 transmembrane domains, containing sites for N-glycosylation and several sites for phosphorylation.

In humans, CrT is expressed predominantly in muscle, kidney and heart, and also in many other tissues including the brain[7]. This pattern of expression reflects the high levels of creatine in muscle and heart, as well as the important role of kidney in the creatine reuptake from urine[6].

CrT is expressed in many regions of the brain, particularly in the olfactory bulb, cerebellum, hippocampus, cortex and several brainstem nuclei[8]. CrT expression is found in both neurons and glial cells, and a recent transcriptional analysis led to the discovery that CrT is highly expressed in fast-spiking neurons parvalbumin-positive inhibitory interneurons[9]. However, the results about glial cells are still debated. In some studies, CrT results to be expressed in oligodendrocytes but not in astrocytes[10], whereas other authors found expression in astrocytes as well[11].

According to in vitro studies of rat hippocampal neurons, CrT is mainly expressed in dendrites and in some axon terminals[12]; this localization can be explained by the high energy requirements for re-establishing the ion electrochemical gradients disrupted during neuronal signaling but also for its envisaged role as neurotransmitter. Evidence was found of the presence of CrT in synaptosomal membrane, which would precisely be the expected place where CrT should be found if Cr were secreted as neurotransmitter[13].

### 1.1.4 Brain Creatine Supplying

Brain is a highly energy demanding organ, despite representing just 2% of the total body weight, and it spends most of its energy demand to maintain the transmembrane ionic gradient and neurotransmission[14]. It is general consensus that most, if not all, Cr supplied to the brain is of peripheral origin[1] and synthetized by the two-step process described above. However, recent findings shows that both AGAT and GAMT are expressed in brain cells[15,16], thus suggesting that endogenous Cr biosynthesis is somewhat present in the brain. A confirmation of this hypothesis is represented by the observation that rats and mice fed with 3-guanidinopropionic acid (GPA), a competitive inhibitor of Cr entry into cells, showed a marked decrease of Cr and PCr contents in heart and skeletal muscle, but only little effect in the brain[17]. However approximately only 12% of brain cells possess the entire biosynthetic pathway (AGAT+GAMT) and approximately 43% of brain cells contain only one of the two biosynthetic enzymes, with the remaining 45% of brain cells devoid of both[18,19]. To further complicate the picture, CrT is expressed by microcapillary endothelial cells at the blood brain barrier[15,20,21], but not in astrocytes, suggesting that the blood brain barrier has a limited permeability for peripheral Cr[8,15].

It is thus possible that the brain has to rely on endogenous synthesis to provide most of its Cr demand. It is possible that Cr synthesis in the brain may be dissociated, just like it is in peripheral tissues, with GAA being transported via CrT from AGAT- to GAMT-expressing cells to allow Cr synthesis[22]. This finding expands the knowledge of the usefulness of CrT function in the brain and further underlines its importance in providing brain cells with the correct amount of Cr necessary to perform their function.

### 1.1.5 Creatine Uptake Regulation

Intracellular levels of Cr are finely regulated to prevent its accumulation that would ultimately lead to ATP depletion. Activity of CrT is directly regulated by extracellular Cr levels: CrT activity is higher with low Cr levels and vice versa[23].

AMP activated protein kinase (AMPK) gives another means of regulation. AMPK switches cellular metabolism from energy consuming pathways to energy generating processes. With regard to CrT, AMPK activates protein kinase C (PKC) which is a

known downregulator of CrT[24]. Another possible mean of regulation is offered by AMPK-dependent activation of a cascade involving mTOR (mammalian target of rapamycin), SGK1 and SGK3 (serum- and glucocorticoid-regulated kinase isoforms)[25].

These findings highlight the complex signaling network responsible for Cr regulation, aimed at matching Cr concentration to current cell energy requirements.

## 1.2 CEREBRAL CREATINE DEFICIENCY SYNDROMES (CCDS): A PARTICULAR FOCUS ON CREATINE TRANSPORTER DEFICIENCY

Proton magnetic-resonance spectroscopy (1H-MRS) allows measuring the concentration of Cr, and other metabolites, in the brain. This technique led to the discovery of Cr deficiency conditions as definite disorders of Cr metabolism. Three cerebral Cr deficiency syndromes (CCDS) have been described so far, all of them characterized by severe intellectual disability: GAMT-deficiency, AGAT-deficiency, and Creatine Transporter Deficiency (CTD).

GAMT-deficiency (GAMT chromosomal location 19p13) was the first CCDS to be described in 1994[26], followed by the discovery of the other two conditions AGAT (AGAT chromosomal location 15q15.1) and CTD (CrT chromosomal location Xq28) deficiency (also called CCDS1)[27,28]. The two enzymatic disorders (AGAT and GAMT-deficiency) impair Cr synthesis and are inherited in an autosomal recessive manner while CrT deficiency is inherited in an X-linked manner and affects the creatine uptake[27]. Due to their rarity, it is difficult to establish the real incidence of the three disorders, but a French study investigating 6353 subjects with unexplained neurological symptoms found a prevalence of 0,09% for GAMT-deficiency, <0,02% for AGAT-deficiency, and 0,16% for CTD[29].

Some studies for CTD incidence have a pure focus on males with diagnosis of autism and/or with X-linked intellectual delays and found a prevalence rate ranging between 0,4-1,4% among the examined cohorts[30–35].

This paragraph will describe GAMT and AGAT deficiency syndromes. For CrT deficiency syndrome a more in-depth description will be provided in the next paragraphs, as it is the main focus of this work.

### 1.2.1 GAMT-deficiency

This pathology was first described in a patient who normally developed until 4 months of age, but developmental arrest, hypotonia, hyperkinetic (hemiballistic) extrapyramidal movements and head nodding, emerged later at 22 months of age[26]. GAMT deficiency presents the most severe phenotype with frequently intractable seizures, extrapyramidal movement abnormalities, and sometimes aggressive or self-injurious behavior[27] By mean of *in-vivo* $^{1}$H-MRS of the brain, it was found that the spectrum lacked the creatine signal but was positive for GAA signal[26]. Moreover, GAMT activity was lacking in liver[36]. Following this report, many other cases were diagnosed[37–39,40]. However, it is general consensus to treat GAMT-deficiency patients with a combination of creatine monohydrate supplementation and dietary arginine removal to prevent GAA accumulation and its neurotoxic effects[41], and it has been shown that treatment starting at the pre-symptomatic stage of the disease might widely prevent neurological manifestations[42,43].

### 1.2.2 AGAT-deficiency

Affecting the first enzyme involved in creatine biosynthesis, this disorder was described in patients that at an *in vivo* $^{1}$H-MRS showed low cerebral creatine and low GAA in body fluids (in contrast to GAMT-deficiency patients) suggesting a defect in GAA biosynthesis. This hypothesis was later confirmed by finding the deficient enzyme activity and identification of a homozygous nonsense mutation in the AGAT gene[28].

AGAT-deficiency is rarely associated with seizures, but is frequently associated with progressive muscle weakness and myopathic electromyography, occurring either early (4-14 months of age[44]) or later in life (6-11 years[45])[27].

In these patients, creatine monohydrate supplementation appears to have a better positive outcome[46], with respect to GAMT-deficiency patients, even when started later in life, although the best outcome is still obtained the sooner the treatment it's started[43,47].

### 1.2.3 Creatine Transporter Deficiency (CTD) and its clinical features

CTD was originally described in a patient presenting hypotonia, epileptic events, delayed speech, language development and creatine deficiency in the brain. In this patient GAA levels were normal, but oral creatine supplementation was ineffective in restoring cerebral creatine levels[48]. Subsequently it was demonstrated its X-linked pattern inheritance when a hemizygous mutation in the SLC6A8 gene mapped to the X-chromosome was found, and linked to a deficiency in creatine uptake in fibroblasts[49].

The defect of the creatine transporter (CrT) impairs Cr uptake by the cells and this accounts for an increased urinary creatine to creatinine (Crn) ratio, which is also the main biochemical hallmark of the pathology[50].

Patients affected by CTD are characterized by cognitive deficits with symptoms partially overlapping with autism spectrum disorder, severe speech delay, behavioral abnormalities and seizures[14,27]. Intellectual disability seems to be progressive as suggested by the observation that in some patients behavioral symptoms become more marked during the course of the disease[51,52]. Speech defects are characterized by dysarthria, oral dyspraxia and deficiency in acquiring a semantic-pragmatic language[53]. The motor system is less impaired: a delay in acquisition of independent walking can be observed, as well as subtle extrapyramidal alterations in some cases[52], but a clear muscle weakness has only rarely been described in patients[34]. Accordingly, MRS reveals that the most characteristic feature of CrT deficiency is a severe depletion of Cr in the brain. Cr content in human muscle seems preserved in CrT defects, whereas it is reduced in defects involving the two biosynthetic enzymes[54–56]. The epileptic phenotype is variegated, ranging from patients with no seizure manifestation, to patients with refractory epilepsy; anyhow in most cases

seizures present as febrile-induced and easily controllable[52,57]. Gastrointestinal problems are also frequent in CTD patients, presenting in early life with feeding difficulties and frequent vomiting[27,52,58,59].

### 1.2.4 Diagnosis of Creatine Deficiency Syndromes

When it comes to diagnose CCDS, the main and foremost analysys to undertake is the chromatographic measurement of Cr/Crn ration in urine by means of high performance liquid chromatography, tandem mass spectrometry, or gas chromatography and mass spectrometry, as it makes possible the identification of AGAT-deficiency (low creatine with low GAA excretion) and GAMT- deficiency (low creatine with high GAA excretion), as well as SLC6A8 defects (high creatine/creatinine and GAA/creatinine ratios in urine)[60–64]. GAA can also be measured in plasma to confirm altered results in urine[65].

In addition, AGAT- and GAMT- deficiencies can be further confirmed by enzymatic studies in which enzyme activity is determined in cultured cells by the measure of formed product in the presence of a labeled substrate of the enzyme[28,66,67]. CTD can be confirmed by the creatine-uptake test which consists in measuring creatine uptake by fibroblasts cultured in medium containing creatine. In cells from affected patients no uptake is observed after incubation with 25umol/L creatine; at 500 mmol/L, uptake is 25% of that found in controls. When the uptake inhibitor guanidinoproprionate is added to the medium, the uptake is decreased in cells from healthy subjects, while no change in uptake is observed in cells from patients. This results also indicates that at high creatine concentration, some passive transport or uptake by means of other transporters is possible[66].

Lastly a highly reliable and precise method for diagnosis of CTD is the in-vivo proton magnetic resonance spectroscopy. Positivity to a CCDS is underlined by a spectrum presenting the total absence of creatine and a normal spectral pattern of the remaining metabolites. The employment of this method is though hindered by its expensiveness and the fact that patients with behavior disorders or mental retardation usually need to be sedated[8,68,69].

### 1.2.5 CTD in female heterozygotes

The disorder mainly affects male patients, but heterozygous females can show a mild symptomatic phenotype[70]. In these cases, diagnosis can be difficult as the urinary Cr/Crn ratio is often in normal range and cerebral creatine levels measured by mean of 1H-MRS, although lower than normal controls, show a partial overlap[70]. However, learning difficulties and mild intellectual disability have been reported in several cases [48,49,51,53,58,59,70–75] together with behavioral problems and seizures[57,76,77].

An experiment with cultured fibroblasts highlighted that Cr uptake in females varied between normal and deficient levels, due to severe skewing of X-inactivation arising during culture of fibroblasts, and unrelated to SLC6A8 deficiency[70]. Moreover, in some of the previously cited study, there was found no skewed X-inactivation in peripheral blood leukocytes, hairs, and saliva of heterozygous females[57,70,76,77]. Taken together, these findings demonstrate that there is no selection during development against SLC6A8 mutations, and the phenotype in females is expected to vary from less to more favorable along a continuous gradient depending on the X-inactivation pattern, posing an additional difficulty layer for the identification of mutated SLC6A8 gene carriers.

### 1.2.6 Genetic and Inheritance

Many different types of genetic mutations affecting the *Slc6a8* gene have been described in CTD: missense and nonsense mutations, splice error mutations (intronic or synonymous variants with aberrant splicing), a translation initiation site mutation and multi-exon deletions (LOVD database, http://www.LOVD.nl/SLC6A8)[78,79]. Most of the genetic alterations observed are concentrated in the transmembrane domains 7 and 8 of the protein[80]. About one third of the cases are due to *de novo* mutations[52] In some cases, a missense mutation can result in a residual transporter function, which in turn can in some cases be associated with a milder phenotype[78].

### 1.2.7 Limited success of therapeutic strategies.

While for AGAT- and GAMT-deficient patients, oral supplementation of Cr is sufficient to increase brain Cr levels leading to the improvement of the symptomatology[42,43,47], the attempts to rescue Cr content in the CTD brain by exploiting nutritional

supplementations have been of limited success[14]. Cr supplementation, alone or combined with arginine (Arg), glycine (Gly), and/or S-adenosyl methionine, failed to restore brain Cr content and to resolve clinical signs in the majority of patients with CTD[57,76,81–83]. Indeed, dietary strategies increased cerebral Cr and improved clinical parameters only in milder cases where there was baseline residual brain Cr, and probable residual CrT protein function[82]. In summary, no satisfactory treatment is still available for CTD disorder; therapeutic strategies are palliative for managing seizure and patients need lifelong assistance.

## 1.3 MOUSE MODELS: A MEAN TO UNDERSTAND CTD

### 1.3.1 Mouse models of CTD

Recently, both ubiquitous[54,84,85] and brain-specific CrT-knockout ($Crt^{-/y}$) mouse models have become available, reproducing to various extents the pathological endophenotype of this disorder. These models are fundamental to gain a deeper knowledge of pathology as well as for the pre-clinical study of possible therapies.

Two ubiquitous knockout models have been generated by two different research groups through the deletion of exons 2-4[86] or 5-7[85]. Ubiquitous knock-out models are supposed to offer a higher face-validity as they reproduce both the cognitive deficits and the autistic-like behaviors observed in patients[85]. $Crt^{-/y}$ mice have a reduced Cr concentration in the brain, in both cortex and hippocampus, and in various peripheral tissues, such as muscle, heart and kidney compared to wild-type ($Crt^{+/y}$) littermates[85,86]. A remarkable difference compared to humans is the finding of reduced Cr levels in $Crt^{-/y}$ mice muscle which is not observed in patients. This finding is not an idiosyncrasy of the specific model because it is shared by the other ubiquitous model[87] indicating that this alteration is an intrinsic difference between mouse and human physiology.

One brain specific CrT-knockout model has been obtained by using a CaMKII promoter to drive Cre-recombinase expression in order to achieve a selective CrT deletion in postnatal forebrain excitatory neurons[88] while in another model, the conditional deletion of *Slc6a8* gene in neuronal and glial cells by crossing CrT floxed mice with the

Nestin::Cre recombinase Tg (Nes-cre) 1Kln mouse, leads to ablation of CrT in all CNS cells[89,90]. These models recapitulate quite well the cognitive defects observed in human patients, but show some limitations when it comes to reproducing the autistic-like features observed in many human patients. Moreover phenotypic alterations in brain-specific CrT-knockout models emerge later in life with respect to ubiquitous models, and this marks a substantial discrepancy with the human pathology. Ubiquitous CrT-knockout models are deemed a better model to study CTD and test possible therapies, and for these reasons will be the main tool used in this study. The following sections will report first line findings drawn by the ubiquitous knock-out model obtained by deletion of exon 5-7[85] because it is the same adopted for the present study. These findings were the state of knowledge about the characterization of this model from which the present study started.

### 1.3.2 First line behavioral characterization

A preliminary characterization of the model assessed CrT-/y mice behavior at P40 was carried out to identify behavioral alteration in order to evaluate the face validity of the ubiquitous CrT knockout model. To this mean, various aspects were taken into consideration, from locomotor activity to different kinds of memory.

To test general locomotor activity and anxiety-related behavior, the open field arena was used. Both $Crt^{+/y}$ and $Crt^{-/y}$ mice spent more time in peripheral regions avoiding the center. No difference was found in the amount of time spent in the centre and the periphery of the arena, in motion speed and in total distance covered by animals between the two genotypes. General locomotor activity can also be assessed in a non-aversive environment (compared to the open field arena which has an aversive component) simply measuring home-cage locomotor activity. In this context $Crt^{-/y}$ showed decreased activity during the night period compared to $Crt^{+/y}$. The day-time activity was normal.

Spatial working memory was evaluated by measuring the rate of spontaneous alternation in the Y maze. Both groups explored all the three arms of the maze without any difference in the total number of entries and any bias for one of the arms, further confirming that general exploratory behavior was preserved in KO. In contrast, the alternation rate was

reduced in $Crt^{-/y}$ compared to $Crt^{+/y}$, indicating a specific mnestic alteration in the field of working memories.

Declarative memory was assessed by using the object recognition test (ORT) evaluating the capacity of recognizing a familiar object from a novel one. Both experimental groups explored the objects for the same amount of time during the familiarization phase and showed no difference in object preference during the short term test at 1h, whereas during the test phase at 24h, $Crt^{+/y}$ showed higher preference for the novel object compared to KO. The Morris water maze (MWM) was used to assess spatial learning and memory. Lower swimming speed was detected in KO, and the performance in the training phase was expressed as the distance covered by each animal to find the hidden platform. This distance was longer in $Crt^{-/y}$ compared to $Crt^{+/y}$ in the last three days of training. In order to evaluate the strength of learning and to discriminate between spatial and non-spatial strategies to find the platform, on the last day of MWM the platform was removed and the time spent in the different quadrants of the pool was measured. $Crt^{+/y}$ mice spent more time in the target quadrant, whereas $Crt^{-/y}$ showed no significant preference.

Thus, the $Crt^{-/y}$ model seems to well recapitulate the genetic, neurochemical and clinical features of patients affected by CTD. Consistent with muscle Cr impairment, motor performances were impaired in $Crt^{-/y}$ mice.

### 1.3.3 Pre-clinical therapy attempts

As described above, Cr is a polar molecule that requires a specific transporter in order to enter cells. Thus, while for AGAT- and GAMT-deficiency patients, oral supplementation of Cr is sufficient to ameliorate symptomatology, the same strategy is not effective in CTD patients.

The main strategy applied in recent pre-clinical trials is indeed the employment of molecules capable of crossing the cellular membrane, or finding a means of delivering them inside the cell with no need of a dedicated transporter.

In one of these pre-clinical study, three Cr salts (Cr-ascorbate, Cr-gluconate and Cr-glucose) were employed *in-vitro*, and their ability to increase concentration of Cr and

PCr in hippocampal slices after GPA-mediated pharmacological block of CrT, was tested. The authors report that Cr-gluconate was superior to Cr in increasing tissue content of Cr after transporter block and restore synaptic transmission[120]. However, in their study the transporter was pharmacologically blocked but it retained its functionality, which is a very different scenario than that observed in CTD, where the transporter is totally non-functional. Moreover GPA is a competitive inhibitor of CrT[91], so the effect observed was most likely due to a better kinetic of Cr-gluconate with the transporter with respect to Cr.

Recently the idea that lipophilic derivative of Cr, able to freely cross the cellular membrane and then cleaved to Cr, has arisen, and in a subsequent study of the same group, a similar approach of the previous study was employed to test di-acetyl creatine ethyl ester (DAC), a lipophilic Cr derivative. They report that DAC was able to increase concentration of Cr and restore synaptic plasticity[122]. Again, the block of CrT-mediated Cr transport was obtained pharmacologically, but the "*lipophilic approach*" has proven to be definitely promising.

In an evolution of this approach, a pre-clinical in-vivo study employed another lipholic Cr derivative, dodecyl creatine ester (DCE)[118,121]. In this study DCE was loaded into microemulsion (ME) particles and intranasally delivered. This approach possibly allows a reliable mean of delivery of the substance to the brain, and the authors report beneficial effects in one behavioral test, novel object recognition test (NOR), suggesting that both the combination of DCE and ME could be a promising candidate for the treatment of CTD[92].

Lastly, another promising molecule for CTD treatment is represented by the lipophilic Cr analogues cyclocreatine, cCr. This molecule was already tested in a previous study. In this study, brain specific CrT knock-out mice at PND365 were treated with a high dose of cCr and an improvement in cognitive abilities was reported[88]. This study, however, had some limitations as it only tested the ability of cCr to enter the brain, the behavioral assessment was limited and the treatment had a short duration.

## 1.4 AIM OF THE STUDY

CTD is a severe disorder, with high negative impact on life quality and expectancy of patients as well as their families. Social impact is great as well, due to the lack of any effective treatment and, thus, to the requirement for long health assistance, with economic burden. Effective treatments can only come from a deep understanding of etiology and pathophysiology of this disorder, and in vivo models are precious to achieve this goal.

To date, various CrT knock-out models, as previously described, are available, supporting the preclinical development of therapeutics and a better understanding of CTD pathophysiology[54,85,88–90,92]. However, the efficacy study of novel potential treatments is also hindered by the scarcity of unbiased, quantitative biomarkers for monitoring brain development and function.

EEG and sensory-evoked responses are readily applicable to humans and widely used for non-invasive assessment of cortical function, making electrophysiological measurements or functional imaging ecologically ideal translational tools for functional analyses in children with neurodevelopmental disorders[93–96] . Accordingly, previous studies reported that a standardized inspection of EEG and cortical responses to sensory stimuli is suitable to reveal, both in animal models and patients, stage-specific alterations in other disorders affecting neurodevelopment[97–103]. Aim of this study was to perform an extensive functional analysis in knock-out mice lacking CrT in order to further expand the knowledge around the pathophysiology of CTD. Since creatine is, given its function, important throughout all of an individual life, we asked ourself if the deficits observed in the first line characterization could worsen with age. This piece of knowledge is important to understand whether CTD is a neurodegenerative or a neurodevelopmental disorder, and it is fundamental for the development and planning of therapeutic strategies as well. To investigate this aspect we planned a longitudinal study in which $CrT^{-/y}$ were tested both behaviorally and with IOS at three different time point: at P40, right after the reaching of the brain development maturity, at P110, when the animal reaches maturity, and at P180, when senescence begins. In addition, once reached the ending point of our timeline, part of our experimental subjects were destined to perform an EEG

characterization of $CrT^{-/y}$ mice at P180. To further understand the aspect related to aging in CTD, we employed mice that did not undergo EEG characterization to investigate the presence, at cellular level, of age-related biomarkers in $CrT^{-/y}$ mice at the ending point, P180, of our longitudinal protocol.

Another important aspect to take into consideration is the possible alteration in the neuronal circuitry. Some patients present an epileptic phenotype, and this could hint an excitatory-inhibitory circuits imbalance. We investigated this possibility in the attempt to understand if there is some specific alteration in the neuronal circuitry, possibly affecting some specific neuronal class.

We then used the results obtained to identify reliable biomarkers (behavior, IOS, EEG pattern) that could be used to evaluate therapeutics in the animal model and that could easily be translated to the clinical evaluation of the same therapeutic. The biomarkers so identified were finally used to test a pharmacological approach for CTD treatment.

Importantly, we also took advantage of the availability of data of a few human CTD patients to look for alteration in the EEG pattern. We compared the EEG pattern from human patients with those obtained from $CrT^{-/y}$ mice as identifying a reliable biomarker that could be used both with mice models and in clinical practice would represent a significant breakthrough in the study and in the search of a cure for CTD.

# 2. RESULTS

## 2.1 LONGITUDINAL NEUROCHEMICAL CHARACTERIZATION OF THE MOUSE MODEL

### 2.1.1 CrT deletion led to a widespread Cr reduction in young and adult mice

To understand whether the progression of cognitive deficits in $CrT^{-/y}$ mice was due to a gradual reduction of brain Cr content, we measured Cr levels in various tissues in 1-month- and 6-month-old animals using GC/MS. At both ages, we observed a significant reduction of Cr in the brain, muscle, heart and kidney of $CrT^{-/y}$ mice with respect to wild-type littermates (Table 1). Importantly, no difference was detected in Cr levels measured in the different tissues between P30 and P180 $CrT^{-/y}$ mice, except for the muscle: a Three way ANOVA on rank transformed data analysis revealed a significant interaction between genotype and age only at level of muscular tissue with a significant reduction of Cr levels in P180 $CrT^{-/y}$ mice. A moderate change in GAA levels was observed in some tissues (Table 2) suggesting that Cr deficiency leads to a compensatory attempt by upregulating Cr biosynthesis. Also in this case GAA content measured in P180 animals reproduced the levels reported in younger tissues: a Three way ANOVA on rank transformed data revealed a significant interaction between genotype and age only at level of muscular tissue, but this analysis only stressed a significant reduction of GAA levels in P180 $CrT^{-/y}$ and $Crt^{+/y}$ mice. These results allow rejecting the hypothesis that higher GAA toxicity could underlie the age-related decline of cognitive functions in $CrT^{-/y}$ animals.

### 2.1.2 Reduced body weight growth in $CrT^{-/y}$ mice

A first clue indicating that CrT deficiency elicits age-related detrimental effects emerged from the general appearance of mutant animals. Mice were weighed at different ages and compared with $Crt^{+/y}$ littermates. Even though no particular problems of breeding were observed and the face of $CrT^{-/y}$ mice was normal till P40, $CrT^{-/y}$ animals showed a significantly reduced body weight compared to $CrT^{-/y}$ animals at P60, P100 and P180 (Fig. 4).

## 2.2 BEHAVIORAL CHARACTERISTICS

### 2.2.1 Age-related deterioration of cognitive functions in Cr deficiency conditions

In the behavioral investigation performed at P40, it was highlighted that $CrT^{-/y}$ mice exhibit a general cognitive impairment across different learning and memory tests[85] . To understand whether a progressive deterioration of behavioral impairment is present in $CrT^{-/y}$ mice, we studied four different stages: 1. during the early brain development (postnatal day (P) 28 at the beginning of testing), 2. during the late brain development (P40 at the beginning of testing), 3. in the adult age (P100 at the beginning of testing), and 4. in the middle age (P180 at the beginning of testing). Interestingly, a progressive worsening of cognitive symptoms was detectable in $CrT^{-/y}$ mutant mice, suggesting that age is a key feature of Cr deficiency disease.

### 2.2.2 Y maze

We first analysed the performance of $CrT^{-/y}$ animals at P28 using the Y maze spontaneous alternation, which is an optimal task for probing memory in juveniles (Fig. 1A;[104]). Animals of both groups equally explored all the three arms of the maze. Indeed, no effect of genotype was detected for either the number of entries in the single arms of the maze (designated A, B, C) or the total number of arm entries, indicating that the exploratory disposition of mutant animals was not altered compared to $Crt^{+/y}$ littermates (Fig. 5A).

However, while in young $Crt^{+/y}$ mice alternation rate was about 60% of total arm choices, in $CrT^{-/y}$ animals it dropped to a lower level (Fig. 5B), demonstrating that CrT disruption in the mouse model could reproduce the early pathological phenotype of CTD patients. The same impairment was detected at P40, P100 and P180 with $CrT^{-/y}$ mice performing again at around 50% level whereas $Crt^{+/y}$ age-matched controls showed significant spontaneous alternation (t-test, $P < 0.01$ for P40, $P < 0.05$ for P100 and P180, Fig. 6). These data also indicated that the spontaneous alternation paradigm cannot reveal age-dependent cognitive decline in CrT mutants because of the ceiling effect in the arm alternation deficit masking the effect of the age variable.

### 2.2.3 Object recognition test (ORT)

We assessed declarative memory abilities in the ORT, a test based on the spontaneous tendency of rodents to spend more time exploring a novel object than a familiar one. No difference in short-term recognition memory between P40 $CrT^{-/y}$ mice and age-matched $Crt^{+/y}$ animals could be detected. In contrast, the discrimination index at 24 h was significantly lower in mutant mice, indicating that their capacity to recall the familiar object was impaired (Fig. 7A). This memory deficit became more pronounced two months later (Fig. 7B), eventually affecting both short- and long-term memories at P180. Indeed, at P180 $CrT^{-/y}$ mice showed a marked memory deficit both at 1- and 24-h interval between the sample and the test phase with respect to $CrT^{+/y}$ mice (Fig. 7C), indicating that the longer the time during which neural circuits are forced to work without Cr energy buffer the worse the cognitive performance of $CrT^{-/y}$ animals.

### 2.2.4 Morris water maze (MWM)

We further assessed memory abilities in the MWM, a cognitive paradigm that allows testing spatial learning and memory. The probe test highlighted a spatial memory impairment in Cr deficient mice at all the different ages tested: $Crt^{+/y}$ animals, indeed, spent significantly longer time in the quadrant where the platform was located during the training days, while mutant mice did not remember the location of the hidden platform and equally explored the four quadrants of the maze (Fig. 8). The results obtained in the training phase of the MWM test, however, showed a clear progression of cognitive deficits in $CrT^{-/y}$ mice. Since a main effect of genotype was found on mean swimming speed

recorded all along the training phase at the different ages tested (Fig. 9), we analysed the length of path covered to find the submerged platform. At P40 $CrT^{-/y}$ animals were able to learn the task as well as their age matched $Crt^{+/y}$ controls: although the mean distance to locate the submerged platform on the last three days of training was longer in mutant mice compared to $CrT^{+/y}$ littermates, they exhibited a progressive reduction of the path length similar to $Crt^{+/y}$ littermates with a significant difference between the two groups only at the day 5 of training (Fig. 10A). The same was true in P100 animals (Fig. 10B). In contrast, $CrT^{-/y}$ mice (n = 7) were significantly slower learners with respect to age-matched $Crt^{+/y}$ mice (n = 9) at P180 so much so that the distance to locate the platform was different between the two groups at days 3, 4, 5 and 6 of training (Fig. 10C). To further corroborate the hypothesis of a premature cognitive decline in CrT null mice, we compared the performance in the MWM of P180 $CrT^{-/y}$ animals and one-year old wild-type mice (n= 4). The mean distance to locate the platform on the last three days of training (Fig. 11A) and the probe test revealed a similar learning and memory impairment in these two experimental groups (Fig. 11B).

### 2.2.5 Emotional phenotype is not altered in CrT mutant animals

To rule out the possibility that significant differences in cognitive capacities reflect changes in the ability to cope with stress in challenging task conditions, we analysed the general activity and anxiety-related behavior of $CrT^{-/y}$ and $CrT^{+/y}$ mice in the open field arena at the different ages used for cognitive assessment. We found that the time spent by $CrT^{-/y}$ mutant mice in both the central and peripheral portion of the apparatus was not different from that recorded for $Crt^{+/y}$ animals at any of the time point tested, indicating that the vulnerability to stress and anxiety responses are not sensitive to CrT deletion and excluding the hypothesis that the progression of cognitive deficit might be related to altered emotionality (Fig. 12).

### 2.2.6 $CrT^{-/y}$ mice exhibit increased repetitive and stereotyped behavior

Since the clinical picture of CTD patients includes multiple traits linked to autism spectrum disorders (ASDs), we also examined social behavior in CrT null mice. Although

we used two different social interaction paradigms, we detected no abnormalities in $CrT^{-/y}$ mice at P180. In the social preference test, indeed, both $CrT^{-/y}$ and $CrT^{+/y}$ animals spent significantly more time exploring the wire cup housing the conspecific subject (Fig. 13 A). Similarly, the index measured in the social novelty task did not differ between mutant and $Crt^{+/y}$ mice (Fig. 13 A). The second core ASD symptom domain includes repetitive and stereotyped movements, routines, and rituals[105] and several mouse lines with ASD-associated mutations exhibit enhanced learning on the accelerating rotarod, a task that requires formation and consolidation of a repetitive motor routine[106]. Thus, we tested rotarod abilities of $CrT^{-/y}$ and $CrT^{+/y}$ animals, with the speed of rotation accelerating from 4 to 40 rpm over 600 s. The performance of $CrT^{-/y}$ mutant mice diverged from that of wild-type mice, with a significant increase of fall latency from the drum at all ages tested (Fig. 13B). We next examined self-grooming, another stereotyped behavior in mice[107]. While no difference was present at P40 CrT null mice spent about threefold as much time grooming themselves as littermate $Crt^{+/y}$ mice at P180 (Fig. 13C).

## 2.3 Morphological characterization of neural circuits in $CrT^{-/y}$ mice

The morpho-functional organization of neural circuits in mice carrying CrT mutations has never been studied so far. Thus, we have investigated whether the accelerated decline of learning and memory functions in CrT-deficient mice was accompanied by pathological changes in brain morphology. The cerebral cortex and the hippocampus were analysed because they are strictly involved with the symptoms caused by CrT deficiency in mice and in humans. In the same animals subjected to behavioral characterization, we first evaluated the neuroanatomical architecture of prefrontal (PFC) and cingulate cortex (ACC) of P180 mice. Cortical thickness and neuronal cell density was estimated on NeuN stained sections. No difference in the cortical thickness and neuronal density across cortical layers was observed in mutant animals (Fig. 14).

### 2.3.1 Loss of GABAergic synapses in the cerebral cortex of $CrT^{-/y}$ mice

Since synaptic dysfunction is a feature commonly observed in normal aging and neurodegenerative disorders likely contributing to the pathology progression[108], we

analysed the synaptic punctate expression of vGlut1 and vGAT, respectively as synaptic markers of excitatory and inhibitory neurons, in the cerebral cortex of $CrT^{-/y}$ mice. While excitatory synapses were not affected by Cr deficiency (Fig. 15 A), we detected a prominent loss of vGAT staining both in PFC and ACC, suggesting a specific contribution of GABAergic synaptic alterations to the neuropathological phenotype of CTD (Fig. 15 B). Importantly, the loss of vGAT-positive synapses overspread all the cortical layers. These results are also consistent with previous studies on CTD patients exhibiting evidence for an epileptic phenotype[109] that could be predictive of a dysfunction of inhibitory interneurons.

### 2.3.2 Microglial cell dysregulation in Cr deficient brain

Since aberrant microglia activation is one of the main pathological hallmarks of brain aging[110,111], we have also evaluated Iba-1 expression as a marker of possible morphological changes of microglia in the cerebral cortex (PFC) and the hippocampus (HP) of mutant mice. During aging microglia cells undergo morphological changes towards a reactive phenotype with short, thickened and less ramified processes[112]. We found a strong increase of activated microglial cells in the brain of CrT null animals as compared to wild-type controls, with a parallel reduction of resting cells (Fig. 16 A and B), indicating that the metabolic deficit caused by Cr deficiency leads to a dysfunction of brain-immune cells interactions and to a neuroinflammatory state that can contribute to the cognitive decline reported in $CrT^{-/y}$ mice.

### 2.3.3 Reduced neurogenesis and enhanced lipofuscin accumulation in the hippocampus of $CrT^{-/y}$ mice

It is well-known that the rate of neurogenesis declines dramatically with age and dysregulation of hippocampal neurogenesis is an important mechanism underlying the cognitive impairment associated with normal aging[113]. In order to investigate whether CrT deficiency could affect hippocampal structure and impinge on the neurogenesis process, we examined neuronal proliferation through Ki67 labelling in the dentate gyrus (DG) of wild type and $CrT^{-/y}$ mice. Stereological analysis first revealed that the hippocampal volume of mutant animals was markedly reduced with respect to that

measured in control mice (Fig. 17 A). The number of Ki67-positive cell was significantly lower in the DG of $CrT^{-/y}$ animal at P180, with approximately 30% reduction (Fig. 17 B and D). We also evaluated the number of immature neurons in hippocampal DG using the neuroblast marker doublecortin (DCX). DCX-positive cells were also significantly reduced in CrT null mice DG (Fig. 17 C and E), demonstrating the impairment of adult hippocampal neurogenesis and suggesting another cellular substrate of the cognitive deficit present in the CrT null model. Another characteristic neuropathological finding in CrT mice was the massive accumulation of autofluorescent material (lipofuscin). Lipofuscin is a lipopigment consisting of aggregated products of lysosomal degradation, including oxidized and misfolded proteins, lipids, defective mitochondria and metal ions[114]. We observed a marked accumulation of autofluorescent lipofuscin throughout the brain, but the most prominent autofluorescent signal was seen in the DG hippocampal region. Lipofuscin deposition and accumulation within the hippocampal neurons is a marker of cellular senescence[115,116]. Thus, we compared the area of lipofuscin granules in the brain cells of 6-month-old $CrT^{-/y}$ mice and their $CrT^{+/y}$ siblings. The accumulation of lipofuscin was significantly exacerbated in the hippocampal DG of $CrT^{-/y}$ animals at P180 (Fig. 17 F and G).

## 2.4 LOOKING FOR CTD BIOMARKERS

Quantitative and unbiased biomarkers for monitoring brain function are needed for the efficacy study of novel potential treatment. We characterized our mouse model using EEG and sensory evoked responses and then applied a machine-learning based algorithm to measure the robustness of those data as biomarkers readily applicable in human patients.

### 2.4.1 CrT deficiency causes an alteration of cortical oscillations in mice and humans

We analyzed EEG data obtained from non-anesthetized freely-moving $CrT^{-/y}$ mice and their $Crt^{+/y}$ littermates (Fig. 18A). We found that $CrT^{-/y}$ animals showed a significantly altered power in a wide range of EEG frequencies, including the theta (4-8 Hz), alpha

(8-12 Hz), beta (12-30 Hz) and gamma (30-45 Hz) bands, both during active/passive wake and sleep, regardless of the light or dark phase (Fig. 18B and Fig.19 A-F). Interestingly, a correlation matrix to summarize spectral density data in $Crt^{+/y}$ and $CrT^{-/y}$ mice suggests an anomalous synchronization of brain activity and, possibly, functional connectivity in the brain of $CrT^{-/y}$ animals with a lower number of positive correlations (blue patches) and a higher percentage of inversely correlated frequency bands (red patches) compared to $Crt^{+/y}$ animals (Fig. 20).

To obtain a clinical validation of results obtained in the mouse model, we analyzed EEG data from patients in an attempt to identify cortical network changes and regional alterations associated with CTD. We report a significant difference between CTD patients and age-matched controls for frequency oscillations in the delta, theta, alpha and gamma bands, with CTD subjects having a higher power in delta and gamma frequency and a lower power in theta and alpha frequency. These alterations are particularly prominent in the signal recorded from C3 electrode, but some of them are recurring in different sites of the cortex (Fig. 21 A-L). Noteworthy, the same power bands are altered in the same direction in mice and patients, indicating that EEG alterations in the mouse model might be predictive of those recorded in CTD patients (Fig. 18 C-D)

### 2.4.2 Epileptic phenotype in $CrT^{-/y}$ mice

To test if our model was able to reproduce the epileptic phenotype observed in CTD patients, we used EEG to examine spontaneous epilepsy and kainic acid (KA)-induced seizure susceptibility in $CrT^{-/y}$ mice. We found that approximately 30% of $CrT^{-/y}$ animals showed at least one spontaneous seizure detectable both at behavioral level and as epileptiform activity in EEG during baseline recording (24h), whereas no ictal events were detected in $Crt^{+/y}$ littermates (Fig. 22 A). Notably, mice presenting with the spontaneous epileptic phenotype display on average one electrographical seizure every 2h (Fig. 22 B), with a mean duration of about 20 s (Fig. 22 C), that simultaneously presented as clonic or tonic-clonic convulsions at the behavioural level in most cases (1.4% of tonic seizures, 54.3% of clonic seizures, 44.3% of tonic-clonic seizures). The larger portion of spontaneous seizures occurred during passive wake (7.1% during active wake, 62.9% during passive wake, 30.0% during sleep). The stratification of power spectra revealed a

specific decrease of theta band in $CrT^{-/y}$ animals displaying spontaneous epilepsy (Fig. 22 D-I). Moreover, $CrT^{-/y}$ mice presented a distinct response to kainic acid (KA) challenge compared to $CrT^{+/y}$ mice. Statistical analysis revealed a significant effect of genotype with a higher Racine behavioural score following KA administration (Fig. 23 B), lower latency to epileptiform activity bursts (Fig. 23 C), and higher frequency and mean duration of epileptiform bursts in $CrT^{-/y}$ with respect to $CrT^{+/y}$ mice (Fig. 23 D,E). In addition, the distribution of seizure severity was significantly different between the two groups with $CrT^{-/y}$ mice presenting a high percentage of tonic-clonic seizures (Fig. 23 F).

Taken together, these data reveal that $CrT^{-/y}$ mice exhibit spontaneous seizures and increased susceptibility to pro-convulsant treatment. Moreover, the power of theta EEG band in $CrT^{-/y}$ animals appears to be predictive of spontaneous seizures phenotype.

### 2.4.3 Altered neurovascular coupling in $CrT^{-/y}$ mutants

We examined cortical responses to visual stimulation with different contrast using intact skull IOS imaging in juvenile (PND40) $CrT^{-/y}$ animals. Fig. 24 A shows typical examples of responses from $CrT^{-/y}$ and age-matched $Crt^{+/y}$ littermates. Data analysis revealed that IOS amplitude of the responses driven by contralateral eye stimulation was significantly higher in $CrT^{-/y}$ compared to control mice and the effect was particularly evident at higher contrasts of visual stimuli (Fig. 24 B). We longitudinally tracked visual responses in the same animals as they aged using the 90% contrast visual stimuli. The response to the contralateral eye showed a similar pattern at PND110 and PND180 with a significantly increased amplitude in $CrT^{-/y}$ compared to $Crt^{+/y}$ mice (Fig. 24 C). Moreover, the latency to response peak was higher in $CrT^{-/y}$ at PND110 and PND180 (Fig. 24 D). These results show that hemodynamic response is markedly altered in the cortex of mutant animals, and that this phenotype progresses with age. To clarify whether this is related to a corresponding change of ongoing neuronal activity, we assessed visual responses in a separate group of $CrT^{-/y}$ mice using intracortical visually-evoked potential (VEP) recordings by means of a multielectrode inserted in the binocular visual cortex of PND110 animals. Data quantification revealed a decoupling between IOS and VEP recordings with a comparable VEP amplitude and latency in $CrT^{-/y}$ and $Crt^{+/y}$ animals (Fig. 24 E). These findings suggest that CTD condition affects neurovascular coupling

and that increased perfusion signals detected in CTD animals by IOS imaging may reflect a major dysregulation of vascular regulation. Regardless, hemodynamic measurements emerge as a sensitive biomarker for classifying $CrT^{-/y}$ and $Crt^{+/y}$ mice.

### 2.4.4 A Random Forest classifier quantify robustness of CTD biomarkers

Longitudinal IOS imaging was conducted along with serial neurobehavioral assessments of cognitive and psychomotor functions (Y maze, Rotarod, Morris Water Maze). At the end of the experimental schedule, EEG recordings were performed in the same animals at PND180. Results of behavioral testing confirmed what was previously reported by our group[117], further establishing the robustness and reliability of the endophenotype in our mouse model. To evaluate the reliability of the behavioral phenotype, imaging and electrophysiological recordings as biomarkers of CTD disorder, we computed accuracy using a Random Forest (RF) binary classifier, a supervised machine-learning algorithm for data classification. When trained with the entire dataset, the algorithm showed a remarkable capability to discriminate between $CrT^{-/y}$ and $Crt^{+/y}$ animals (Full; accuracy = 95.67%; Fig. 25 B). As a control, we also repeated the procedure after bootstrapping the dataset (Bootstrap; accuracy = 54.86%). We then assessed the discriminative performance of smaller subsets of data dividing the entire dataset in behavioral (beh), imaging (IOS) and electrophysiological (EEG) variables. We found that behavioral (accuracy = 95.45%), IOS (accuracy = 90.84%) and EEG (accuracy = 88.1%) models showed a significantly better performances than the bootstrap condition. The behavioral subset displayed higher accuracy in segregating $CrT^{-/y}$ and $Crt^{+/y}$ mice than either IOS or EEG, with a performance comparable to the full dataset. Moreover, a principal component analysis (PCA) revealed a significant segregation degree between the two groups in the space of the two first principal components for the Full dataset and the smaller subsets (Fig. 25 A,B). Importantly, the analysis of feature importance highlighted that the most informative variables are Y maze, IOS amplitude and alpha band (night, active wake) in EEG recordings (Fig. 25 C).

# 2.5 CYCLOCREATINE: A PHARMACOLOGICAL APPROACH TO CTD

To investigate whether behavioral measurements and functional biomarkers can be used to study the efficacy of a potential therapeutic agent in $CrT^{-/y}$ mice, we performed a randomized, blind, placebo-controlled, preclinical trial to explore the therapeutic efficacy of a chronic (24 week) daily treatment with cyclocreatine (cCr) (Fig. 27 A). It has been reported that lipophilic analogs and other derivatives of Cr can enter cells independently of CrT and could represent a promising approach for CTD treatment[88,92,118–122]. In particular, cCr is a nearly planar Cr analog that can be phospho/dephosphorylated by Cr kinase, thus mimicking the metabolic function of Cr[88,123–125]. However, the evaluation of these treatment options has been limited to biochemical measurements, behavioral outcomes and in vitro assays of neuronal function.

Here, we combined functional biomarker assessment with well-established behavioral readouts for CTD to monitor brain function of $CrT^{-/y}$ mice at three time points (P40, P110, P180) in response to pharmacological intervention.

## 2.5.1 Effects of CCr on hemodynamic responses of CTD brain

Since we found that hemodynamic responses are altered in $CrT^{-/y}$ mice and that hemodynamic measurements obtained with optical imaging are a reliable biomarker of brain function in $CrT^{-/y}$ animals, we longitudinally tracked visual responses in the same animals used for behavioral assessment at the three different time points. While no difference was detected between non-treated animals and vehicle-treated mice for every age examined, we found a dose-dependent effect in mice administered CCr. More specifically, responses of mice treated with 140 mg/Kg CCr were significantly lower with respect to untreated animals at every time point tested, moving the amplitude of signals closer to that measured for $Crt^{+/y}$ animals; the medium dose ameliorates IOS signal at P110 and P180 and the low dose was effective only at P180 (Fig. 27 B-C).

### 2.5.2 CCr does not rescue reduced body weight growth of CrT$^{-/y}$ mice

CrT$^{-/y}$ mice have a significantly reduced body weight with respect to Crt$^{+/y}$ littermates[85,117]. We weighed the mice every other day starting from P20, concurrent with the start of CCr treatment. No treatment was effective in ameliorating the decreased body weight in CrT$^{-/y}$ mice; CCr treatment did not result in any decreases in body weight either (Fig. 26).

### 2.5.3 CCr partially prevents age-related cognitive decline in CrT$^{-/y}$ mice

Since we previously reported that the Y-maze is a behavioral test with very high performance in discriminating between CrT$^{-/y}$ and Crt$^{+/y}$ animals (Mazziotti, Cacciante et al., BrainComm in press),we first assessed spatial working memory to evaluate for cCr effects on cognitive function. Untreated CrT$^{-/y}$ mice performed worse than CrT$^{+/y}$ littermates, confirming our previously published data regarding the mouse model characterization[117]. We found a small but statistically significant increase in the spontaneous alternation rate for CrT$^{-/y}$ mice treated with the high and the medium dose levels of CCr at P40; no beneficial effects were observed at P110, while all three CCr dose levels improved the cognitive performance of CrT$^{-/y}$ animals at P180 (Fig. 27 D). Importantly, CrT$^{-/y}$ animals treated with vehicle had an alternation rate comparable to untreated animals at every time point. There were no differences in the total number of entries in the 3 arms of the maze between the different groups.

We also investigated spatial learning memory using the Morris Water Maze (MWM) at P110 and P180. We already found that CrT$^{-/y}$ mice are significantly slower swimmers with respect to CrT$^{+/y}$ littermates[117] and cCr had only a partial effect in ameliorating this phenotype. No dose levels showed a beneficial effect in either the training phase or in the probe trial at P110 (Fig. 28 A-C), whereas treatment with 46mg/kg of CCr was able to reduce the distance needed to locate the platform during the training phase at P180 with no change in velocity (Fig. 27 E-F). A partial effect was also detected in the probe trial for the high and medium dose level at P180: despite the lack of a specific preference for the target quadrant, CrT$^{-/y}$ mice treated with 140mg/kg and 46mg/kg CCr mostly explored

the target quadrant and adjacent ones, suggesting the presence of a memory trace (Fig. 27 G). No differences were observed between non-treated animals and vehicle-treated animals at any time point (Fig. 27 D-G). Differences in MWM performance between untreated $CrT^{-/y}$ and $CrT^{+/y}$ confirms our previous findings[117].

Altogether, these results suggest that CCr has a partial effect in recovering learning and memory functions, potentially acting to prevent its age-related decline.

### 2.5.4 Stereotypical behavior is reverted with CCr treatment

Another important hallmark characterizing $CrT^{-/y}$ mice and CTD patients is the presence of stereotypical and autistic-like behaviors[52,117]. Accordingly, we reported that $CrT^{-/y}$ mice perform better than their $Crt^{+/y}$ littermates in the rotarod test, with a longer fall latency from the rotating drum, and spend considerably more time grooming[117]. Here, we found that all three cCr dose levels were effective in reducing stereotyped movements in the rotarod at P40, whereas at P110 and P180 only the high and medium doses displayed the same beneficial effect (Fig. 27 H). CCr treatment reverted fall latency effects to those observed in $Crt^{+/y}$ animals in most of the cases.

Reversion to $Crt^{+/y}$ phenotype was also observed in self-grooming assessments; $CrT^{-/y}$ animals treated with every CCr dose tested showed a drastic reduction in the time spent grooming at P180 (Fig. 27 I). This evidence strongly suggests that CCr might ameliorate stereotypic and autistic-like behaviors in CTD.

### 2.5.5 CCr ameliorates the epileptic phenotype and increases resistance to chemically- induced seizure events

Since we have shown that CrT deficiency causes an alteration of cortical oscillations and the manifestation of a full-blown epileptic phenotype in the mouse model at P180 (Mazziotti, Cacciante et al., BrainComm in press), we used EEG recordings of spontaneous activity and following KA administration to characterize the outcome of chronic CCr treatment on this relevant pathological feature. We previously reported behavioral and IOS variables exhibit a very high power in discriminating between $CrT^{+/y}$ and $CrT^{-/y}$ mice (Mazziotti, Cacciante et al., BrainComm in press).

The analysis of spontaneous EEG showed no influence of vehicle treatment in any frequency band or behavioral state measured (multiple t-tests, two-stage step-up method of Benjamini, Krieger and Yekutieli for False Discovery Rate). cCr-treated mice showed differences compared to V-CrT$^{-/y}$ only for theta band during passive wake (all doses; One-way ANOVA post-hoc Dunnett's multiple comparisons test, $p < 0.05$) and sleep (H-CrT$^{-/y}$ animals, $p < 0.05$) in the night phase, with non-significant trends ($p < 0.1$) for theta band during passive wake (M-CrT$^{-/y}$ mice, $p = 0.061$) in the day phase, and alpha band during sleep both in the day and night phase (H-CrT$^{-/y}$ animals, $p = 0.078$ and $p = 0.098$). However, a much clearer response to cCr emerged by pooling together untreated and V-CrT$^{-/y}$ mice.

Indeed, we found that cCr increases cortical theta band activity in the passive states of vigilance (H and M doses) and sleep (only H, during night), with H-CrT$^{-/y}$ also showing an increase of low alpha band in sleep phase both during day and night (Fig. 29 A-F).

The percentage of animals experiencing spontaneous seizures at the clinical and electrographical level was significantly lower in H-CrT$^{-/y}$ and M-CrT$^{-/y}$ groups (Fig. 30A) and a significant increase of theta band power was detected in the brain of CrT$^{-/y}$ mice treated with cCr compared to CrT$^{-/y}$ animals showing spontaneous seizures (Fig. 30 B-G). Based on these results, we assessed the response to KA challenge in H-CrT$^{-/y}$ and M-CrT$^{-/y}$. Electrographical analysis and behavioral scoring revealed that H-CrT$^{-/y}$ animals display a more prolonged latency and a shorter duration of epileptiform bursts (Fig. 30 H,J), although cCr treatment did not affect the frequency of evoked seizures (Fig. 30 I). The distribution of seizure severity was also statistically different among the different groups, with H-CrT$^{-/y}$ and M-CrT$^{-/y}$ mice presenting a lower amount of tonic-clonic seizures (Fig. 30 K).

Taken together, these results suggest that cCr can protect against spontaneous seizures and shift epileptic susceptibility towards a milder phenotype.

# 2.6 CELL SPECIFIC IMPAIRMENT OF PARVALBUMINERGIC INTERNEURONS

We asked ourselves if the deficit found in GABAergic puncta could involve a specific class of interneurons. Parvalbuminergic (PV) neurons seemed like a good candidate as with their characteristic burst-firing activity they are high energy-demanding cells[126–130]. Our hypothesis is further corroborated by the fact that CrT expression is strongly correlated and high in fast-firing cell types[9]. Moreover parvalbumin interneurons are the primary source of direct inhibition to the soma or initial segment of the pyramidal neuron axon[131]. Reduction in cortical PV neurons number has been observed in post-mortem analysis of autistic patients[132] and an alterations in PV neurons network have been found in animal models of autism, schizophrenia and attention-deficit hyperactivity disorder[133–136]. Lastly, parvalbuminergic network alterations have been linked with the onset of seizures in various epilepsy models[137,138,139].

We analysed both parvalbumin-positive cell number and parvalbumin-positive puncta density in the cortex of $CrT^{-/y}$ mice by mean of immunohistochemistry, and we found no differences in the cortical cell density in the PFC (Fig. 31 A), a decreased cell density in ACC (Fig. 31 A), and a marked decrease in parvalbumin puncta both in PFC and in ACC (Fig. 31 B). This finding further strengthens our hypothesis and can offer a direct link between the alteration in the inhibitory circuitry and the epileptic phenotype observed in human patients.

The following sections will describe our first and preliminary results obtained employing a conditional PC-CrT knockout model.

## 2.6.1 A conditional PV-CrT knockout mice model recapitulates phenotype displayed by $CrT^{-/y}$ mice.

We developed a PV specific knockout model in which a conditional CrT allele was deleted in postmitotic PV-neurons, by using the PV promoter to drive Cre-recombinase expression (PV-$CrT^{-/y}$ mice) only in parvalbumin interneurons[140].

We tested this model employing a combination of y-maze, IOS and EEG as these three experiments represent, according to the random forest classifier previously described, the most effective, reliable and exhaustive way to evaluate the phenotype linked to CTD.

We behaviorally tested PV-CrT$^{-/y}$ mice with the Y-Maze test, since it is the behavioral test that better discriminate between genotypes, and we found that PV-CrT$^{-/y}$ mice show a spontaneous alternation rate lower than PV-CrT$^{+/y}$ (Fig. 32 B), confirming that cognitive deficits may arise due to alterations in the parvalbuminergic neurons.

IOS has been revealed in our study to be an effective and reliable biomarker capable of discriminating between CrT$^{+/y}$ and CrT$^{-/y}$ genotypes. Here, we recorded visual evoked IOS in PV-CrT$^{+/y}$ and PV-CrT$^{-/y}$ mice and we found an increase in the signal amplitude in PV-CrT$^{-/y}$ with respect to PV-CrT$^{+/y}$ mice (Fig. 32 C), same as we previously observed in CrT$^{-/y}$ mice, confirming the validity of the model. To note that the delta of response amplitude may not be as pronounced as for the naive model, but since parvalbuminergic neurons represent just a small fraction of cortical cells, the result is remarkable.

### 2.6.2 Preliminary results on the epileptic phenotype in PV-CrT$^{-/y}$ mice

We applied the same KA-challenge protocol to PV-CrT$^{-/y}$ mice in order to assess the contribution of parvalbuminergic interneurons in the development of seizures events.

This experiment is at a preliminary stage, nonetheless we already were able to observe that after the first KA-injection PV-CrT$^{-/y}$ mice display a racine scale score higher than PV-CrT$^{+/y}$ mice (Fig. 33A); PV-CrT$^{-/y}$ mice also display a decrease in the latency to first seizures following first KA-injection, a higher frequency and duration of seizures, with respect to PV-CrT$^{+/y}$ mice (Fig. B-D); seizure events are also more severe as the percentage of tonic seizures is decreased, whereas the percentage of tonic-clonic seizures is increased (Fig. E).

Altough the preliminary nature of these findings, the differences between PV-CrT$^{+/y}$ and PV-CrT$^{-/y}$ already seems to suggest a major role of parvalbuminergic neurons in the development of the epileptic phenotype.

# 3. DISCUSSION

## 3.1 Characterization and face validity of the mouse model

CTD is known to cause brain Cr depletion and several neurological deficits, but nothing is known about the neurobiological basis of this disease. We performed the first analysis of morphological, cellular and behavioral impairments in a CTD mouse model. The results report the earliest cognitive phenotype observed so far in CTD mice, and a novel behavioral phenotype consisting of enhanced stereotypies. Moreover, we found that phenotypes associated with brain aging, including a progressive learning and memory deterioration, synaptic loss, microglial cell activation, neurogenesis impairment and lipofuscin deposition already occur in adult animals. The significant differences in learning and memory performance of $CrT^{-/y}$ mice reflected changes in cognitive abilities *per se*: indeed, the open field test revealed that mutant mice display anxiety levels in the range of normal values, indicating that their capacity to cope with stressful conditions of behavioral tests is not altered.

Since epilepsy is common in CTD[27,109] and seizures are one of the symptoms with the greatest impact on quality of life of patients and caregivers, these findings fill a

considerable gap in the current literature and substantially expand the translational validity of our CTD murine model for the evaluation of therapeutic strategies.

An important question raised by the premature aging of $CrT^{-/y}$ mice concerns the role of Cr deficiency in the aging process. It is worth noting that the cognitive regression of $CrT^{-/y}$ animals was not paralleled by either a decrease of Cr levels in the brain tissue or a rise of GAA toxicity, suggesting that the prolonged lack of Cr energy buffer may set in motion cellular compensatory mechanisms, such as a continuous synthesis of ATP and corresponding generation of ROS, leading to the gradual deterioration of brain function. We detected a significant reduction of Cr levels in P180 $CrT^{-/y}$ mice with respect to P30 CrT null mice only at level of muscular tissue, indicating that compensatory upregulation of Cr in the muscle declines with age. Despite the ubiquitary pattern of CrT deletion, only few CTD patients displayed an alteration of muscular Cr levels and strength[34]. Our results raise the possibility that a muscular phenotype could occur also in patients later in life.

We have considered the possibility that the accelerated decline in cognitive performance in mature $CrT^{-/y}$ animals could be related to the documented neuroprotective[34,141–143] and anti-apoptotic effects of Cr[144]. However, when we examined the neuronal density in the cerebral cortex, we did not detect any significant reduction in the number of NeuN-positive cells either in the PFC or in the ACC. In contrast, we found a marked impairment of hippocampal neurogenesis in the brain of mature $CrT^{-/y}$ mice. This was assessed by observing significantly reduced numbers of Ki67-positive proliferating cells along with DCX-positive immature neurons in the hippocampal DG region. These results are consistent with the notion that the creation of new neurons is an energetically expensive process[145] and that the hippocampus is particularly vulnerable to metabolic alterations[146]. Since adult hippocampal neurogenesis plays a vital role in maintaining normal cognitive processing[146,147], an impairment of this process could conceivably compromise hippocampal function and represent a key substrate of the cognitive defects seen in $CrT^{-/y}$ mice. Accordingly, most studies indicate a correlation between a compromised neurogenic niche and impaired performance in hippocampus-dependent cognitive tasks in aged mice[113].

In addition, we observed that long-term Cr deficiency induce a more subtle and specific reorganization of neuronal circuits consisting in significantly lower expression of the vesicular GABA transporter. This alteration, which has been detected in two brain regions fundamentally involved in the processing of learning and memory tasks such as the PFC and the ACC, could be mirrored by a significant dysfunction of synaptic activity leading to increased cognitive frailty. It has been reported, indeed, that alterations in inhibitory interneurons contribute to cognitive deficits associated with aging and neurological diseases[148,149].

One of the principal findings of this work is the demonstration that neuroinflammation plays a critical role in the progression of CrT disorder. It is apparent that Cr deficiency causes an aberrant activation of microglial cells in the brain of mature $CrT^{-/y}$ animals and activated microglia may release a number of cytokines and chemokines, which in turn activate many proinflammatory signal transduction pathways. It is known that co-activation of proinflammatory and cytotoxic products during neuroinflammation process is detrimental to neurons and may alter synaptic proteins[150]. . Recent evidence demonstrates that neuroinflammation also negatively affects hippocampal neurogenesis[151,152]. We could hypothesize that activated microglia-neuron crosstalk has detrimental effects on hippocampal neurogenesis and brain synaptic connectivity in $CrT^{-/y}$ animals. Thus, the dysregulation of microglial behavior appears to be a critical component of the negative progression of CrT deficiency pathology.

A possible trigger of neuroinflammation is the increased concentration of damaged macromolecules and protein aggregates as a result of an increase in oxidative stress as well as of mitochondrial dysfunction leading to excessive generation of reactive oxygen species (ROS) and oxidative damage to lipids, proteins and DNA. The Cr/PCr system is strongly implicated in the cellular bioenergetic function and several studies have revealed a correlation between Cr levels and intracellular ROS in as much Cr exhibits antioxidant activity through either direct interaction with oxidant species or metabolic action conferring antioxidant protection[153,154]. Accordingly, we found an enhanced accumulation of lipofuscin in the brain of $CrT^{-/y}$ mice that could be the result of increased oxidative damage[155]. The presence of lipofuscin can also influence important cellular processes, such as autophagy, by inhibiting the fusion between autophagosomes

and lysosomes, thus further exacerbating the accumulation of degradation products and cognitive impairment[156].

Present results suggests that CrT null mice may undergo an early onset of brain aging. One fundamental conclusion emerging from this work is that CTD is a metabolic disorder associated with early brain aging and that age should be a key factor to deal with in the clinical evaluation of patients. It has been previously reported that patient intellectual disability becomes more pronounced with age[27], but longitudinal studies in patients are totally lacking and little is known about the progression of the disease.

In addition, our CrT mouse model allowed us to discover alterations of cellular and molecular mechanisms that play a pivotal role in the generation of the CTD neurological phenotype. Mutant mice displayed alteration of GABAergic system, reduction of hippocampal neurogenesis, marked activation of microglia, and altered oxidative metabolism, leading to a general cognitive deterioration progressively worsening with age.

We further investigated the alteration of the GABAergic system assuming that the observed alteration could be specific of a specific interneuron class. To test this hypothesis we choose to investigate the parvalbuminergic neurons, because these interneurons have a very high metabolic rate so it was an educated guess to assume they would be the ones to suffer the most from the lack of creatine. Indeed we found that cortical parvalbuminergic puncta density was decreased in $CrT^{-/y}$ mice, thus confirming our hypothesis.

To better understand the parvalbuminergic network involvement into the development of the deficits observed in CTD we developed a conditional knock-out model in which the creatine transporter was ablated only into parvalbuminergic interneurons. Experiments in this model showed the same behavioral deficit observed in the total knock-out model and IOS responses confirmed the same neurovascular coupling alterations found in the total knock-out model. Moreover, our preliminary data indicates a higher susceptibility to epileptic seizures, suggesting that parvalbuminergic neurons may in fact be largely responsible for the phenotype observed in the total knock-out model.

This knowledge opens the important possibility to design targeted-drug intervention protocols aimed at overcoming brain alterations. If we could rescue brain alterations

underlying CTD, indeed, both clinical and behavioral amelioration should be achieved. The use of non-invasive methods for behavioral assessment suitable for longitudinal analysis and the morphological characterization of brain alterations in $CrT^{-/y}$ mice set a firm background for translational studies using this model, providing normative data and protocols necessary to validate potential treatment strategies prior to launching costly clinical trials.

Our data also suggest that $CrT^{-/y}$ animals may serve as a useful model for exploring the mechanisms of age-related damage in the brain. A large number of neurodevelopmental and neurological disorders, including Down syndrome, Batten disease, progranulin deficiency, brain iron dysregulation, have been associated with early brain aging[157–160]. Thus, a better understanding of factors that accelerate age-related deterioration of cognitive performance is critical both for improving the likelihood for successful aging and for revealing pathological changes of translational value.

## 3.2 The importance of reliable biomarkers in the development of therapeutic strategies for CTD

Quantitative biomarkers measuring cortical function are a fundamental tool for the development of therapeutics, and different techniques have been recently and successfully introduced in clinical and research settings for neurodevelopmental disorders[99,102,161,162]. Following this approach, we report novel functional CTD biomarkers capable of classifying mutants at single animal level with high accuracy and sensitivity (>85%), and to measure disease progression and amelioration. These data provide an accurate protocol for CTD assessment with tools of high translational value constituting a paradigm for future preclinical trials on this condition, and more broadly for neurodevelopmental disorders presenting with cognitive dysfunction, autistic-like features and brain hyperexcitability.

The clinical relevance of spectral changes of EEG signal apparent in $CrT^{-/y}$ mice was proved by our findings showing a comparable dysfunction of neural oscillations in CTD patients. More specifically, theta (4-8Hz) and alpha (8-12Hz) power was decreased in the cerebral cortex of $CrT^{-/y}$ mice compared to $Crt^{+/y}$ animals, whereas beta (12-30Hz) and

gamma (>30Hz) power was increased, highlighting a transition from physiological to pathological network activity similar to that observed in other neurodevelopmental disorders and patients in the autistic spectrum[163–165]. Importantly, the same power bands were altered in the same direction in mice and patients, identifying a "network biomarker" of CTD disorder. Moreover, we demonstrated that $CrT^{-/y}$ mice display an epileptic phenotype, with spontaneous seizure occurrence and increased susceptibility to kainic acid, as assessed through behavioral observation and video-EEG recordings in awake animals. The stratification of animals based on the manifestation of spontaneous seizures revealed that epileptic mice exhibit a specific decrease of theta power band with respect to non-epileptic animals. This result is in agreement with previous literature showing that changes in theta band power can be predictive of epilepsy[166–168].

Since the timing of rhythmic activity in cortical networks strongly affects the coordination of neuronal responses throughout the cortex, the EEG alterations found in CTD mice and patients establish a robust link between alterations in brain oscillatory activity and the pervasive cognitive and behavioral impairment of this condition, suggesting that a derangement in local and long-range cortical connectivity and plasticity could be a good candidate to explain at the network level the pathological endophenotype of CTD[169–181]. The increase of beta and gamma power could seem at odds with the observed cognitive deficits and natural history of CTD, but excessive beta/gamma activity was previously associated with increased brain excitability and seizures[182–185]

We also found a highly specific increase of cortical IOS responses in $CrT^{-/y}$ mice. Since IOS imaging measures BOLD-like signals, these data suggest that the assessment of brain metabolic consumption might represent a further non-invasive and sensitive biomarker for the analysis of brain function in CTD. In light of the ubiquitous expression of Slc6a8 gene in the brain at the cellular and regional level[186], the normal VEP amplitude recorded in the visual cortex of $CrT^{-/y}$ mice suggests that glial and vascular cells might be the cellular basis of altered IOS. Accordingly, the forced metabolic phenotype and the resultant increase of cellular oxidative stress observed in the brain of $CrT^{-/y}$ animals[117,187] could dynamically upregulate the cerebral blood flow stimulating vasodilation [188]. Abnormal neurovascular coupling could significantly affect fMRI responses in CTD patients and represent another CTD biomarker of relatively easy assessment in children using

functional near infrared spectroscopy (fNIRS), an imaging method of cerebrovascular dynamics particularly suitable to patients with neurodevelopmental disorders[94,95].

Using a Random Forest machine-learning algorithm for data classification, we showed that behavioral, imaging and EEG assessment can be used to automatically classify single subjects, providing a very reliable protocol to longitudinally monitor the efficacy of potential therapeutic strategies in preclinical studies for CTD. Since ease of testing is a key factor in complex multidose assessments, we also showed that smaller subsets of variables could reach a similar discriminative performance. In this framework, Y maze and IOS amplitude emerged as the two more informative variables, indicating that even simpler sets of physiological parameters could be a powerful tool for tracking disease progression and the efficacy of treatments.

Overall, our findings identify novel, translational and non-invasive biomarkers for the analysis investigation of brain function in CTD. Despite the availability of reliable tools for CTD diagnosis, including biochemical, magnetic resonance spectroscopy and genetic analyses, the biomarkers discovered in this work will have a fundamental impact in the research and clinical setting at multiple levels: (i) their evaluation will allow clinicians to optimize the follow-up of patients, recognizing possible alterations of brain circuits during the progression of CTD disorder; (ii) the study of EEG pattern could be predictive of the epileptic phenotype; (iii) the combination of behavioral, IOS and EEG testing provides, providing a very reliable protocol to longitudinally monitor the efficacy of potential therapeutic strategies in preclinical, and possibly clinical, studies.

## 3.3 Cyclocreatine treatment: a pharmacological approach and an excellent benchmark for biomarkers testing.

By using our battery of functional and behavioral assessment, we found that chronic cCr treatment was effective on different aspects of CTD, including cognitive dysfunction, autistic-like features and epilepsy.

We found that cCr was able to rescue loss of working memory and prevent age-related long-term memory loss, even though to a lesser extent. Moreover, a reduced performance in rotarod and shorter time spent grooming themselves demonstrate that cCr treatment is very effective in ameliorating the autistic-like phenotype in $CrT^{-/y}$ mice, strongly downsizing the manifestation of stereotypical movements, motor routine and rituals. Importantly, cCr has a positive effect in counteracting the epileptic phenotype of $CrT^{-/y}$ mice, with a lower percentage of animals experiencing spontaneous seizures and a higher resistance to chemically-induced convulsions. This is mirrored by increased theta power in basal EEG activity, strengthening the hypothesis that alterations in theta band frequency can be predictive of epilepsy[166–168].

The outcome of this pharmacological approach has been previously evaluated in brain-specific CrT conditional knockout mice, reporting a beneficial outcome for learning and memory deficits[88]. This study, however, was mainly oriented in testing the effective ability of cCr to enter brain cells and to serve as substrate for Cr kinase, and the face and construct validity of the brain-specific model are limited, as a milder pathological endophenotype seems to emerge quite late in this breed of mice (see also [89]). Kurosawa and colleagues probed only cognitive aspects of CTD clinical picture in aged animals (PND365) and in response to a short treatment with highly concentrated cCr. Some discrepancies between our studies further confirm this interpretation: Kurosawa used a harder protocol for MWM and the fact he didn't observe a difference in the baseline time spent in platform area between $CrT^{+/y}$ and $CrT^{-/y}$ corroborates the idea that the brain-specific knockout manifests a milder phenotype; in addition he reports that impaired and cognitive performance are normalized after 9-weeks of treatment whereas we only found a partial rescue, despite our 24-weeks of treatment, again possibly because of the milder phenotype of brain-specific knockout model.

Here, we employed an ubiquitous $CrT^{-/y}$ knockout model, exhibiting a precocious impairment of cognitive functions and sharing all the main hallmarks of human pathology, and a comprehensive experimental design to longitudinally assess the therapeutic validity of chronic cCr treatment and to determine the minimum effective dose (MED) on different aspects of CTD pathological framework. We designed the study to fulfil the best-practice guidelines for rigorous assessment in preclinical trials, including

the use of a mouse model of well-established face and construct validity (the ubiquitous $CrT^{-/y}$ knockout model;[117]), robust statistical design with a priori computation of the sample size based on primary endpoints, minimization of genetic variability with littermates, random allocation of subjects to experimental groups, blinded assessment of readouts, longitudinal quantification of multiple robust and reproducible outcome measures, and dose-response analyses with placebo controls to determine the minimum effective dose (MED) on different aspects of CTD pathological framework. To stick as closely as possible to expected clinical trial indications, the treatment started in already symptomatic mice and involved chronic intervention. Our results clearly indicate that the high (140 mg/kg) and the medium (46 mg/kg) doses have the stronger therapeutic effect in $CrT^{-/y}$ mice and MED is potentially 46 mg/kg for cognitive defects and network hyperexcitability, whereas 14 mg/kg emerge to be sufficient to drastically reduce autistic-like stereotyped movements. This variability might reflect distinct metabolic constraints of different brain processes, with the circuitry involved in the government of stereotyped movements possibly demanding less energy than those related to working and declarative memory[189].

Importantly, we did not report any detrimental product of cCr treatment. The only possible side effect could be the decrease of delta frequency power and the gain of alpha power during the sleep phase observed following the treatment with the 140 mg/kg cCr dose, potentially causing sleep disturbances. Together with the lack of preservation against chemically-induced convulsions in H-$CrT^{-/y}$ mice, these data raise the possibility that an excess of cCr could have adverse effects on brain circuitry and future toxicology studies in wild-type and knock-out animals are needed to assess the safety window of this prodrug. However, our findings strongly support the efficacy of cCr for treating CTD, opening the possibility to design intervention protocols for this drug or other chemically modified, lipophilic compounds that could be readily translated to the bedside.

# 4. MATERIALS AND METHODS

## 4.1 Animals

As CrT deficiency is an X-linked pathology, male mice were selected for this study. $CrT^{-/y}$ and $CrT^{+/y}$ mice on a C57BL/6 J background were generated as described previously[85]. Animals were maintained at 22°C under a 12-h light–dark cycle (average illumination levels of 1.2 cd/m2 ). Food (4RF25 GLP Certificate, Mucedola) and water were available ad libitum. To target CrT deletion to parvalbuminergic cells of the central nervous system we used a mouse[190] expressing Cre recombinase under the PV promoter (PV:Cre). $CrT^{+/fl}$ females were crossed with Nestin:Cre male mice to generate a mouse line carrying the floxed CrT and Nestin:Cre alleles. Mice with three genotypes were used as experimental animals: mice carrying the brain specific deletion of CrT (PV:Cre-$CrT^{-/y}$, PV-$CrT^{-/y}$), mice expressing the floxed allele but not Cre-recombinase ($CrT^{fl/y}$), and mice expressing Cre-recombinase but not carrying the floxed allele (PV:Cre-$CrT^{+/y}$, PV-$CrT^{+/y}$). These genotypes were obtained in the same litters. Since $CrT^{fl/y}$ mice did not display any difference in Cr levels with respect to PV-$CrT^{+/y}$ animals, we performed behavioral and anatomical investigation only in the other two experimental groups. All experiments were carried out in accordance with the European Communities Council Directive of 24 November 1986 (86/609/EEC) and were approved by the Italian Ministry of Health (authorization number 259/ 2016-PR).

## 4.2 Detection of Slc6a8 mutation by PCR

Genomic DNA was isolated from mouse tail using a kit, and the protocol suggested by the manufacturer (DNeasy Blood & Tissue Kit, Qiagen, USA). DNA was amplified for CrT mutant and wild-type alleles using a standard PCR protocol with the following primers: F:AGGTTTCCTCAGGTTATAGAGA; R:CCCTAGGT

GTATCTAACATCT; R1: TCGTGGTATCGTTATGCGCC. Primers for Cre recombinase expression were: F: AACGCACTGATTTCGACC; R: CAACACCATTTTTTCTGACCC. For PCR amplification, we used 300 ng of DNA in a 25 ll reaction volume containing 0.2 mM of each dNTP, 2 lM of F primer, 1 lM of R primer, 1 lM of R1 primer and 0.5 U/ll Red Taq DNA polymerase (Sigma-Aldrich, Italy). The PCR conditions were as follows: 94 C for 4 min followed by 37 cycles at 94 C for 30 s, 58 C for 30 s, 72 C for 40 s and a final extension at 72 C for 7 min. Amplicons were separated using 2% agarose gel and visualized under UV light after staining with Green Gel Plus (Fisher Molecular Biology, Rome, Italy). Amplicon sizes were: $Crt^{+/y}$ allele = 462 bp; mutant allele = 371 bp; Cre allele = 310 bp.

## 4.3 Experimental design of longitudinal mouse experiments

The same animals were subjected to longitudinal IOS recordings at PND40, PND110 and PND180. At least 4 days after the completion of each IOS recording, the animals were each subjected to serial neurobehavioral assessments of cognitive and psychomotor functions (Y maze, Rotarod, Morris Water Maze (PND110 and PND180 only)). Behavioral assessments were performed as previously described[117]. At the end of the experimental schedule, EEG electrode surgeries followed by EEG recordings were performed. A separate group of animals were used for VEP experiments.

This preclinical trial was a randomized, double-blind study of three fixed doses of CCr. $CrT^{-/y}$ mice were divided in 5 groups, each one receiving either no treatment (NT), vehicle treatment (VEH), or three different CCr dosages (H, high = 140 mg/kg; M, medium = 46 mg/kg; L, low = 14 mg/kg). The treatment started at P20. CCr was dissolved in 1% low fat chocolate milk (in a volume of 2.5 ml/kg) and daily administered *per os*. Animals were weighed every other day to adjust the drug solution volume. Animals were randomly assigned to the different arms of the study. All treatments, experiments and analysis were performed in blind with the respect to the genotype of animals and the treatment administered. The same animals were subjected to longitudinal IOS recordings at P40, P110 and P180. At least four days after the completion of each IOS recording, the animals were each subjected to serial neurobehavioral assessments of cognitive and psychomotor functions. The testing order for behavioral assessment performed in the same animals

consisted of: Y maze (1 day), Morris water maze (MWM) with hidden platform (7 days), rotarod (1day), and self-grooming (1day). The mice were tested on one task at a time with the next behavioral test starting at least 1 day after the completion of the previous one. While Y maze, MWM and rotarod were longitudinally administered to the same animals at P40, P110 and P180 (only P110 and P180 for MWM), self-grooming has been tested only at P180. At the end of the experimental schedule, EEG electrode surgeries followed by EEG recordings were performed.

## 4.4 Open field and object recognition test (ORT)

The apparatus consisted of a square arena (60 x 60 x 30 cm) constructed in poly(vinyl chloride) with black walls and a white floor. The mice received one session of 10-min duration in the empty arena to habituate them to the apparatus and test room. Animal position was continuously recorded by a video tracking system (Noldus Ethovision XT). In the recording software an area corresponding to the centre of the arena (a central square 30 x 30 cm), and a peripheral region (corresponding to the remaining portion of the arena) were defined. The total movement of the animal and the time spent in the center or in the periphery area were automatically computed. Mouse activity during this habituation session was analysed for evaluating the behavior in the open field arena. The ORT consisted of two phases: sample and testing phase. During the sample phase, two identical objects were placed in diagonally opposite corners of the arena, approximately 6 cm from the walls, and mice were allowed 10 min to explore the objects, then they were returned to their cage. The objects to be discriminated were made of plastic, metal, or glass material and were too heavy to be displaced by the mice. The testing phase was performed either 1h or 24h after the sample phase. One of the two familiar objects was replaced with a new one, while the other object was replaced by an identical copy. The objects were placed in the same locations as the previous ones. The mice were allowed to explore objects for 5 min. To avoid possible preferences for one of two objects, the choice of the new and old object and the position of the new one were randomized among animals. The amount of time spent exploring each object (nose sniffing and head orientation within <1.0 cm) was recorded and evaluated by the experimenter blind to the mouse genotype. Arena and objects were cleaned with 10% ethanol between trials to stop the build-up of olfactory cues. Mice exploring the two objects for less than 10s during the

sample phase were excluded from testing. A discrimination index was computed as DI = (T new - T old)/(T new +T old), where T new is the time spent exploring the new object, and T old is the time spent exploring the old one [85].

## 4.5 Y maze spontaneous alternation

We used a Y-shaped maze with three symmetrical grey solid plastic arms at a 120-degree angle (26 cm length, 10 cm width, and 15 cm height). Mice were placed in the centre of the maze and allowed to freely explore the maze for 8 minutes. The apparatus was cleaned with 10% ethanol between trials to avoid the build-up of odour traces. All sessions were video-recorded (Noldus Ethovision XT) for offline blind analysis. The arm entry was defined as all four limbs within the arm. A triad was defined as a set of three arm entries, when each entry was to a different arm of the maze. The number of arm entries and the number of triads were recorded in order to calculate the alternation percentage (generated by dividing the number of triads by the number of possible alternations and then multiplying by 100[85]).

## 4.6 Morris water maze

Mice were trained for four trials per day and for a total of 7 days (11) in a circular water tank, made from grey polypropylene (diameter, 120 cm; height, 40 cm), filled to a depth of 25 cm with water (23°C) rendered opaque by the addition of a non-toxic white paint. Four positions around the edge of the tank were arbitrarily designated North (N), South (S), East (E), and West (W), which provided four alternative start positions and also defined the division of the tank into four quadrants, i.e. NE, SE, SW, and NW. A square clear Perspex escape platform (11 x 11 cm) was submerged 0.5 cm below the water surface and placed at the midpoint of one of the four quadrants. The hidden platform remained in the same quadrant during training, while the starting positions (N, S, E, or W) were randomized across trials. The pool was situated in a room containing extra-maze cues that provide specific visual reference points for locating the submerged platform. Mice were allowed up to 60 s to locate the escape platform, and their swimming paths were automatically recorded by the Noldus Ethovision system. If the mouse failed to reach the platform within 60 s, the trial was terminated, and the mouse was guided onto the platform for 15 s. On the last trial of the last training day, mice received a probe trial,

during which the escape platform was removed from the tank and the swimming paths were recorded over 60 s while mice searched for the missing platform. The swimming paths were recorded and analysed with the Noldus Ethovision system.

## 4.7 Rotarod

Motor coordination and abilities were assessed using the rotarod test as described in[191]. Animals were placed on a drum with increasing rotation speed from 4 to 40 rpm. The time spent on the drum was recorded by an automated unit, which stops as the mouse fall. Motor abilities were assessed by conducting the test for four consecutive times with an interval of 5 min in the same day.

## 4.8 Three-chamber social test

The three-chamber paradigm test has been successfully employed to study sociability and preference for social novelty in several mutant mouse lines. 'Sociability' is defined as a propensity to spend time with a conspecific, as compared to time spent alone in an identical but empty chamber; 'preference for social novelty' is defined as propensity to spend time with a new mouse rather than with a familiar mouse[192]. We adapted the protocol reported in[193]. The apparatus consisted in a rectangular, three-chamber box made from clear Plexiglas (72 cm wide x 50 cm length x 33 high). Each chamber is 24 x 50 cm and the dividing walls are made from clear Plexiglas, with an open middle section, which allows free access to each chamber. Two identical, wire cup-like containers with removable lids were placed inside the apparatus, one in each side chamber. Each container was made of metal wires allowing for air exchange between the interior and exterior of the cup but small enough to prevent direct physical interactions between the inside animal and the subject mouse. Two classes of mouse were used in this experiment, one acting as a control, naı̈ve animal, while the other is the test subject. The control mouse was a mouse of the same background, age, gender and weight, without any prior contact with the subject mouse. Two control mice were required per experiment, one used for session I (Stranger 1) and another for session II (Stranger 2). The same control mice were used between trials. Control mice were gradually habituated to wire-cup housing in the three-chamber box for 4 days (30 min per day) before the starting of test session. After 10 min of habituation in the arena with empty wire cups of the subject mouse, we placed

Stranger 1 inside one of the wire cups. The subject mice were allowed to explore each of the three chambers for 10 min (session I). Animal position was continuously recorded by a video tracking system (Noldus Ethovision XT). The amount of time spent exploring each wire cup was recorded and evaluated by the experimenter blind to the mouse genotype. A discrimination index was computed as DI = (Tsoc - Tobj)/ (Tsoc + Tobj), where Tsoc is the time spent exploring the cup housing the Stranger 1, and Tobj is the time spent exploring the other cup. In session II we placed Stranger 2 inside the wire cup in the opposite side chamber. Duration of session II was 10 min and we calculated the same DI described above, differentiating the exploration time of the subject mouse between Stranger 1 and Stranger 2. The placement of Stranger 1 and Stranger 2 in the left or right side of the box was randomized between trials. Arena and wire cups were cleaned with 10% ethanol between trials to prevent olfactory cue bias.

## 4.9 Self-grooming

Mice were scored for spontaneous grooming behaviors as described earlier[194]. Each mouse was placed individually into a clean, empty, standard mouse cage (27 cm length x 20 cm wide x 15 cm high) without bedding. Animal behaviors were videotaped for 20 min. After a 10-min habituation period in the test cage, each mouse was scored with a stopwatch for 10 min for cumulative time spent grooming all body regions.

## 4.10 Behavioral analysis of seizure severity in mice

Seizures were scored according to Racine (1972): stage 0, normal behavior; stage 1, immobility; stage 2, forelimb and/or tail extension, rigid posture; stage 3, repetitive movements, head bobbing; stage 4, forelimb clonus with rearing and falling; stage 5, continuous rearing and falling; stage 6, severe whole-body convulsions; stage 7, death. Seizure severity was scored every 10 min for 1 h after each KA injection. The maximum rating scale values reached by each animal over each 10 min interval were used to calculate the behavioral rating scale value for the different experimental groups. Similarly, severity of each seizure detected in EEG traces was established based on the inspection of video recordings, using the same scale. Seizures of stage 1 and 2 were classified as tonic events,

seizures of stage 3 were assigned to clonic events and seizures of stage 4, 5 and 6 were categorized as tonic-clonic events.

## 4.11 EEG recordings and data analysis in mice

A two-channel headmount (8201, Pinnacle Technology) for EEG recordings was placed on the skull of mice anesthetized with isoflurane (1-3%). EEG electrodes were stainless steel screws implanted epidurally over the frontal and the occipital areas. Mice were allowed to recover for at least 4-5 days with antalgic therapy (paracetamol, 100 mg/kg, *per os*). EEG signals were recorded using a preamplifier (8202-SL) connected to a data acquisition system (8206, Pinnacle Technology) and Sirenia Software 1.7.9 (Pinnacle Technology). Signals were recorded at 400 Hz sampling frequency to evaluate baseline (spontaneous) activity for 24 hours followed by treatment with i.p. kainic acid (KA) at 10 mg/kg to evoke seizure activity. Video was recorded in parallel during the entire duration of the EEG assessments. For the analysis of baseline EEG, signals were segmented in 30s epochs. The vigilance state in each epoch was manually classified as active wake, passive wake or sleep, based on the inspection of video recordings by an operator blind to the genotypes and the treatment administered. EEG signals were converted into power spectra by Fast Fourier Transform (FFT) for at least 12 epochs in each light/dark cycle and wake/sleep condition. Consecutive epochs of the same vigilance state were selected to be spaced at least 10 minutes apart between each other. The spectra were normalized to the total power of the signal. The power spectra were averaged over subjects in each light/dark cycle and wake/sleep condition at frequency ranges divided into five bands as follows: 0.5–4 (delta), 4–8 (theta), 8–12 (alpha), 12–30 (beta), and 30–45 (gamma) Hz. This part of the analysis was performed using custom software written in Matlab. A correlation matrix of EEG spectral power in $CrT^{-/y}$ and WT animals was obtained using Spearman correlation, with Benjamini-Hochberg adjustment (Python, *scipy* library). To quantify both baseline (spontaneous) and KA-evoked seizure episodes we used Sirenia Seizure Pro 1.8.4 (Pinnacle Technology). The baseline period of each animal was used as a cutoff threshold (mean line length + 8xSD). Events in the 2-10 Hz frequency range, with a line length higher than the defined threshold, and lasting at least 10 seconds were identified as seizures.

## 4.12 Patients

Five subjects with CTD aged to the present date between 7.7 and 22.7 years were diagnosed at IRCCS Stella Maris Foundation at the age ranging between 5.1 and 9 years (mean age = 7.2 years; SD = 1.8 years). Diagnosis of CTD was confirmed in all five patients, using clinical, neurochemical (Cr/Crn urine levels and lack of brain Cr in $^{1H}$MRS) and genetical assessments. Twelve healthy subjects served as age-matched controls (mean age = 7.7 years; SD = 2.3 years). Data have been anonymized using an alphanumeric code. EEG recordings were performed as part of routine examination of patients with intellectual disability and language deficits. The experiment has been subjected to approval by the Ethics Board (201/2019, Pediatric Ethics Board of Tuscany) and has been performed in accordance with the Declaration of Helsinki.

## 4.13 EEG recordings and data analysis in humans

EEG data in patients were collected using a Micromed or Grass EEG recording system. Gold ring electrodes were placed following the international 10–20 convention for a 32-channel cap and signals were recorded at a sampling rate of 500 Hz. For this analysis, we used the first EEG recorded at the time of diagnosis; thus, patients were not prescribed anticonvulsant medications yet.

EEG recordings were screened and divided into artefact-free segments (10-s duration for eyes closed condition, 20-s duration for eyes open and sleep conditions). EEG signal was then exported in European Data Format (EDF) and subjected to FFT. Power spectra were estimated by averaging at least 8 segments for each behavioral state. The spectral power values in the same frequency bands described above for mice were evaluated in humans. The spectra were normalized to the total power of the signal.

## 4.14 Intrinsic optical signal (IOS) imaging

For IOS preparations, mice were anesthetized with isoflurane (1-3%), and fixed on a stereotaxic apparatus using ear bars. Surgery was performed as previously described[102]. A thin layer of cyanoacrylate was poured over the exposed skull to affix a custom-made metal ring (9 mm internal diameter) in correspondence with the binocular visual cortex and a drop of transparent nail polish was used to improve the optical access. Mice were

left to recover for at least 72h and administered paracetamol (100 mg/kg, in drinking water). IOS recordings were performed under isoflurane (0.5-1%) and chlorprothixene anesthesia (1.5 mg/kg, i.p.) longitudinally in each animal at postnatal day (PND)40, PND110 and PND180. Images were visualized using a custom Leica microscope (Leica Microsystems). The animals were secured under the objective using a ring-shaped magnet mounted on an arduino-based imaging chamber. Red light illumination (630 nm) was obtained with 8 individually addressable LEDs (WS2812) fixed to the objective (Leica Z6 APO coupled with a Leica PanApo 2.0X 10447170) by a custom 3D printed conical holder[103]. Visual stimuli were generated using Matlab Psychtoolbox and presented on a monitor placed 13cm away from the eyes of the mouse. Sinusoidal wave gratings were presented in the binocular portion of the visual field with spatial frequency 0.03 cyc/deg, mean luminance 20cd/m 2 and contrast up to 90%. The stimulus consisted in the abrupt contrast reversal of a grating with a temporal frequency of 4Hz for 1s. Frames were acquired at 30 fps with a resolution of 512×512 pixels. The signal was averaged for at least 80 trials. Fluctuations of reflectance (R) for each pixel were computed as the normalized difference from the average baseline (ΔR/R). A region of interest (ROI) was calculated on the mean image of contralateral eye response by selecting the pixels in the lowest 30% ΔR/R of the range between the maximal and minimal intensity pixel, and mean evoked response was quantitatively estimated as the average intensity within the ROI. See[102] for further details on signal analysis.

## 4.15 Visually evoked potentials (VEPs)

Mice were anesthetized with isoflurane (1-3%), and head-fixed on a stereotaxic frame. After exposing the skull, a small craniotomy (2× 2mm) overlying the visual cortex was performed. Then, a multichannel neural probe (Q-trode tetrode configuration, Neuronexus) was slowly inserted at a depth of 150–200μm in the binocular visual cortex (coordinates: 3.2mm lateral, 0.2mm rostral with respect to lambda landmark). Signal was acquired using Cheetah 32 (Neuralynx) recording system at 30.3kHz of sampling rate with a band pass filter of 0.1–250Hz. Signal from each channel was averaged to obtain VEPs. Visual stimuli were generated using Matlab Psychtoolbox and presented on a monitor placed 20cm away from the mouse. Stimuli consisted in sinusoidal wave gratings with spatial frequency 0.03 cyc/deg, temporal frequency 2Hz, mean luminance 25cd/m 2

and contrast 90%. VEP responses were averaged for at least 100 trials per eye. The amplitude of VEP response was calculated as the peak to baseline difference of the first positive component (at ~100 ms).

## 4.16 Machine learning-based classification

Scikit-learn, a Python-based library (http://scikit-learn.org/stable/), was used to compute both principal component analysis (PCA) and train the classification model. The model is a supervised machine learning algorithm called Random Forest (RF) that is based on multiple decision tree learning. We used the Scikit-learn implementation for this algorithm, called ExtraTreesClassifier function. To determine an optimal set of hyparameters for the classifier we used the function RandomizedSearchCV on the dataset with all the variables.

Then, we applied the RF classifier adopting the function cross_val_score with cv = 3 to perform 3-fold cross-validation. To calculate feature importance in classifier decision, we used the attribute feature_importance that is an instance of the ExtraTreesClassifier expressing the fraction of relative importance for each feature. Data from all ages of phenotyping (PND40, PND110 and PND180) were combined together.

## 4.17 Biochemical analysis

For Cr and GAA assay, mouse tissues, immediately frozen on dry ice and stored at -80 C until the analysis, were homogenized in 0.7 ml PBS buffer (Sigma-Aldrich, Italy) at 4 C using a ultrasonic disruptor (Microson Heat System, NY, USA) for brain or a glass manual homogenizer (VWR, Italy) for kidney, heart and muscle. After centrifugation (600 g for 10 min at 4 C) an aliquot of the homogenate (50 ml) was assayed for protein content and the supernatant used for Cr assay as previously described[195]. Briefly, 50 ml of saturated sodium hydrogen carbonate and 50 ml of a mixture containing 2-phenylbutyric acid (I.S.) in toluene (6.09 mmol/l; Sigma-Aldrich, Italy) were added to 200 ml of homogenate or to 100 ml of serum and urine, respectively. After adding 1 ml of toluene and 50 ml of hexafluoro-2,4-pentanedione (Sigma-Aldrich, Italy) to form bistrifluoromethyl-pyrimidine derivatives, the mixture was stirred overnight at 80 C. The organic layer was centrifuged, dried under nitrogen and 2 ml of the residue derivatized at

room temperature with 100 ml of BSTFA + TMCS (Sigma-Aldrich, Italy) injected into the Gas Chromatography/Mass Spectrometry (GC/ MS) instrument. GC analyses were performed using an Agilent 6890N GC equipped with an HP5MS capillary column (0.25 mm  30 m, film thickness 0.25 ım) and an Agilent mass spectrometer 5973N (Agilent Technologies, Italy). The mass spectrometer was set in EI- single ion monitoring mode (SIM). The ions with m/z of 192 for I.S., 258 for Cr and 225 for guanidinoacetic acid (GAA) were used for calculation of the metabolites, using standard curves ranging 5–90 mmol/l and 0.30–6 mmol/l for Cr and GAA, respectively. Data were processed by the G1701DA MSD ChemStation software. All the aqueous solutions were prepared using ultrapure water produced by a Millipore system.

## 4.18 Immunohistochemistry

Animals were perfused transcardially with 4% paraformaldehyde in phosphate buffer. Brains were post-fixed and impregnated with 30% sucrose in phosphate buffered saline (PBS). Coronal brain sections (40 mm) were cut on a freezing microtome and collected in PBS before being processed for immunohistochemistry. After a blocking step, free-floating slices were incubated O/N at 4°C in a solution of primary antibody (NeuN, Millipore, 1:500; Ki67, Abcam, 1:400; DCX, Abcam, 1:200; vGlut1, Synaptic System, 1:500; vGAT, Synaptic System, 1:1,000; Iba-1, Wako, 1:400) and antigen-antibody interaction was revealed with suitable Alexa Fluor-conjugated secondary antibodies (1:400, Invitrogen). Immunostaining for Ki67 involved an additional treatment with sodium citrate for antigen retrieval. Sections were then counterstained with Hoechst dye (1:500, Sigma), mounted on microscope slides and coverslipped using Vectashield mounting medium for fluorescence (Vector Laboratories Inc.).

## 4.19 Image analysis

NeuN and Iba1- To quantify the density of neuronal and microglial cells in the cerebral cortex we used the StereoInvestigator software (MicroBrightField) equipped with motorized X–Y sensitive stage and video camera connected to a computerized image analysis system. NeuN-positive cells were counted using 20x magnification and sampling boxes (250 x 250 x 40 um) located in both superficial and deep layers of PFC and ACC cortex. Iba1- positive cells were counted using 40x magnification and sampling boxes (250

x 250 x 40 um) located in both superficial and deep layers of PFC cortex. Cell density was calculated by averaging values obtained from at least 6-8 counting boxes per animal.

Ki67 and DCX- Examination of Ki67 and DCX-positively labelled cells was confined to the hippocampal dentate gyrus (DG), specifically to the granule cell layer (GCL) and the subgranular zone of the hippocampus defined as a two-cell body-wide zone along the border between the GCL and hilus. Quantification of Ki67 or DCX-immunoreactive cells was conducted from 1-in-6 series of immunolabeled sections using 20x magnification and spanning the rostrocaudal extent of DG. All immunostained sections were analysed using the StereoInvestigator software. The reference volume was determined as the sum of the traced areas multiplied by the distance between the sampled sections. Densities of immunopositive cells were then calculated by dividing the number of positive cells by the reference volume. Numbers of positively labelled neurons were normalized as density per unit of volume (mm3 ).

vGlut1 and vGAT- To quantify the density of vGlut1- and vGAT-positive puncta, the parameters of acquisition (laser intensity, gain, offset) were optimized at the beginning of the acquisition and then held constant throughout image acquisition. All sections were acquired in random order in a single session to minimize fluctuation in laser output and degradation of fluorescence. We imaged superficial and deep layers of PFC and ACC on a Zeiss laser-scanning Apotome microscope using a 63x oil immersion objective. For each section, we imaged serial optical sections at 0.33 lm intervals for a total of at least 15 optical sections (5 um). From each animal we imaged 6 sections (3 in superficial layers and 3 in deep layers). Maximum intensity projections (MIPs) were generated from the group of 5 consecutive sections yielding the higher mean pixel intensity. These MIPs were imported in ImageJ and quantified using Puncta analyzer plugin[196]. The number of positive puncta was measured within the entire acquired area.

## 4.20 Determination of lipofuscin accumulation by autofluorescence

Coronal brain sections were mounted on microscope slides and coverslipped using Vectashield mounting medium for fluorescence (Vector Laboratories Inc.). We imaged hippocampal DG on a Zeiss laser-scanning Apotome microscope using a 40 oil immersion objective. The parameters of acquisition were optimized at the beginning of the

experiment and then held constant. Lipofuscin level was measured as the presence of autofluorescence at 550 nm in the region of interest. For each section, we imaged serial optical sections at 0.5 lm intervals for a total of at least 80 optical sections (40 um). From each animal we imaged 3–4 sections. MIPs were generated from the group of 5 consecutive sections yielding the higher mean pixel intensity. These MIPs were imported in ImageJ and quantified using Threshold plugin. The area of positive puncta and mean pixel intensity were measured within the entire acquired area.

## 4.21 Statistical analysis

All statistical analyses were performed using GraphPad Prism 8.0.1. Differences between two groups were assessed with a two-tailed t-test. Multiple t-test was used for the analys of EEG spectral power. The significance of factorial effects and differences among more than two groups were evaluated with ANOVA/RM ANOVA followed by post hoc Holm-Sidak test. Rank transformation was exploited for data not normally distributed. The level of significance was $p < 0.05$ or as otherwise stated in the Figure Legends.

# 5. FIGURES

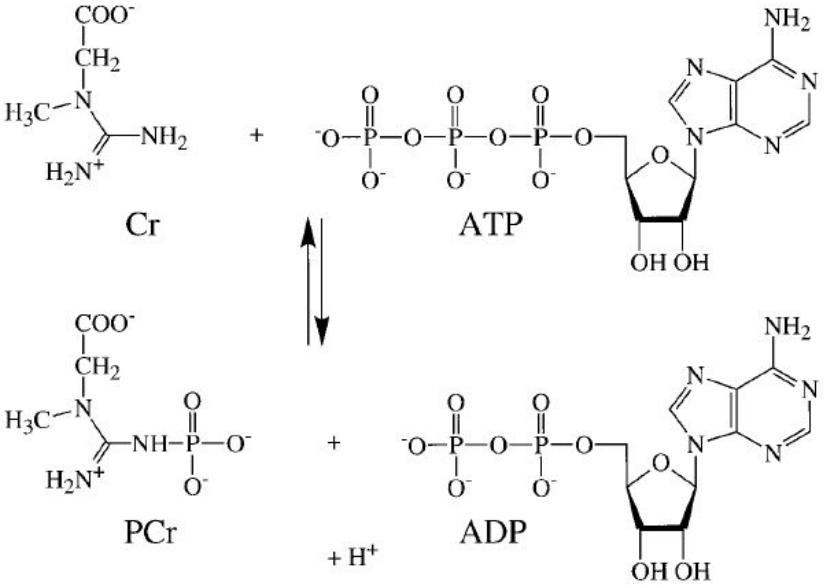


**Fig. 1: The creatine cycle.**

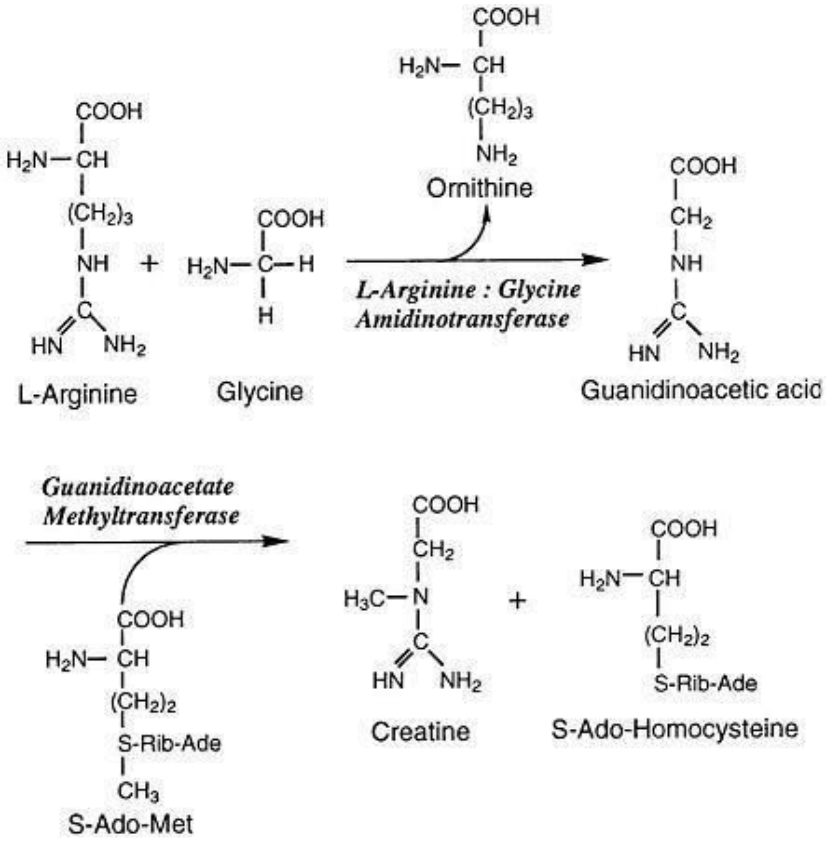


**Fig. 2: The synthesis of creatine.**

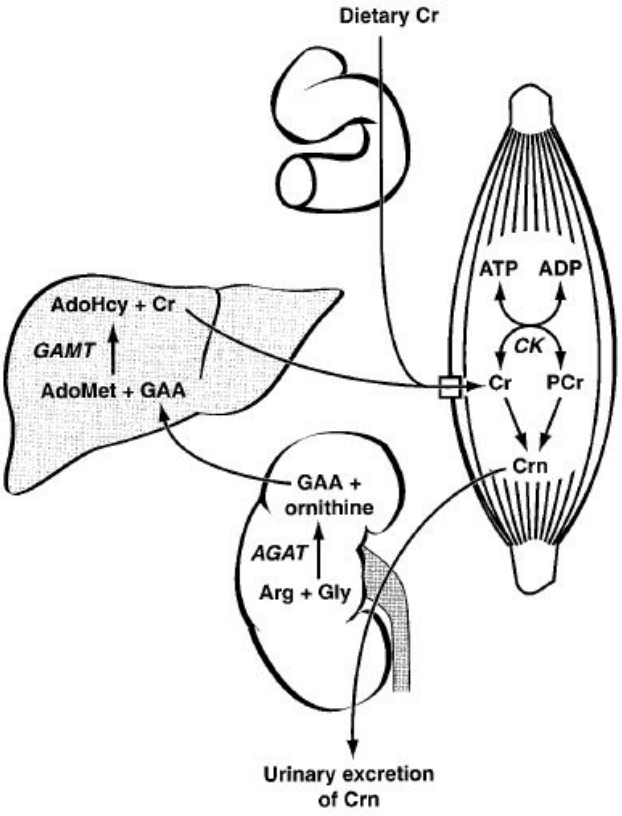


**Fig. 3: Hypothesized model of Cr synthesis in mammals** (Wyss & Kaddurah-Daouk 2000).

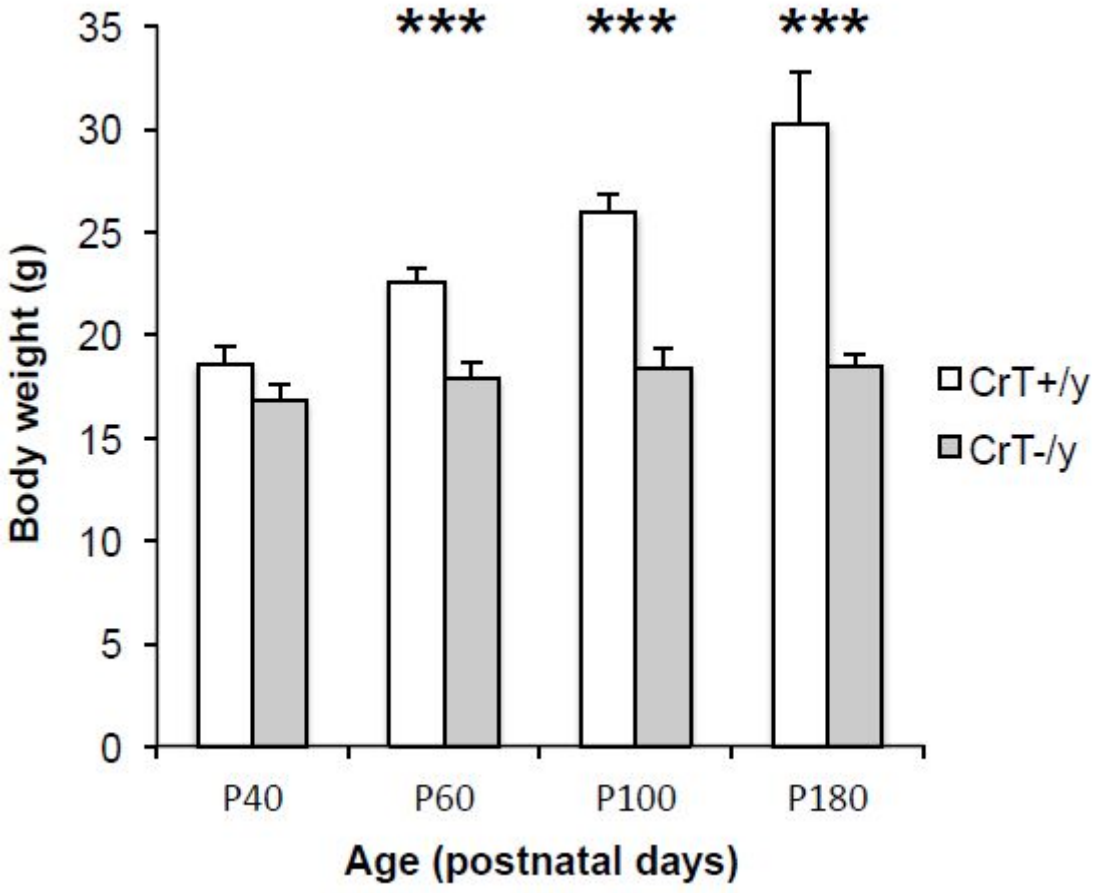


**Fig. 4: reduced body weight in CrT$^{-/y}$ mice** (n = 13; Two way ANOVA on rank transformed data, P < 0.001 effect of genotype, P < 0.001 interaction between genotype and age; post hoc Holm Sidak method, P = 0.092 at P40, P < 0.001 in all other comparisons)

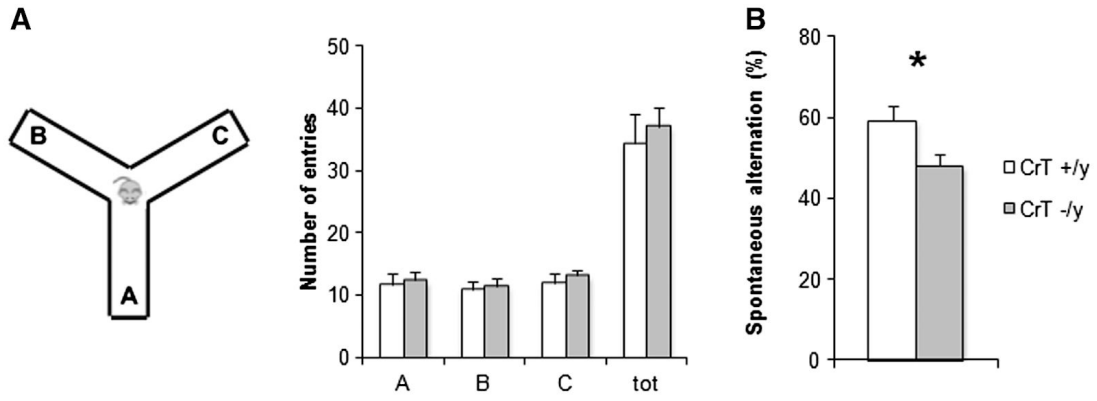


**Fig. 5: Early deficiency of working memory in CrT$^{-/y}$ mice.** (A) Schematic diagram of the Y maze apparatus. The mean number of entries in the single arms of the maze (A, B, C) and the total number of arm entries were comparable for the different experimental groups (Two-Way ANOVA on rank transformed data, post hoc Holm-Sidak method, $p = 0.506$, $p = 0.941$, $p = 0.276$, $p = 0.391$, respectively). (B) Alternation rate in the Y maze was significantly lower in CrT$^{-/y}$ mice (n=9) compared to that recorded for CrT$^{+/y}$ littermates (n = 11; t test, $p < 0.05$) at P28. *$p < 0.05$. Error bars, SEM.

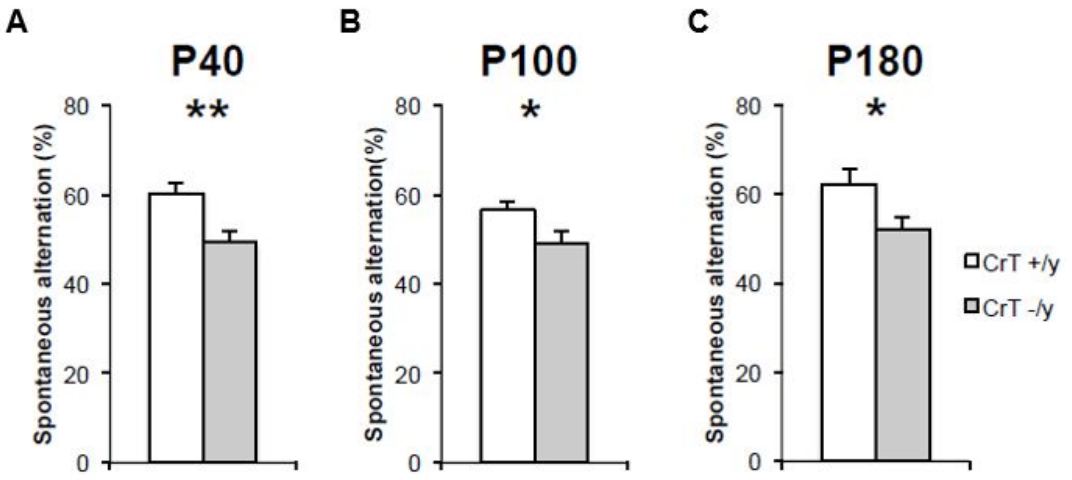


**Fig. 6: Impaired working memory in $CrT^{-/y}$ mice.** Alternation rate in the Y maze was significantly lower in $CrT^{-/y}$ mice compared to that recorded for $CrT^{+/y}$ littermates at P40 ($CrT^{+/y}$, n = 13, $CrT^{-/y}$, n = 12; t-test, $p < 0.01$, panel a), P100 ($CrT^{+/y}$, n = 13, $CrT^{-/y}$, n = 12; t-test, $p < 0.05$, panel b) and P180 ($CrT^{+/y}$, n = 9, $CrT^{-/y}$, n = 7; t-test, $p < 0.05$, panel c). * $p < 0.05$; ** $p < 0.01$. Error bars, SEM.

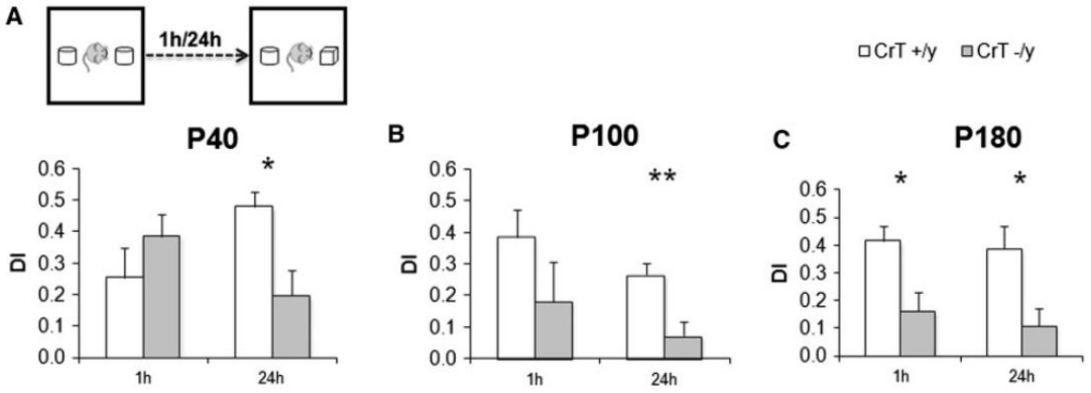


**Fig. 7: Progressive impairment of object recognition memory in CrT$^{-/y}$ mice.** Top, a schematic representation of the object recognition task. Histograms display object discrimination indexes of CrT$^{+/y}$ and CrT$^{-/y}$ during the testing phase performed after a delay of 1 and 24h since the sample phase at different ages. (A) P40. While both experimental groups can recognize the new object in the test at 1h (t-test, $p = 0.285$), a significantly lower discrimination index was found in CrT$^{-/y}$ mice ($n = 9$) compared to CrT$^{+/y}$ animals ($n = 7$; t-test, $p < 0.05$). (B) P100. Even if still not significant, the recall capacity of CrT$^{-/y}$ animals at 1h was reduced (t-test, $p = 0.242$). At 24h, a t-test revealed that the performance of CrT$^{-/y}$ animals ($n = 11$) was strongly impaired with respect to controls ($n = 10$; $p < 0.01$). (C) P180. A significant deficit of both short (t-test, $p < 0.05$) and long-term (t-test, $p < 0.05$) memory was detected in mutant mice ($n = 10$) compared to controls ($n = 9$). *$p < 0.05$; **$p < 0.01$. Error bars, SEM.

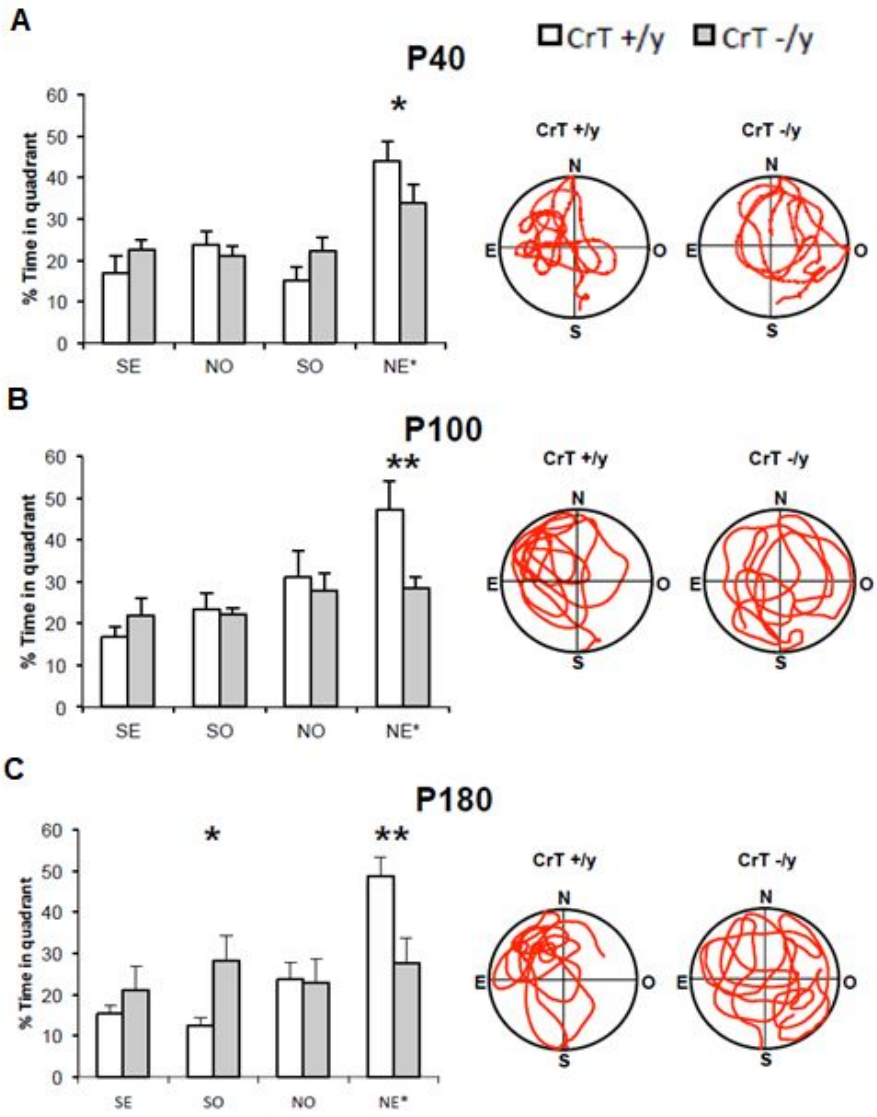


**Fig. 8: Spatial memory impairment in CrT$^{-/y}$ mice.** A Two-Way RM ANOVA followed by Holm-Sidak multiple comparison revealed that while CrT$^{+/y}$ spent significantly more time in the NE* quadrant than in the other ones, CrT$^{-/y}$ did not show any preference for the target quadrant at P40 (CrT$^{+/y}$, n = 10, CrT$^{-/y}$, n = 12; panel a), P100 (CrT$^{+/y}$, n = 7, CrT$^{-/y}$, n = 8; panel b) and P180 (CrT$^{+/y}$, n = 9, CrT$^{-/y}$, n = 7; Two-Way RM ANOVA, post hoc Holm-Sidak method, panel c). At all ages tested, the percentage of time spent in the target quadrant was shorter in CrT$^{-/y}$ mice than in the control group (Two-Way RM ANOVA, post hoc Holm-Sidak method, $p < 0.05$ at P40 and $p < 0.01$ at P100 and P180). At P180, a significant difference was also detected in the percentage of time spent in the SO quadrant by CrT$^{+/y}$ and CrT$^{-/y}$ mice ($p < 0.05$). * $p < 0.05$; ** $p < 0.01$. Error bars, SEM.

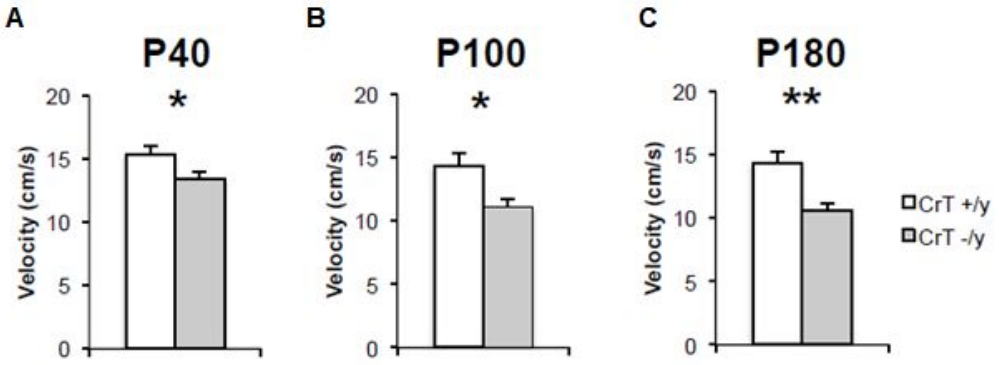


**Fig. 9: Slower swimming velocity in CrT$^{-/y}$ mice.** Mean swimming speed measured all along the training phase of the Morris water maze for CrT$^{+/y}$ and CrT$^{-/y}$ animals at P40 (CrT$^{+/y}$, n = 10, CrT$^{-/y}$, n = 12; panel a), P100 (CrT$^{+/y}$, n = 7, CrT$^{-/y}$, n = 8; panel b) and P180 (CrT$^{+/y}$, n = 9, CrT$^{-/y}$, n = 7; panel c). At all ages tested mutant mice resulted to be slower swimmers with respect to control littermates (t-test, $p < 0.05$ at P40 and $p < 0.01$ at P180; Mann-Whitney Rank Sum test, $p < 0.05$ at P100). * $p < 0.05$; ** $p < 0.01$. Error bars, SEM.

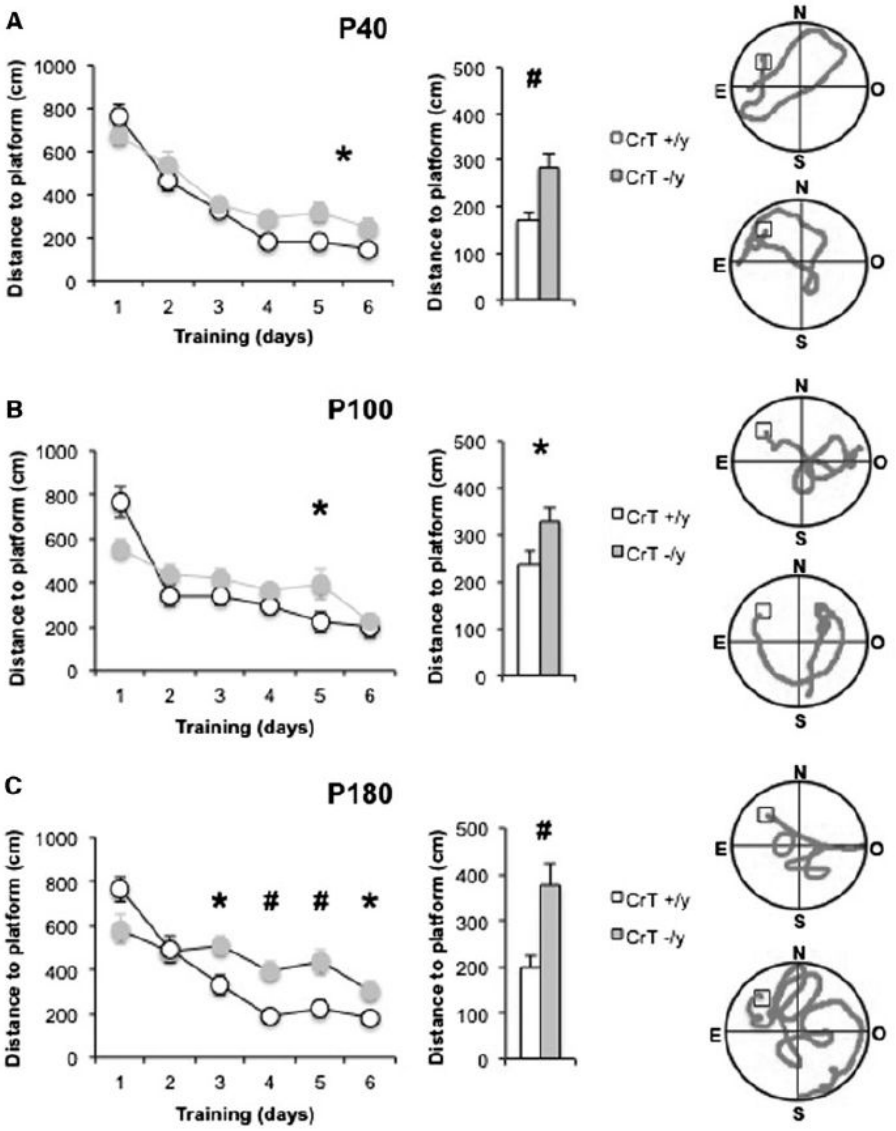


**Fig. 10: CrT deletion progressively deteriorates spatial learning and memory in mutant mice.** (A) Left, learning curves for $CrT^{+/y}$ (n = 10, white) and $CrT^{-/y}$ mice (n = 12, grey) at P40. A significant difference was detected at day 5 (Two-Way RM ANOVA, post hoc Holm-Sidak method, $p < 0.05$). Right, histograms showing the mean swimming path covered to locate the submerged platform on the last three days of training for the two groups. A significant difference between $CrT^{-/y}$ and $CrT^{+/y}$ animals was present (t-test, $p < 0.01$). Representative examples of swimming path during the day 3 of the training phase for a $CrT^{+/y}$ (top) and a $CrT^{-/y}$ mouse (bottom) are also reported. (B) Left, learning curves for $CrT^{+/y}$ (n = 7, white) and $CrT^{-/y}$ mice (n = 8, grey) at P100. A significant difference was detected at day 5 (Two-Way RM ANOVA, post hoc Holm-Sidak method, $p < 0.05$). Right, histograms showing the mean swimming path on

the last three training days for the two groups. A significant difference between $CrT^{+/y}$ and $CrT^{-/y}$ animals was present (t-test, $p < 0.05$). Representative examples of swimming path during the day 3 of the training phase for a $CrT^{+/y}$ (top) and a $CrT^{-/y}$ mouse (bottom) are also reported. (C) Left, learning curves for $CrT^{+/y}$ (n = 9, white) and $CrT^{-/y}$ mice (n = 7, grey) at P180: mutant mice were poorer learners with respect to control littermates and a significant difference was detected at day 3, 4, 5 and 6 (Two-Way RM ANOVA on rank transformed data, post hoc Holm-Sidak method, $p < 0.05$ for day 3 and 6, $p < 0.01$ for day 4 and 5). Right, histograms showing the mean swimming path on the last three days of training. A t-test analysis showed a statistical difference between $CrT^{+/y}$ and $CrT^{-/y}$ animals ($p < 0.01$). Representative examples of swimming path during the day 3 of the training phase for a $CrT^{+/y}$ (top) and a $CrT^{-/y}$ mouse (bottom) are also depicted. $^{*}p < 0.05$; #$p < 0.01$. Error bars, SEM.

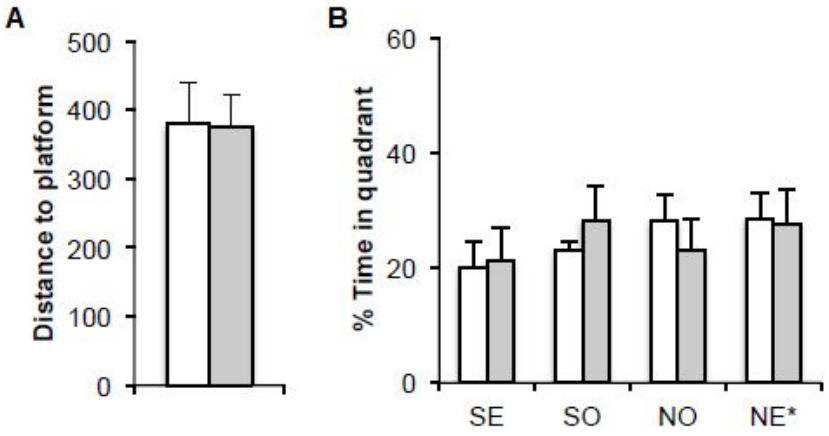


**Fig. 11: Premature cognitive decline in CrT null mice.** (a) No difference was found in the mean swimming path on the last three days of training between P365 $CrT^{+/y}$ (n = 4) and P180 $CrT^{-/y}$ animals (n = 7; t-test, p = 0.968). (b) In the probe test, the percentage of time spent in the different two quadrants was totally comparable in P180 $CrT^{-/y}$ mice and six-month older $CrT^{+/y}$ animals (Two-Way RM ANOVA, p = 0.479). Error bars, SEM.

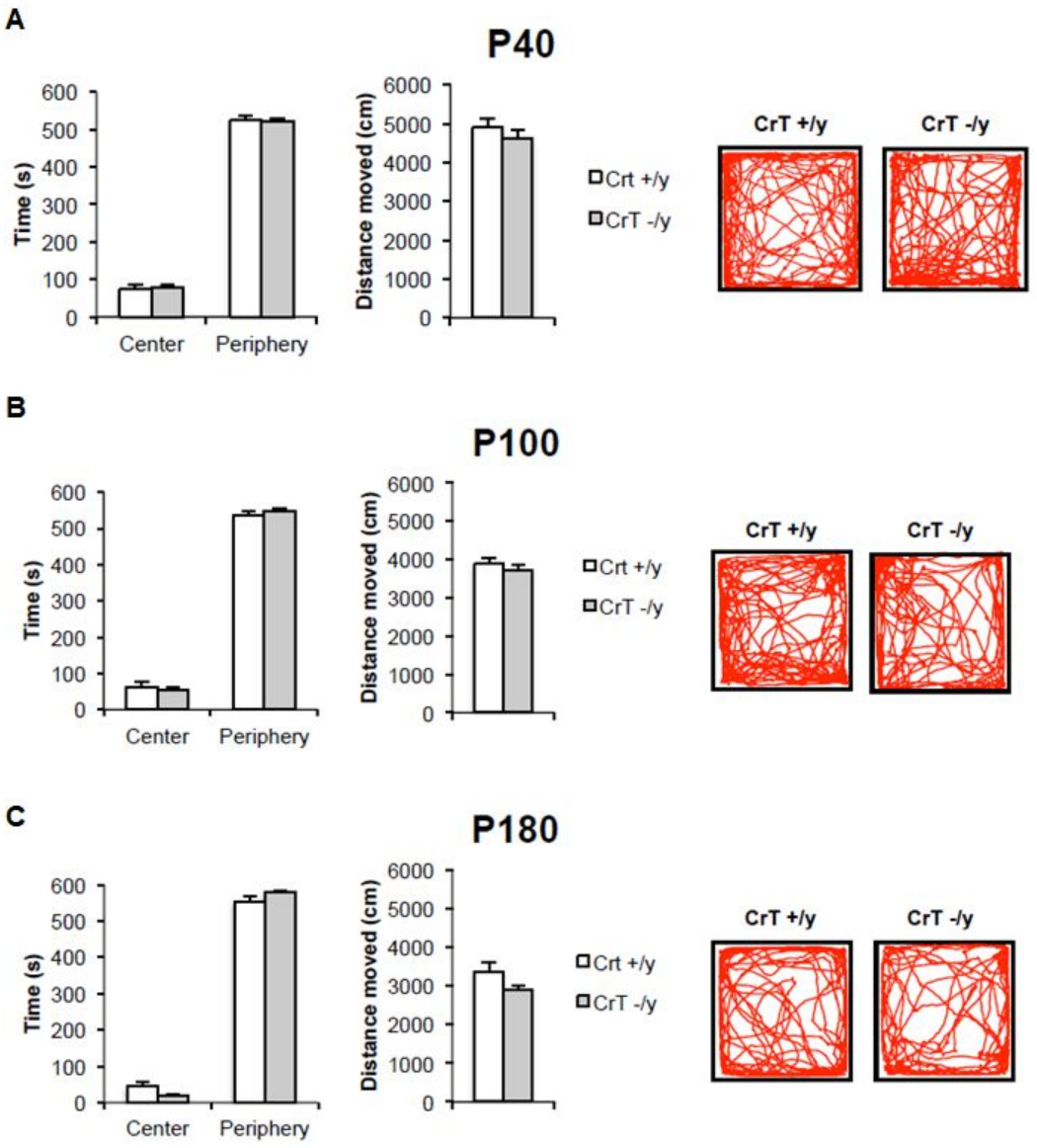


**Fig. 12: Normal behavior of CrT mutant mice in the open field arena.** Left, $CrT^{+/y}$ and $CrT^{-/y}$ mice spent a comparable amount of time in the center and in the peripheral region of the open field arena. A Two-Way ANOVA analysis shows no significant effect of genotype at P40 ($CrT^{+/y}$ n = 13, $CrT^{-/y}$ n = 12; p = 0.725; panel A), P100 ($CrT^{+/y}$, n = 13, $CrT^{-/y}$, n = 12; p = 0.508; panel B) and P180 ($CrT^{+/y}$, n = 11, $CrT^{-/y}$, n = 11; panel c; p = 0.348). Right, total distance moved did not differ between CrT mutants and wild-type animals at all ages tested (t-test, p = 0.363, p = 0.452 and p = 0.101, respectively). Representative examples of movement path during the open field session for a $CrT^{+/y}$ and a $CrT^{-/y}$ mouse are also reported. Error bars, SEM.

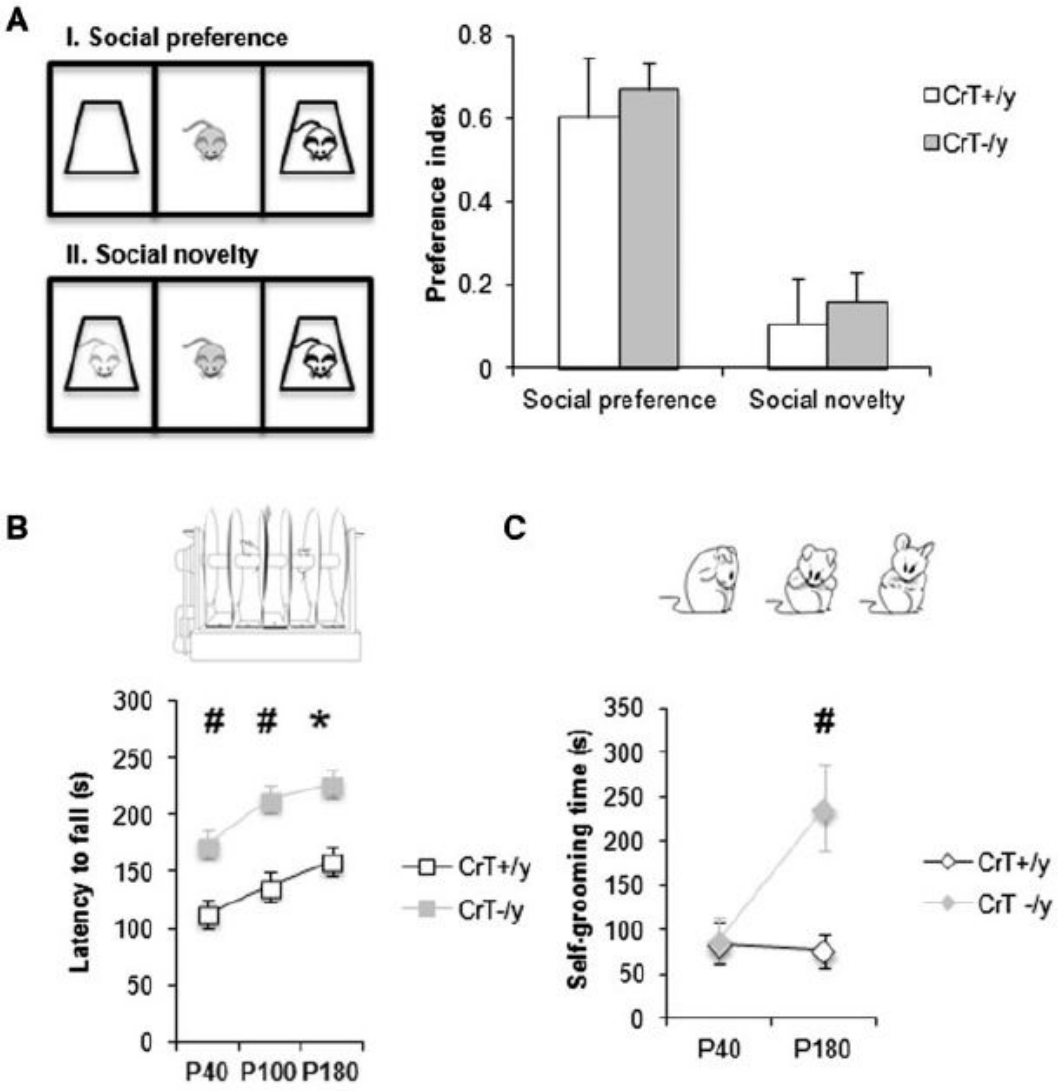


**Fig. 13: CrT mutation enhances repetitive and stereotyped behaviors.** (A) Social interaction behaviors in $CrT^{-/y}$ mice. Histograms display discrimination indexes of $CrT^{+/y}$ (n = 6) and $CrT^{-/y}$ (n = 8) mice during the social preference (session I) and the social novelty phase (session II). No difference was detected between the two groups (Mann–Whitney Rank Sum test, P>0.662 for session I; t-test, p = 0.784 for session II). A schematic representation of the three-chamber test is also depicted. (B) Performance of littermate wild-type (n = 11) and $CrT^{-/y}$ mice (n = 9) on the accelerating rotarod. Inset shows an illustration of the rotarod apparatus. A two-way ANOVA showed a significant effect of genotype ($p < 0.001$). Post hoc Holm-Sidak test revealed that the fall latency of mutant animals was significantly different from that of wild-type mice at all ages tested ($p < 0.01$ at P40 and P100, $p < 0.05$ at P180). (C) Histograms display mean time spent self-grooming in $CrT^{+/y}$ and $CrT^{-/y}$ animals at P40 and P180. While no difference was

detected at P40 ($CrT^{+/y}$, n = 7; $CrT^{-/y}$, n = 9; Two Way ANOVA on rank transformed data, post hoc Holm-Sidak method, p = 0.912), CrT null mice exhibit increased grooming behavior at P180 ($CrT^{+/y}$, n = 11; $CrT^{-/y}$, n = 7; $p < 0.01$). A schematic representation of self-grooming behavior is reported. *$p < 0.05$; #$p < 0.01$. Error bars, SEM.

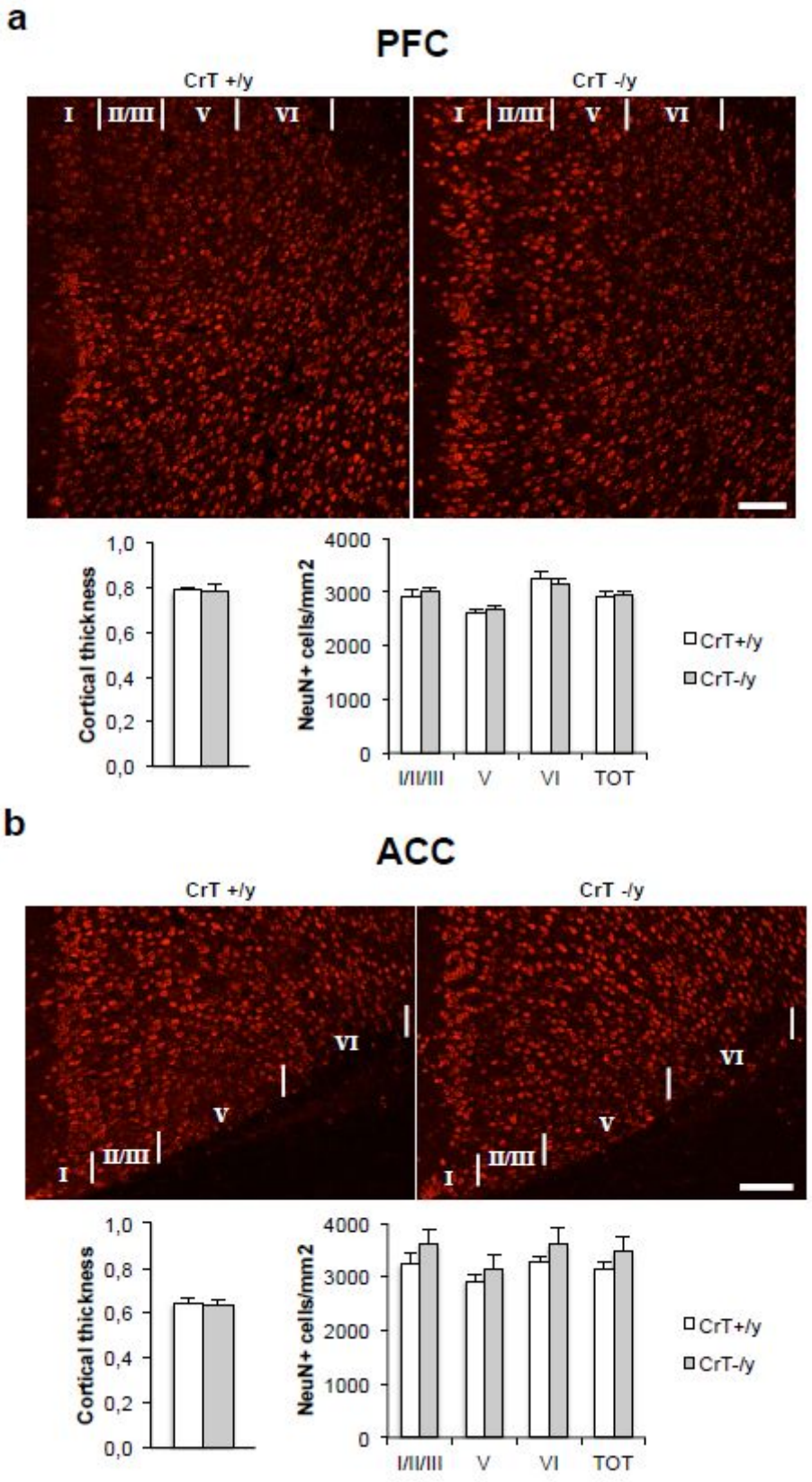


**Fig. 14: Morphological characterization of cerebral cortex in $CrT^{+/y}$ and $CrT^{-/y}$ animals at P180.** (n = 6 for both groups). (a) Left, cortical thickness of prefrontal cortex

was comparable in the two groups of animals (t-test, p = 0.838). Right, no difference in neuronal cell density measured in different layers (layer I/II/III, layer V, layer VI) and in the entire cortical thickness was detected between $CrT^{+/y}$ and $CrT^{-/y}$ mice (Two-Way ANOVA, post hoc Holm-Sidak method, p = 0.414, p = 0.670, p = 0.526 and p = 0.837, respectively). (b) Left, cortical thickness of cingulate cortex was similar in the two experimental groups (t-test, p = 0.824). Neuronal cell density measured in different layers and in the entire cortical thickness was not different in the two groups (Two- Way ANOVA, post hoc Holm-Sidak method, p = 0.197, p = 0.454, p = 0.302 and p = 0.262, respectively). Representative immunostaining for NeuN from PFC and ACC of a $CrT^{+/y}$ and a $CrT^{-/y}$ mouse are also reported. Calibration bars: 100 μm. Error bars, SEM.

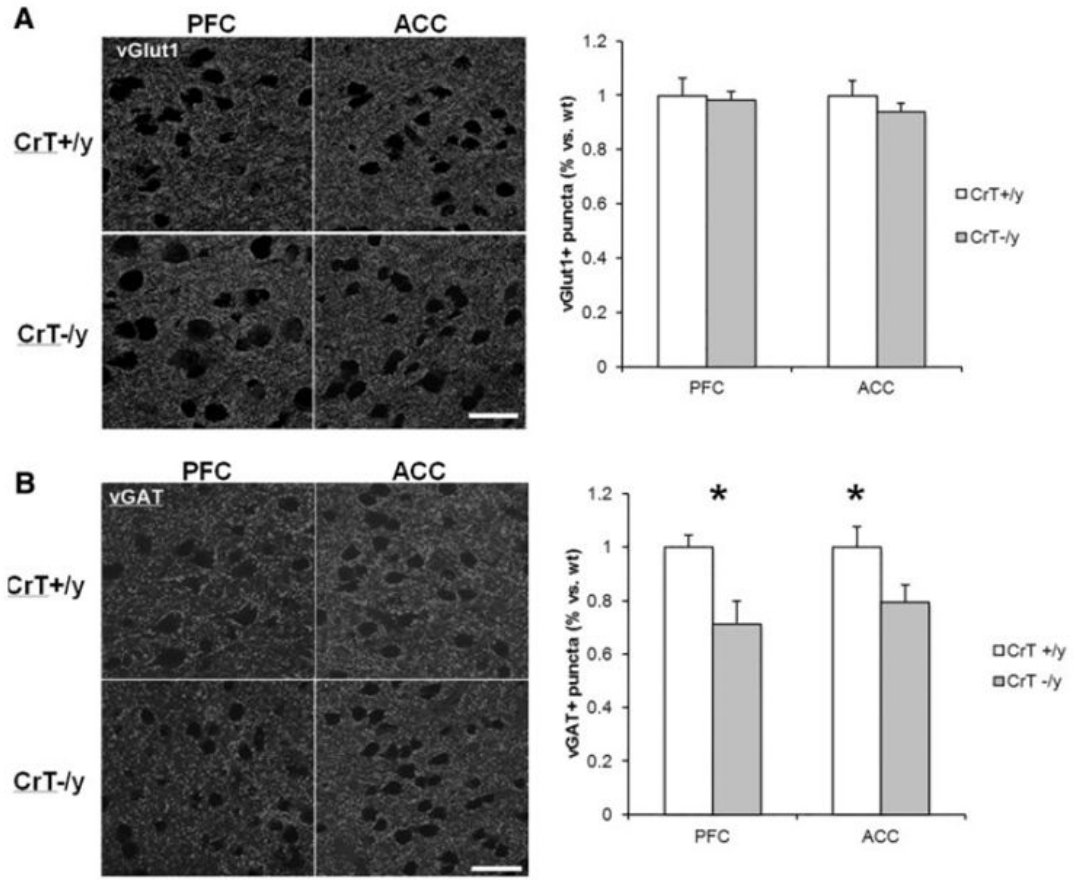


**Fig. 15. Synaptic neurotransmission in CrT$^{+/y}$ and CrT$^{-/y}$ animals at P180.** (A) Left, representative immunostaining for vGlut1 from PFC and ACC of a CrT$^{+/y}$ and a CrT$^{-/y}$ mouse. Right, no difference in vGlut1 staining was detected between the two experimental groups (n = 6 for both groups) either in PFC (t-test, p = 0.792) or ACC (t-test, p = 0.340). (B) Left, representative immunostaining for vGAT from PFC and ACC of a CrT$^{+/y}$ and a CrT$^{-/y}$ mouse. The number of vGAT-positive puncta was significantly reduced both in the PFC and the ACC of mutant animals (n = 9) with respect to controls (n = 8; t-test, p < 0.05 for both comparisons). *p < 0.05. Calibration bars: 25 lm. Error bars, SEM.

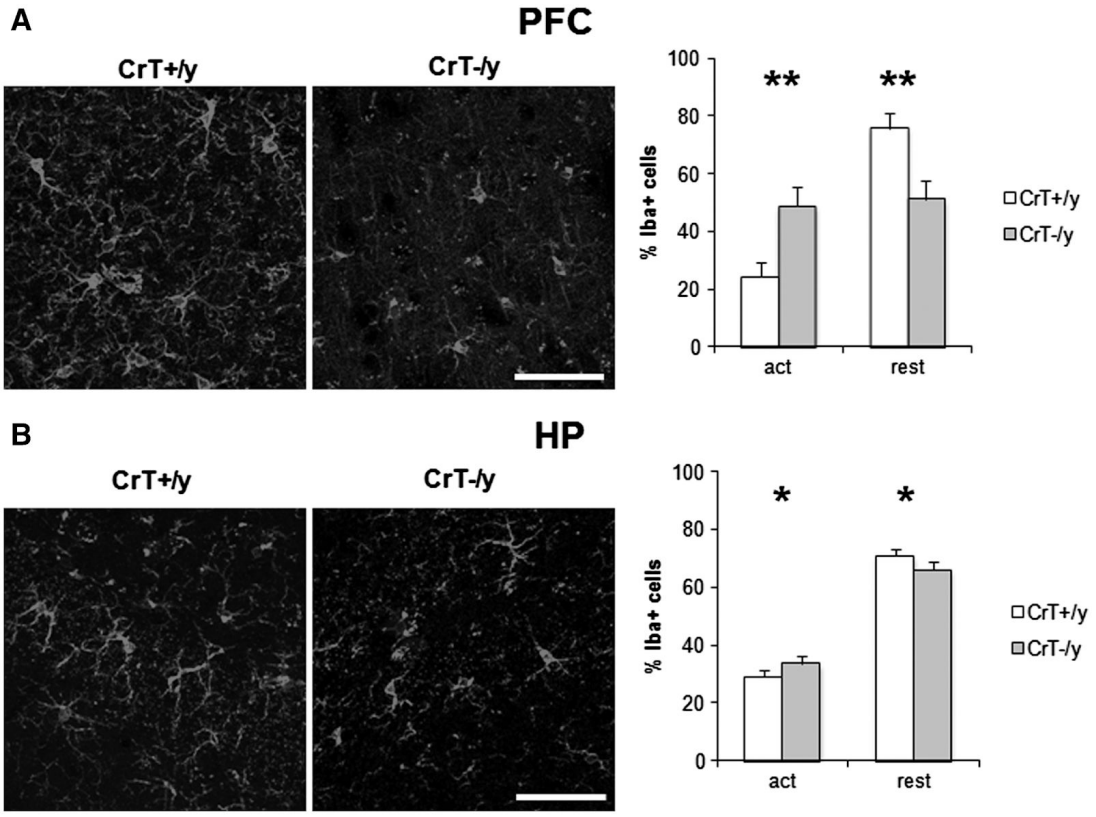


**Fig. 16: Pathological activation of microglial cells in CrT$^{-/y}$ animals.** (**A**) Left, representative immunostaining for Iba-1 from prefrontal cortex (PFC) of a CrT$^{+/y}$ and a CrT$^{-/y}$ mouse. Right, a significant increase of the percentage of activated microglial cells, with a parallel decrease of resting microglia, was detected in mutant mice with respect to wild-type animals ($n=8$ for both groups; Two Way ANOVA, post hoc Holm Sidak method, $P<0.01$). (**B**) Left, representative immunostaining for Iba-1 from the hippocampus (HP) of a CrT$^{+/y}$ and a CrT$^{-/y}$ mouse. Right, the percentage of activated microglia was increased in mutant mice, whereas the relative number of resting cells was reduced compared to controls ($n=8$ for both groups; Two Way ANOVA, post hoc Holm Sidak method, $P<0.05$). *$P<0.05$; **$P<0.01$. Calibration bar: 100 μm. Error bars, s.e.m.

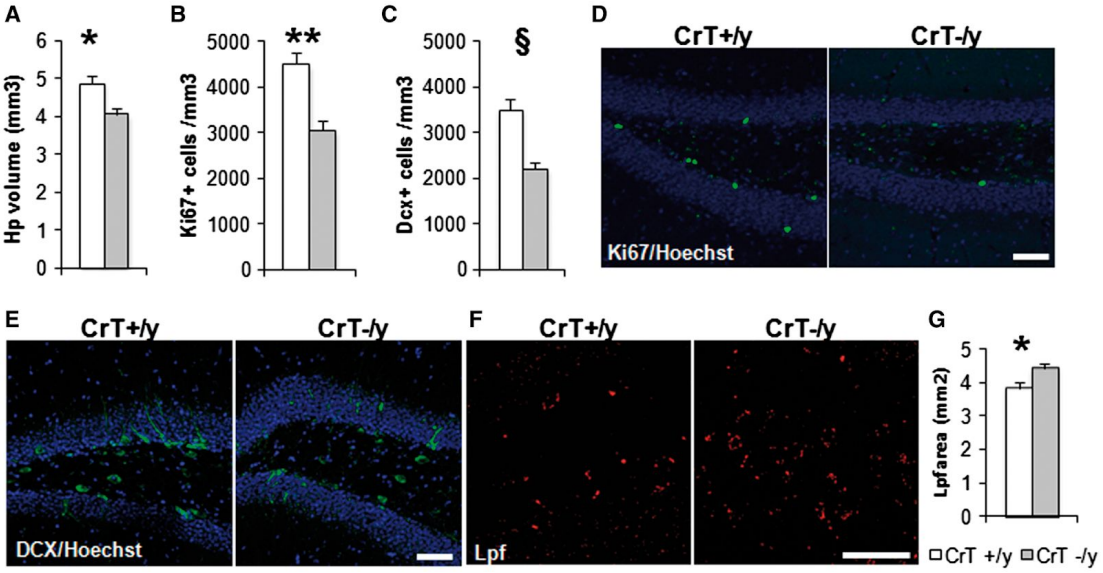


**Fig. 17: Neurogenesis impairment and enhanced lipofuscin accumulation in the hippocampus of CrT$^{-/y}$ animals at P180.** (**A**) The hippocampal volume of CrT$^{-/y}$ mice was smaller compared to CrT$^{+/y}$ mice ($n=6$ for both groups; *t*-test, $P<0.05$). (**B**) Stereological counting revealed that the density of Ki67-positive cells was significantly reduced in the DG of CrT$^{-/y}$ mice, with approximately 30% reduction with respect to wild-type littermates ($n=6$ for both groups; *t*-test, $P<0.01$). (**C**) A significant decrease of the DCX-positive immature neurons was detected in the hippocampus of adult CrT$^{-/y}$ mice compared to controls ($n=6$ for both groups; *t*-test, $P<0.001$). (**D**) Representative immunostaining for Ki-67, a nuclear protein required for cellular proliferation, from a CrT$^{+/y}$ and a CrT$^{-/y}$ mouse. (**E**) Representative immunostaining for DCX, a microtubule-associated phosphoprotein expressed in early neuronal differentiation, from a CrT$^{+/y}$ and a CrT$^{-/y}$ mouse. (**F**) Representative images for lipofuscin autofluorescence from a CrT$^{+/y}$ and a CrT$^{-/y}$ mouse. (**G**) Six-month-old CrT$^{-/y}$ mice ($n=6$) show extensive accumulation of autofluorescent material throughout the brain when compared to the wild-type control ($n=5$). A significant increase of abnormal autofluorescent storage was mainly found in DG granular and polymorph layer of CrT$^{-/y}$ mice (*t*-test, $P<0.05$). $^{*}P<0.05$; $^{**}P<0.01$; §$P<0.001$. Calibration bars: 50 μm. Error bars, s.e.m.

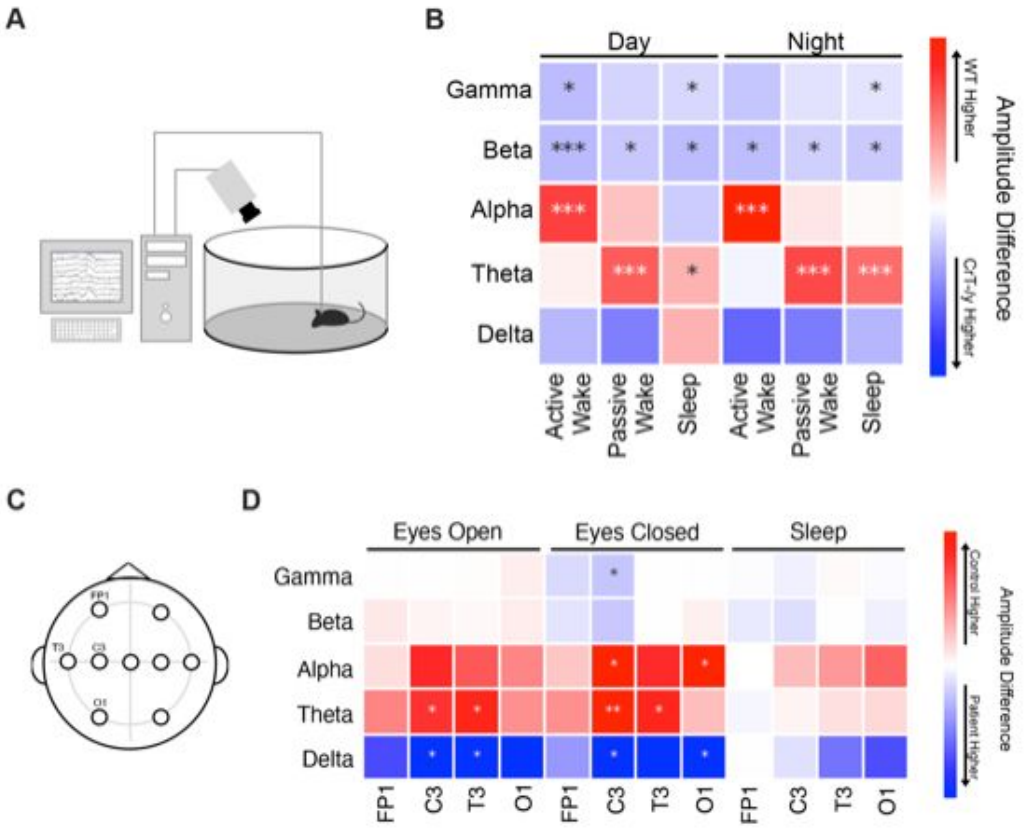


**Fig. 18. Altered neural oscillations in CrT$^{-/y}$ mice. (A)** Schematic diagram of the apparatus used for video-EEG recordings in awake, freely-moving mice. **(B)** The patch color indicates the relative difference between WT and CrT$^{-/y}$ mice in the amplitude of EEG power bands, measured in three different behavioral states (active wake, passive wake and sleep) both during the day and the night phase. A single asterisk or a triple asterisk in the colored patch indicates $p < 0.05$ and $p < 0.001$ (multiple t-test, corrected using the Benjamini, Krieger and Yekutieli procedure), respectively. **(C)** Schematic diagram of electrode location in the 10-20 international system for EEG recordings. We used this electrode configuration for EEG recordings in CTD patients and age-matched controls. Electrodes used for the analysis were FP1 (frontopolar 1), C3 (central 3), T3 (temporal 3) and O1 (occipital 1). **(D)** The patch color indicates the relative difference between healthy controls and CTD patients in the amplitude of EEG power bands, measured in three different behavioral states (eyes open, eyes closed and sleep). A single asterisk or a double asterisk in the colored patch indicates $p < 0.05$ and $p < 0.01$ (multiple t-test), respectively.

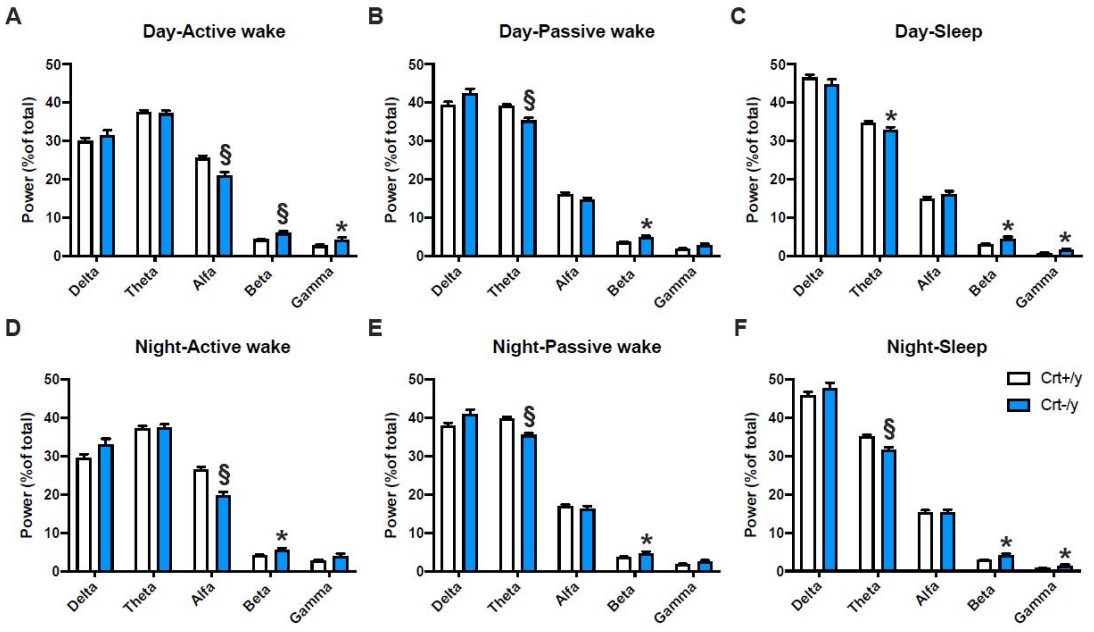


**Fig. 19. Details of alterated neural oscillations in CrT$^{-/y}$ mice during the light and the dark phase**. Normalized power spectrum of cortical EEG recordings from adult WT CrT$^{+/y}$ (n = 22) and CrT$^{-/y}$ mice (n = 24). (A) Decreased power of 8-12 Hz alpha frequency and increased power of 13-30 Hz beta and 30-45 Hz gamma frequency in CrT$^{-/y}$ mice during the active wakefulness of light phase. (B) Decreased power of 4-8 Hz theta and increased power of 13-30 Hz beta frequency in CrT$^{-/y}$ mice during the passive wakefulness of light phase. (C) Decreased power of 4-8 Hz theta frequency, and increased power of 13-30 Hz beta and 30-45 Hz gamma frequency in CrT$^{-/y}$ mice during sleep in the light phase. (D) Decreased power of 8-12 Hz alpha frequency and increased power of 13-30 Hz beta frequency in CrT$^{-/y}$ mice during the active wakefulness of dark phase. (E) Decreased power of 4-8 Hz theta and increased power of 13-30 Hz beta frequency in CrT$^{-/y}$ mice during the passive wakefulness of dark phase. (F) Decreased power 4-8 Hz theta frequency, and increased power of 13-30 Hz beta and 30-45 Hz gamma frequency in CrT$^{-/y}$ mice during sleep in the dark phase. Vigilance state was classified by video inspection. Multiple t tests with adjusted p-value: * $p < 0.05$, § $p < 0.001$. Error bars, SEM.

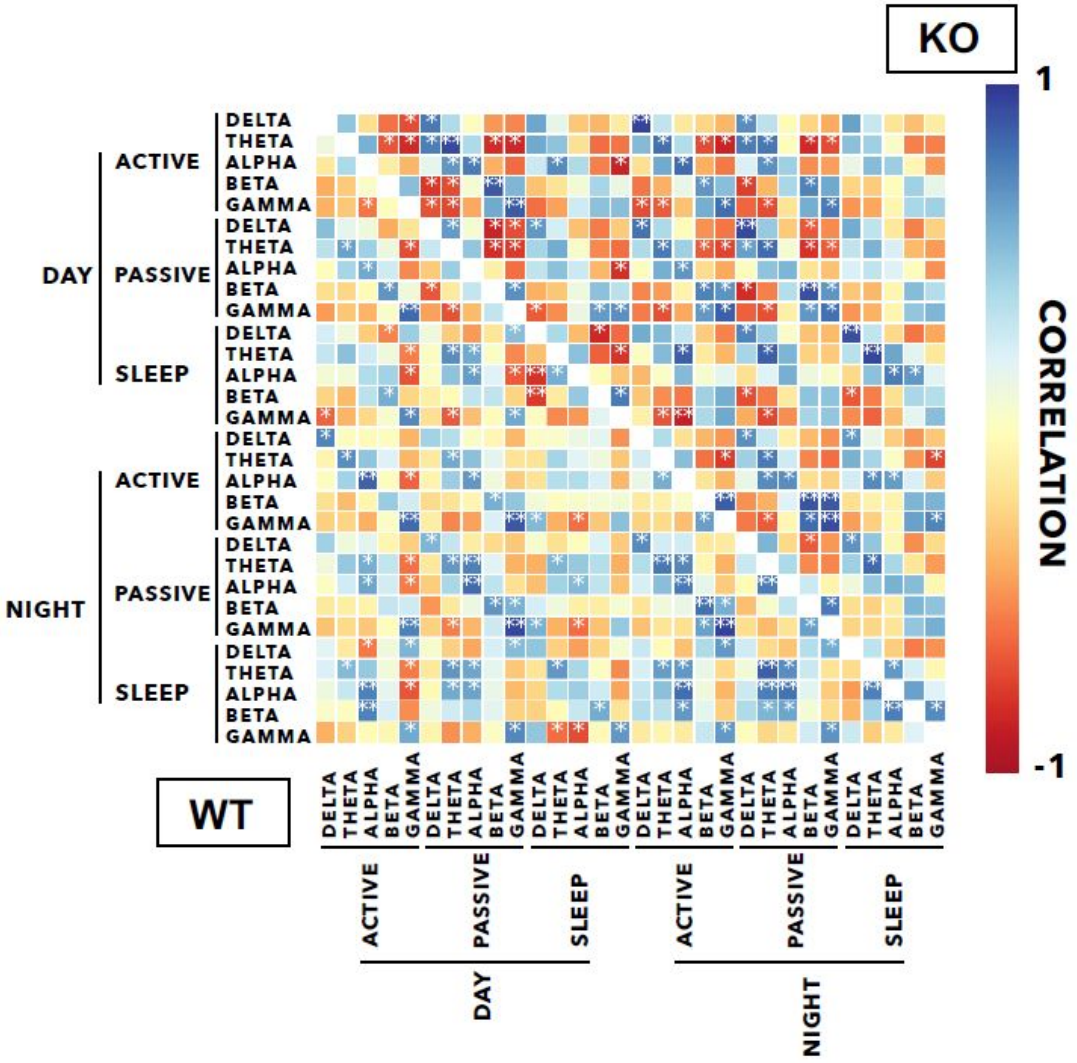


**Fig. 20. Correlation matrix showing the relationships between EEG power bands measured in three different behavioral states (active wake, passive wake and sleep) both during the day and the night phase in WT and CrT$^{-/y}$ animals.** The patch color indicates the correlation between the horizontal and vertical variables (Spearman's rho test). A single asterisk or a double asterisk in the colored patch indicates $p < 0.05$ and $p < 0.01$ (corrected using the Benjamini-Hochberg procedure), respectively. The bottom left panel contains the matrix for CrT$^{+/y}$ animals; the upper right panel contains the matrix for CrT$^{-/y}$ mice. The different correlation pattern suggests an altered synchronization of neural networks and anomalous functional connectivity in the brain of CrT$^{-/y}$ animals. It is worth noting that only 41 correlations are in common between WT (out of 99) and CrT$^{-/y}$ (out of 107) mice. The distribution between positively and negatively correlated bands was significantly different between the two groups (Fisher's

exact test, $p < 0.05$), with $CrT^{-/y}$ animals showing a lower proportion of positive correlations and higher percentage of inverse correlations.

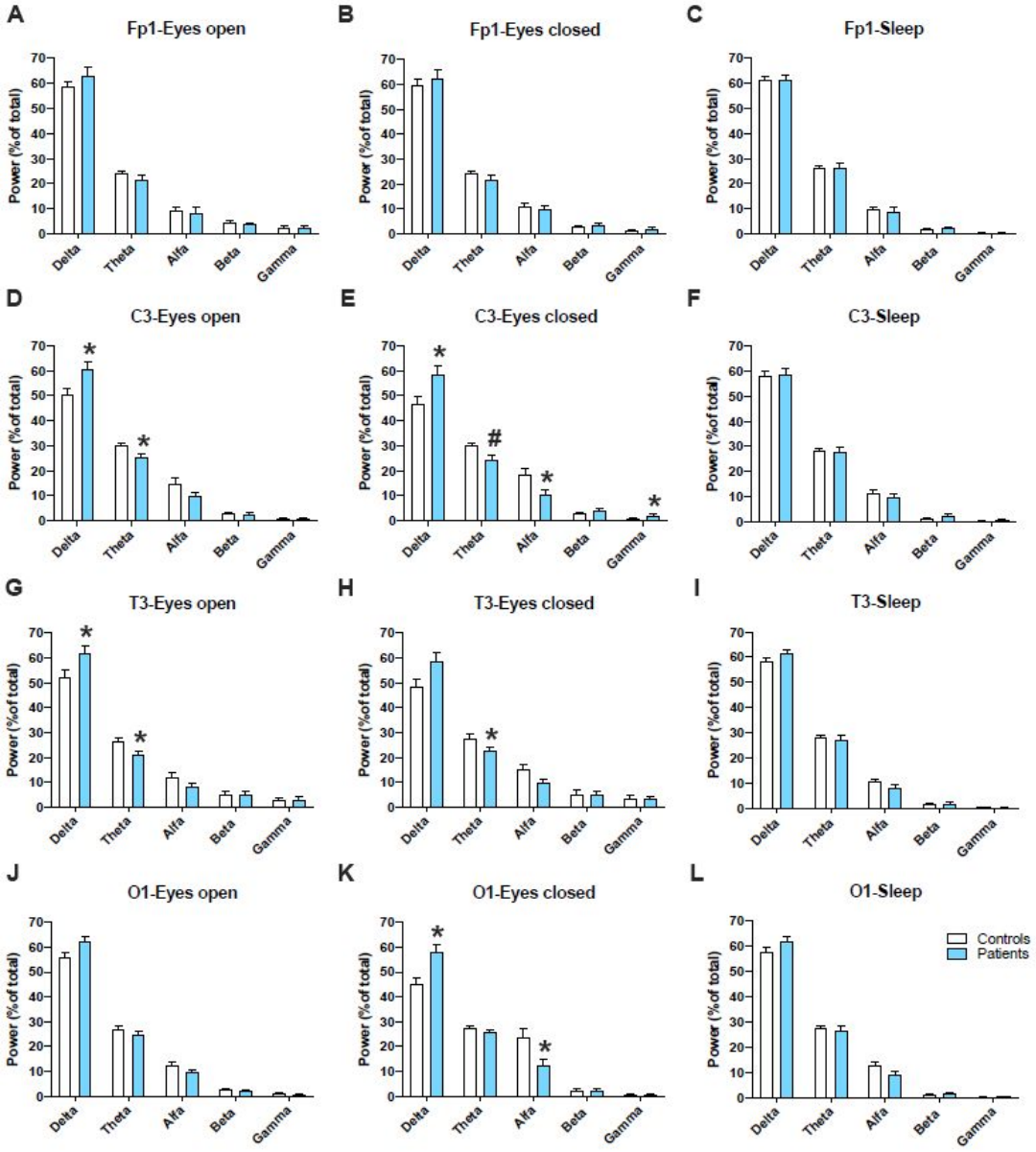


**Fig. 21. Altered neural oscillations in CTD patients in different behavioral states (eyes closed, eyes open and sleep).** Normalized power spectrum of cortical EEG recordings from CTD patients (n = 5) and age-matched controls (n = 12). Electrodes were placed following the international 10–20 convention. (A-C) No difference was found in the signal recorded from frontopolar (Fp1) electrode. (D-F) Increased power of 0.5-4 Hz delta frequency band and decreased power of 4-8 Hz theta frequency band in the signal recorded from central (C3) electrode in eyes open condition (D). Increased power of 0.5-4 Hz delta and 30-45 Hz gamma frequency band, and decreased power of 4-8 Hz theta and 8-12 Hz alpha frequency band in the signal recorded from C3 electrode in eyes closed condition (E). No difference in C3 electrode was found during sleep. (G-I) Increased

power of 0.5-4 Hz delta frequency band and decreased power of 4-8 Hz theta frequency band in the signal recorded from temporal (T3) electrode in eyes open and eyes closed condition (G, H). No difference in T3 electrode was found during sleep. (J-L) Increased power of 0.5-4 Hz delta frequency band and decreased power of 8-12 Hz alpha frequency band in the signal recorded from occipital (O1) electrode in eyes closed condition (K). No difference in O1 electrode was found in eyes open condition and during sleep (J, L). Multiple t tests: * $p < 0.05$. Error bars, SEM.

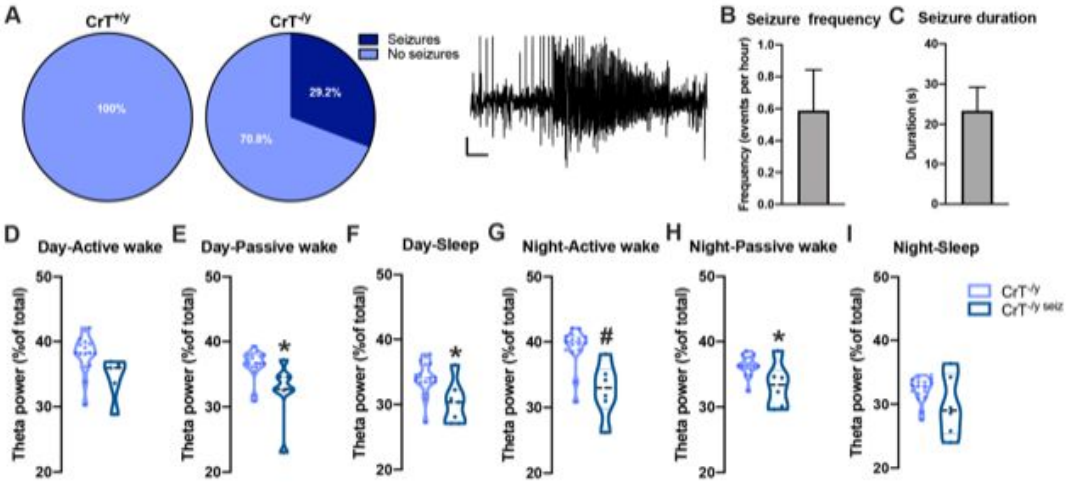


**Fig. 22: Spontaneous epileptic phenotype in CrT$^{-/y}$ animals and stratification of EEG power data according to this phenotype. (A)** Using baseline EEG recordings (24h), we found that 30% of CrT$^{-/y}$ mice (n = 24) display spontaneous seizures, while no ictal events were detected in CrT$^{+/y}$ animals (n = 22). On the right, a representative seizure in a CrT$^{-/y}$ mouse is shown. Calibration bar: 100 μV, 10s. **(B)** Frequency of spontaneous seizures in CrT$^{-/y}$ epileptic animals. **(C)** Average duration of spontaneous seizures in CrT$^{-/y}$ epileptic animals. **(D-I)** Violin plots with individual values depict normalized theta power spectrum of cortical EEG recordings from epileptic (Seizures, n = 7) and non-epileptic CrT$^{-/y}$ mice (No seizures, n = 17). Decreased power of 4-8 Hz theta frequency band in epileptic CrT$^{-/y}$ mice during the passive wakefulness and sleep in the light phase, and during the active and passive wakefulness in the dark phase. Multiple t-tests with adjusted p-value: * $p < 0.05$, # $p < 0.01$. Error bars, SEM.

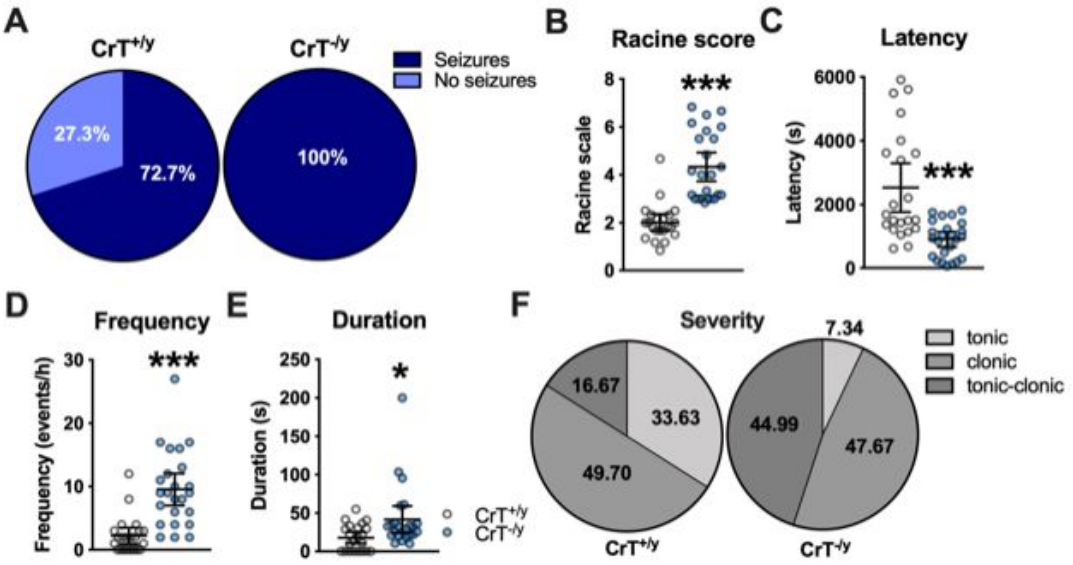


**Fig. 23: Kainic acid (KA) challenge in the brain of CrT$^{-/y}$ mice. (A)** Kainic acid injection (10 mg/kg) induced overt seizures in 100% of CrT$^{-/y}$ mice (n = 24), whereas only 14/22 WT animals displayed epileptic bursts at electrographical level over 1h of observation. **(B)** Effect of KA treatment at the behavioural level. Circles represent the maximum seizure rating score of individual WT and CrT$^{-/y}$ mice over a period of 1 hr after KA administration. Black lines represent mean with 95% CI. CrT$^{-/y}$ mice displayed a higher Racine score (t-test, $p < 0.001$). **(C-F)** Severity of KA-induced seizures in WT and CrT$^{-/y}$ mice at electrophysiological level. EEG analysis was performed on the same animals used for behavioural scoring. CrT$^{-/y}$ mice showed a lower latency to the first seizure (C, t-test, $p < 0.001$), and increased frequency (D, t-test, $p < 0.001$) and duration E, t-test, $p < 0.05$) of seizure events with respect to age-matched littermates. For WT animals not presenting seizures during the 1h of monitoring, we extended the observation until the occurrence of the first electrographical burst to provide a latency value. Circles represent single data values; black lines indicate mean with 95% CI. Relative percentage of tonic, clonic and tonic-clonic seizures WT and CrT$^{-/y}$ mice (F) indicates that seizure severity is more pronounced in CrT$^{-/y}$ animals ($\chi^2$ test; $p < 0.001$). * $p < 0.05$, *** $p < 0.001$.

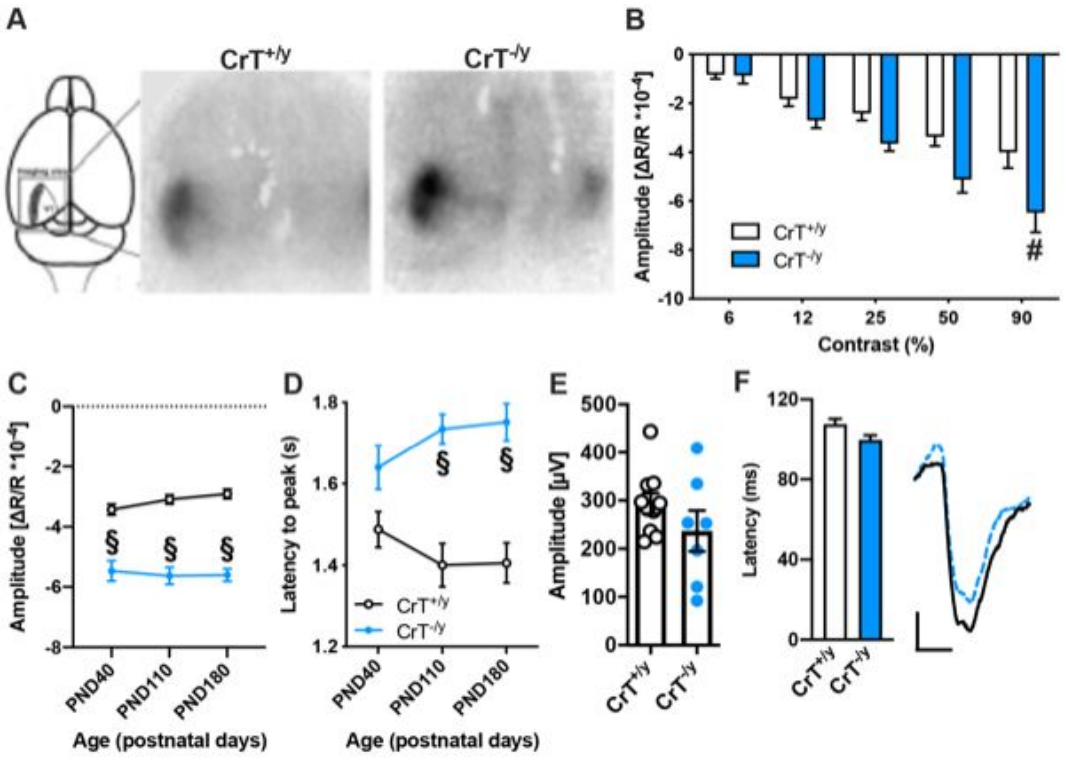


**Fig. 24. Altered hemodynamic response in CrT$^{-/y}$ animals. (A)** Typical IOS response to visual stimulation in the binocular visual field for a WT (CrT$^{+/y}$) and a CrT$^{-/y}$ animal. **(B)** Contrast-response function for contralateral eye stimulation in male WT (n = 6) and CrT$^{-/y}$ (n = 9) mice at PND40. IOS amplitude was increased in CrT$^{-/y}$ animals in particular at high contrast of visual stimuli (Two-way ANOVA, effect of genotype $p < 0.05$, genotype x contrast interaction $p < 0.05$, post- hoc Holm Sidak method, $p < 0.01$ at 90% of contrast). **(C)** Response for contralateral eye stimulation in male WT and CrT$^{-/y}$ mice at three different time points (n = 15 for each group at each time point). IOS amplitude was significantly increased in CrT$^{-/y}$ animals (Two-way ANOVA, effect of genotype $p < 0.001$, post-hoc Holm Sidak method $p < 0.001$ at all ages tested). **(D)** The latency of IOS responses was longer in CrT$^{-/y}$ mice at PND110 and PND180 (Two-way ANOVA, effect of genotype $p < 0.001$, post-hoc Holm Sidak method $p < 0.001$). **(E-F)** No differences in VEP amplitude (E) and latency (F) were detected between WT (n = 10) and CrT$^{-/y}$ animals (n = 7; t-test, $p = 0.767$ and $p = 0.087$, respectively). Representative VEP traces for a WT (continuous black line) and a CrT$^{-/y}$ (dashed blue line) mouse are also shown on the right. # $p < 0.01$, § $p < 0.001$. Error bars, SEM.

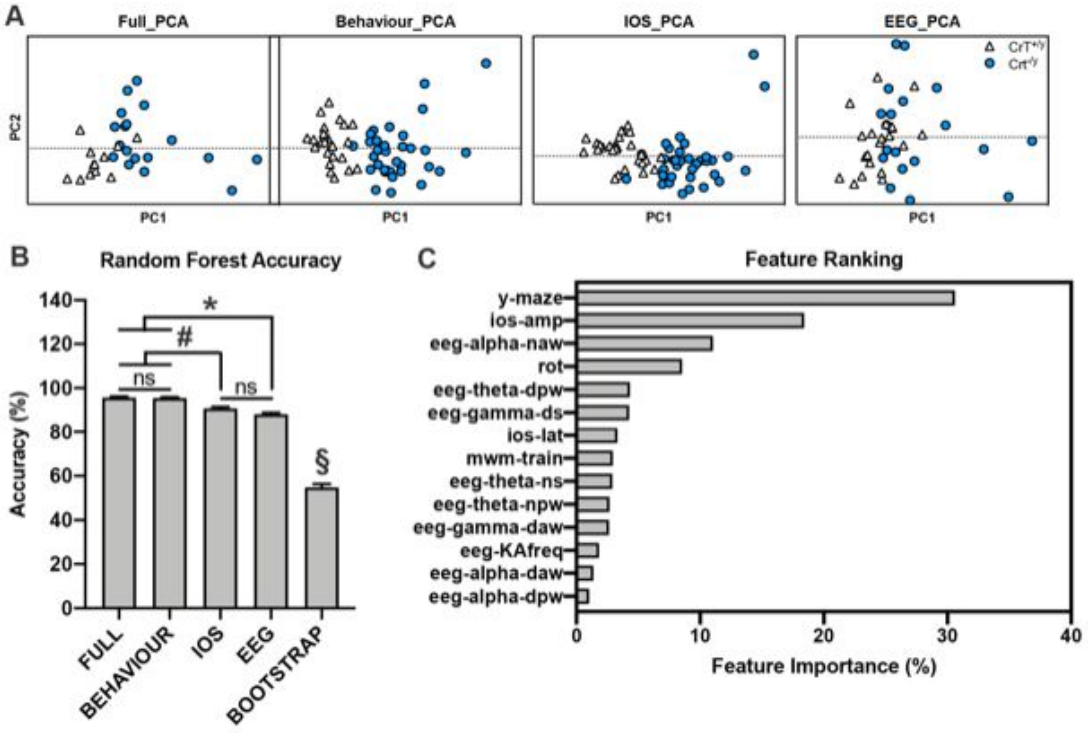


**Fig. 25. Random Forest analysis of the dataset. (A)** Scatter plot of all the experimental subjects analyzed with the full dataset (Full), behavioral (Behavior), IOS imaging (IOS) and EEG variables plotted in the space of the first two principal components of PCA. **(B)** Comparison of accuracy for different Random Forest classifiers trained and tested, respectively, with the entire dataset, behavioral, IOS, EEG variables and randomly permuted dataset (Bootstrap). A Kruskal-Wallis analysis followed by Dunn's multiple comparisons revealed that the behavioral variable has an accuracy comparable to the full dataset, whereas the accuracy of IOS and EEG variables is slightly lower. All classifiers displayed a higher accuracy than Bootstrap ($p < 0.001$ for all comparisons). **(C)** Histogram depicts the relative importance of top 14 features in the Random Forest model. The following abbreviations were used: ios-amp, amplitude of IOS signal; naw, night active wake; rot, rotarod; dpw, day passive wake; ds, day sleep; ios-lat, latency of IOS signal; mwm-train, training distance of Morris water maze; ns, night sleep; npw, night passive wake; daw, day active wake; KAfreq, frequency of seizures after KA challenge. * $p < 0.05$, # $p < 0.01$, § $p < 0.001$, ns, not significant. Error bars, SEM.

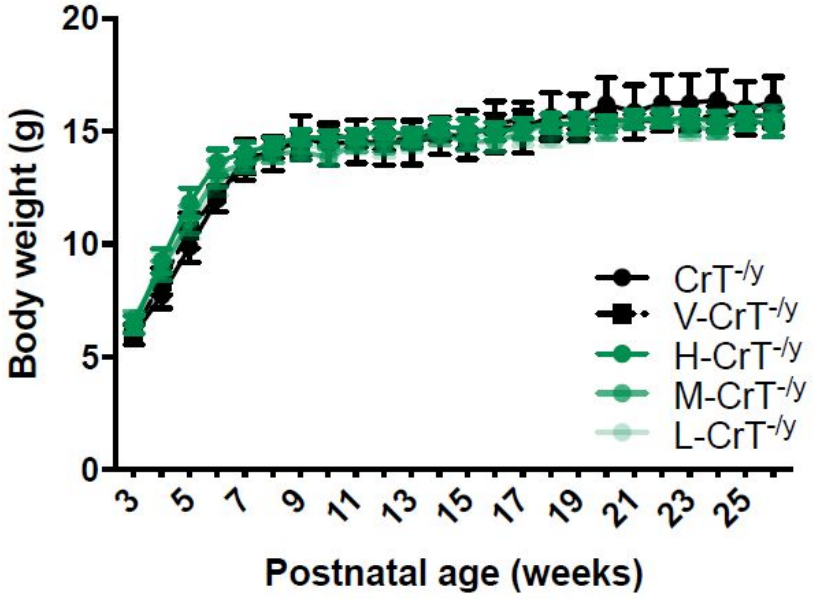


**Fig. 26. No effect of cCr treatment on body weight.** The weight of $CrT^{-/y}$ mice treated with the different doses of cCr (H-$CrT^{-/y}$, n = 19; M-$CrT^{-/y}$, n = 17; L-$CrT^{-/y}$, n = 16) was comparable to that of untreated (n = 18) and vehicle-treated $CrT^{-/y}$ animals (n = 16) at any age tested (mixed effects analysis, effect of treatment p = 0.989). Error bars, SEM.

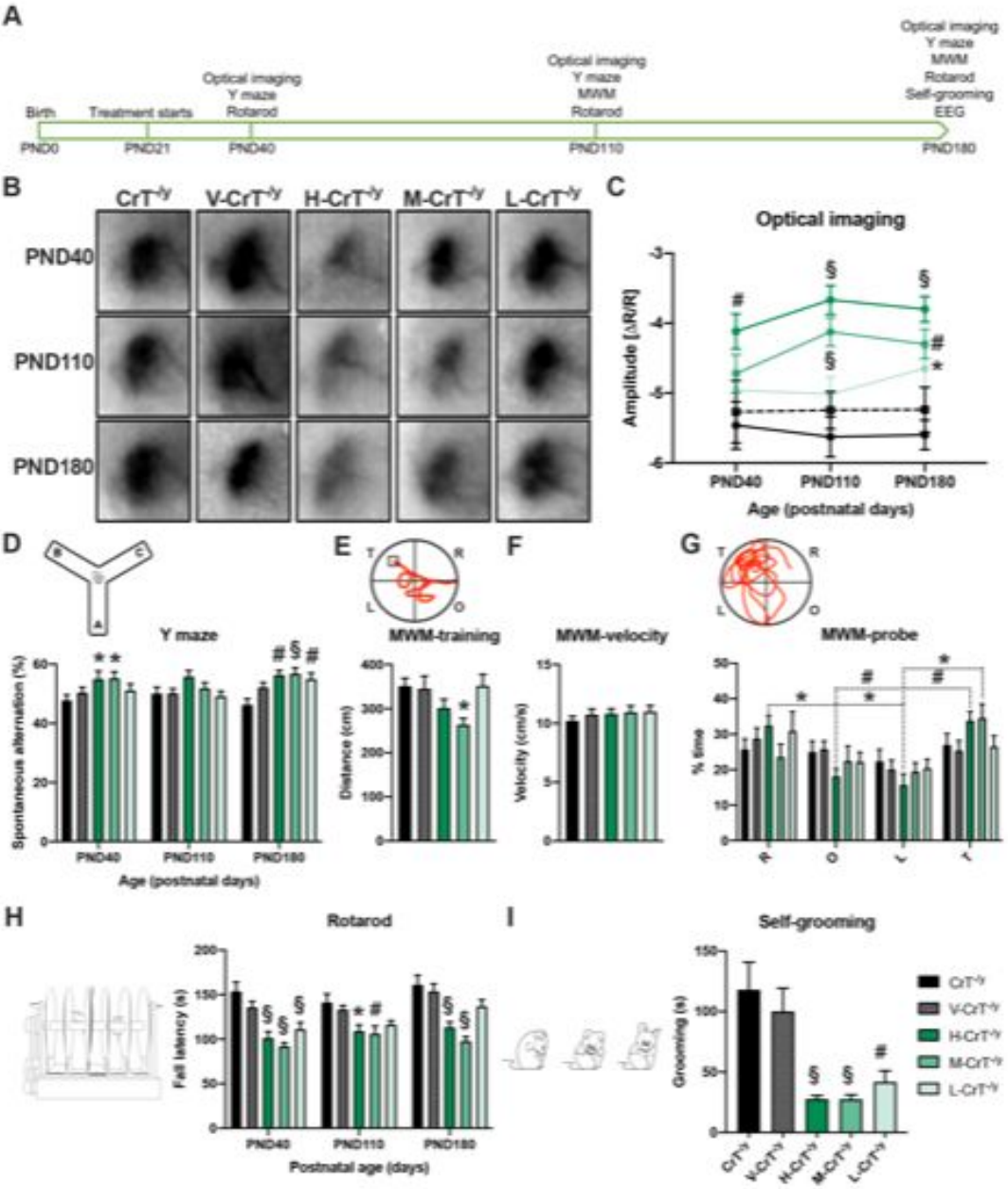


**Fig. 27. cCr treatment improves hemodynamic responses and behavior in CrT$^{-/y}$ mice. (A)** Schematic diagram of the experimental design. We employed IOS imaging, behavioral assessment (Y maze and Morris water maze, MWM) and video-EEG recordings to evaluate the therapeutic efficacy of longitudinal treatment with cCr at three different doses (high dose, H: 140 mg/kg, medium dose, M: 46 mg/kg, low dose, L: 14 mg/kg). Untreated mice (CrT$^{-/y}$) and animals administered with placebo (only chocolate milk, V-CrT$^{-/y}$) were used as controls (n = 15 for each group at each time point, except n = 17 each for H-CrT$^{-/y}$ and M-CrT$^{-/y}$ mice at PND180). **(B)** Representative IOS response images collected at different ages (PND40, PND110 and PND180) in CrT$^{-/y}$, V-CrT$^{-/y}$,

H-CrT$^{-/y}$, M-CrT$^{-/y}$ and L-CrT$^{-/y}$ mice. **(C)** Mean amplitude of visually evoked IOS responses measured after 20 (PND40), 90 (PND110) and 160 (PND180) days of cCr delivery. Two-way ANOVA revealed a significant effect of treatment ($p < 0.001$) and post-hoc Dunnett's multiple comparisons test showed an amelioration of hemodynamic responses in H-CrT$^{-/y}$ mice at every time point tested ($p < 0.01$ at PND40, $p < 0.001$ at PND110 and PND180), whereas IOS signals were attenuated at PND110 ($p < 0.001$) and PND180 ($p < 0.01$) in M-CrT$^{-/y}$ animals, and only at PND180 ($p < 0.05$) in L-CrT$^{-/y}$ mice. No difference was present between untreated CrT$^{-/y}$ animals and V-CrT$^{-/y}$ mice ($p = 0.965$ at PND40, $p = 0.728$ at PND110, $p = 0.739$ at PND180). **(D)** Histograms depict the spontaneous alteration rate in the Y maze for the different experimental groups at PND40, PND110 and PND180. The performance of H-CrT$^{-/y}$ and M-CrT$^{-/y}$ animals was statistically higher than CrT$^{-/y}$ littermates at PND40 (Two-way ANOVA, effect of treatment $p < 0.001$, post-hoc Dunnett's multiple comparisons test, $p < 0.05$) and PND180 ($p < 0.01$ for H-CrT$^{-/y}$ group, $p < 0.001$ for M-CrT$^{-/y}$ mice); L-CrT$^{-/y}$ showed a slightly improved spontaneous alternation only at PND180 ($p < 0.01$). No difference emerged between CrT$^{-/y}$ animals and V-CrT$^{-/y}$ mice at every age tested ($p = 0.767$ at PND40, $p = 0.999$ at PND110, $p = 0.112$ at PND180). The inset depicts a schematic diagram of the Y maze apparatus. **(E-G)** MWM at PND180. The mean swimming path covered prior to locate the submerged platform on the last three days of training (E) was statistically shorter in M-CrT$^{-/y}$ mice (One-way ANOVA, $p < 0.05$, post-hoc Dunnett's multiple comparisons test, $p < 0.05$). The inset shows a representative example of swimming path during the training phase. Mean swimming speed (F) was unaffected by cCr treatment (One-way ANOVA, $p = 0.774$). (G) Probe trial. A Two-Way RM ANOVA followed by Dunnett's multiple comparisons revealed that while CrT$^{-/y}$ animals did not show any exploration preference, H-CrT$^{-/y}$ mice spent significantly more time in the T quadrant than in the opposite (O, $p < 0.01$) and in the left (L, $p < 0.01$) quadrants. No difference was present between the time in the T and the right (R) quadrant ($p = 0.968$). M-CrT$^{-/y}$ mice spent significantly more time in the T quadrant than in the L quadrant ($p < 0.01$). No effect of the low cCr dose or vehicle treatment was detected. The inset shows a representative example of swimming path during the probe phase. **(H)** A Two-way ANOVA highlighted a significant effect of treatment ($p < 0.001$) in the performance of CrT$^{-/y}$ animals on the accelerating rotarod. Post hoc Dunnett's multiple

comparison test showed that the fall latency of H-CrT$^{-/y}$, M-CrT$^{-/y}$ and L-CrT$^{-/y}$ mice was significantly lower from that of CrT$^{-/y}$ animals at PND40 ($p < 0.001$ for all groups), whereas only H-CrT$^{-/y}$ and M-CrT$^{-/y}$ mice exhibited an improved performance at PND110 ($p < 0.05$ for H-CrT$^{-/y}$ and $p < 0.01$ for M-CrT$^{-/y}$) and PND180 ($p < 0.001$ for both groups). No difference was present between CrT$^{-/y}$ animals and V-CrT$^{-/y}$ mice ($p = 0.293$ at PND40, $p = 0.876$ at PND110, $p = 0.888$ at PND180). Inset shows an illustration of the rotarod apparatus. **(K)** H-CrT$^{-/y}$, M-CrT$^{-/y}$ and L-CrT$^{-/y}$ mice showed decreased self-grooming behavior at PND180 (One-way ANOVA, effect of treatment $p < 0.001$, post-hoc Dunnett's multiple comparisons test, $p < 0.001$ for H-CrT$^{-/y}$ and M-CrT$^{-/y}$ animals, $p < 0.01$ for L-CrT$^{-/y}$ mice). No effect of vehicle treatment was detected ($p = 0.793$). A schematic representation of self-grooming behavior is also shown. * $p < 0.05$, # $p < 0.01$, § $p < 0.001$. Error bars, SEM.

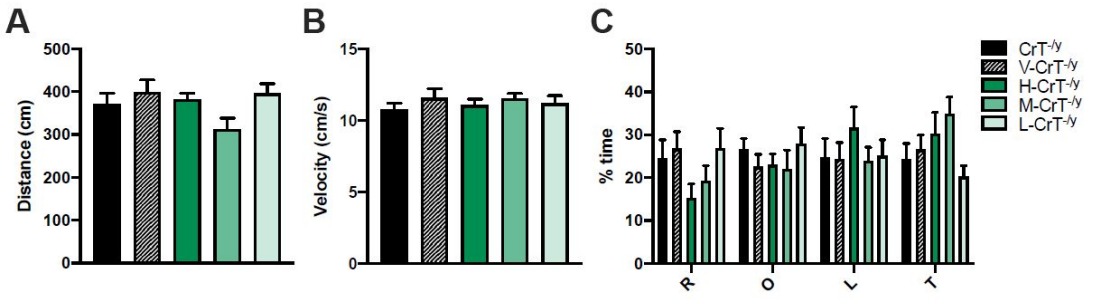


**Fig. 28. Spatial learning and memory at PND110.** (A) No effect of cCr was found in the average distance covered to locate the platform in the last three days of training (One-way ANOVA, p = 0.09) and (B) in swimming velocity of mice (p = 0.469). (C) The probe test shows lack of preferential exploration of the target (T) quadrant where the platform was located during the training phase for all experimental groups (Two-way RM ANOVA, effect of treatment p = 0.718, interaction treatment x quadrant p = 0.182). R, right; O, opposite; L, left. Error bars, SEM.

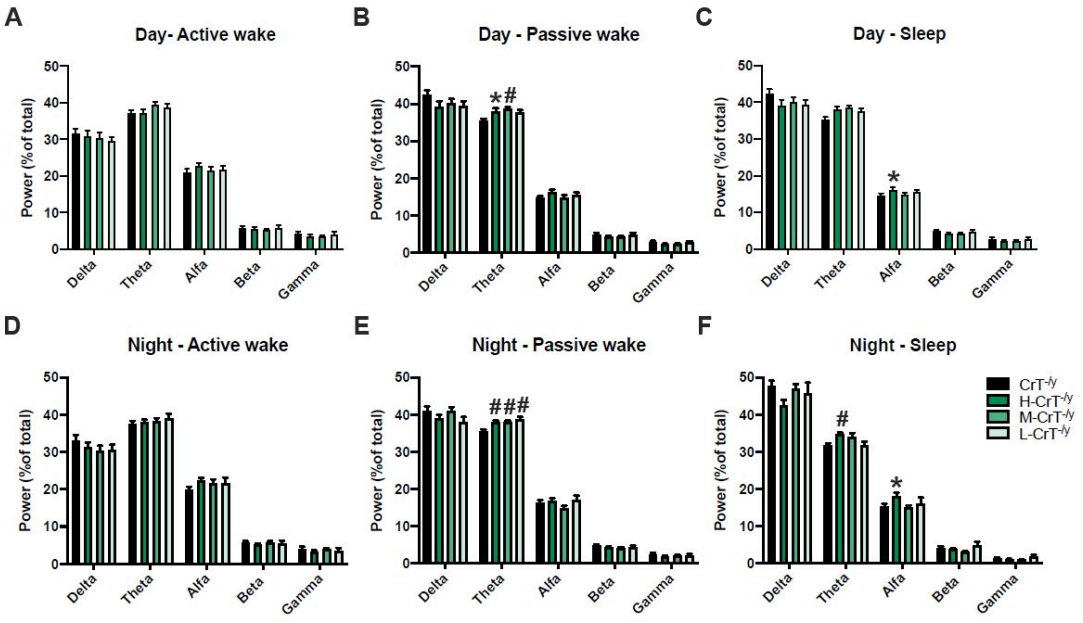


**Fig. 29. Rescue of theta brain oscillations following cCr treatment.** (A-F) Normalized power spectrum of cortical EEG recordings from $CrT^{-/y}$ (n = 24), H-$CrT^{-/y}$ (n = 15), M-$CrT^{-/y}$ (n = 12) and L-$CrT^{-/y}$ mice (n = 8). Untreated and V-$CrT^{-/y}$ mice were pooled together in the $CrT^{-/y}$ group. Increased power of 4-8 Hz theta frequency in H-$CrT^{-/y}$ and M-$CrT^{-/y}$ animals during the passive wakefulness (One-way ANOVA, $p < 0.01$, post-hoc Dunnett's multiple comparisons test, $p < 0.05$ for H-$CrT^{-/y}$ and $p < 0.01$ for M-$CrT^{-/y}$), and increased power of 8-12 Hz alpha frequency in H-$CrT^{-/y}$ mice ($p < 0.05$) during sleep of light phase. Increased power of 4-8 Hz theta frequency in H-$CrT^{-/y}$, M-$CrT^{-/y}$ and L-$CrT^{-/y}$ animals during the passive wakefulness ($p < 0.01$ for all comparisons), and increased power of 4-8 Hz theta ($p < 0.01$) and 8-12 Hz alpha frequency ($p < 0.05$) in H-$CrT^{-/y}$ mice during sleep of night phase. Vigilance state was classified by video inspection. * $p < 0.05$, # $p < 0.01$. Error bars, SEM.

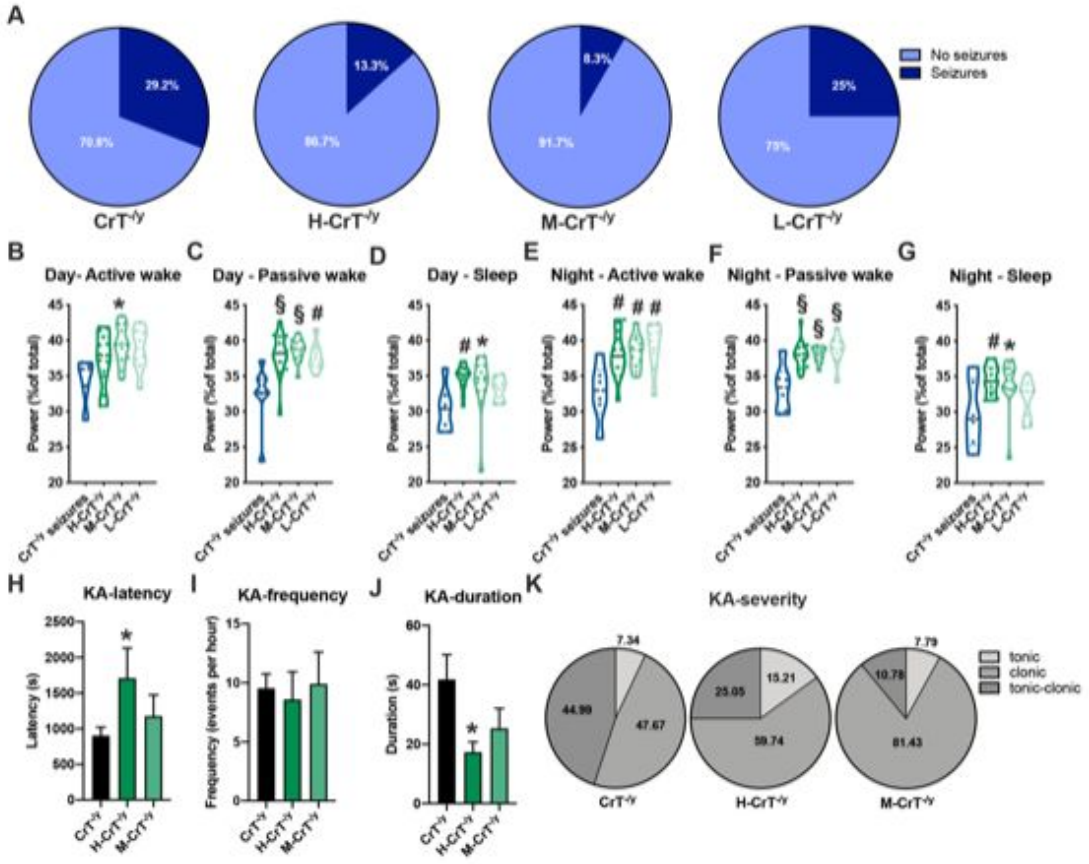


**Fig. 30. cCr treatment protects CrT$^{-/y}$ mice against spontaneous and evoked epilepsy. (A)** The percentage of animals experiencing spontaneous seizures at the clinical and electrographical level was significantly lower in H-CrT$^{-/y}$ (Fisher's exact test, $p < 0.01$) and M-CrT$^{-/y}$ mice ($p < 0.001$) than in CrT$^{-/y}$ group. No beneficial effect was detected in L-CrT$^{-/y}$ animals ($p = 0.431$). **(B-G)** The comparison of power spectra of cortical EEG recordings with epileptic CrT$^{-/y}$ mice (CrT$^{-/y}$ -seizures, n = 7) revealed an increased power of 4-8 Hz theta frequency in cCr-treated animals (One-way ANOVA, post-hoc Dunnett's multiple comparisons test). **(H-K)** Effect of KA treatment in CrT$^{-/y}$, H-CrT$^{-/y}$ and M-CrT$^{-/}$ mice at behavioral and electrophysiological level. While no difference was present in the frequency of ictal events (I, One-way ANOVA, $p = 0.897$), H-CrT$^{-/y}$ mice displayed a longer latency (H, One-way ANOVA, effect of treatment $p < 0.05$, post-hoc Dunnett's multiple comparisons test, $p < 0.05$) and a shorter duration (J, One-way ANOVA, effect of treatment $p < 0.05$, post-hoc Dunnett's multiple comparisons test, $p < 0.05$) of epileptiform bursts compared to CrT$^{-/y}$ animals. (K) Relative percentage of tonic, clonic and tonic-clonic seizures indicates that seizure severity is less pronounced in

H-CrT$^{-/y}$ and M-CrT$^{-/y}$ animals at 10 mg/kg ($\chi^2$ test; $p < 0.001$). * $p < 0.05$, # $p < 0.01$, § $p < 0.001$. Error bars, SEM.

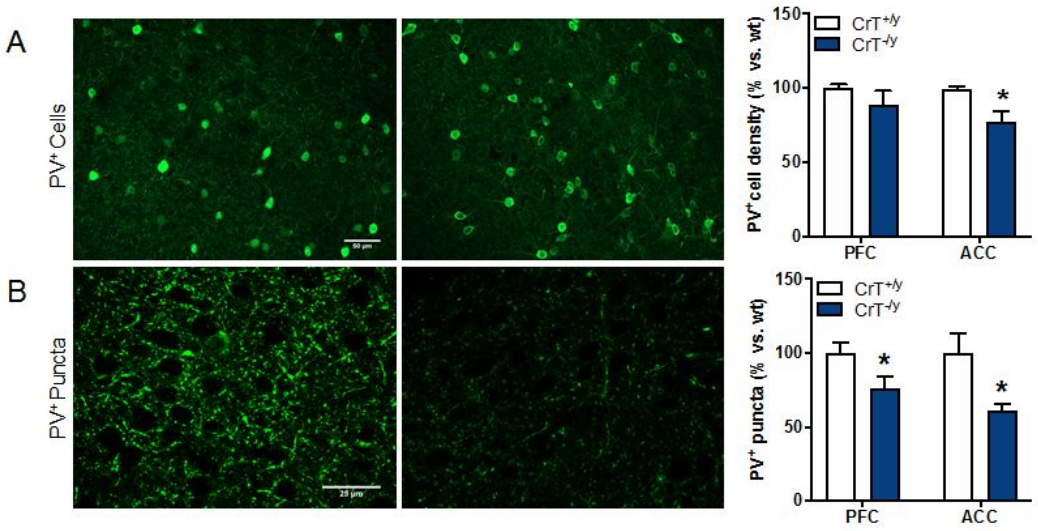


**Fig. 31. Cortical parvalbuminergic interneurons alterations in CrT$^{-/y}$ mice.** (A) PV$^{+}$ interneurons density is not altered in PFC of CrT$^{-/y}$ mice (unpaired t-test, $p = 0.28$) but is lower in ACC (unpaired t-test, $p < 0.05$). (B) Cortical PV$^{+}$ puncta density is lower both in PFC and in ACC of CrT$^{-/y}$ mice (PFC, unpaired t-test, $p < 0.05$; ACC, unpaired t-test, $p < 0.05$). N = 5 for all groups in every experiments. Representative immunostaining images for PV$^{+}$ cells are shown in top left and middle panel. Representative immunostaining images for PV$^{+}$ puncta are shown in bottom left and middle panel.

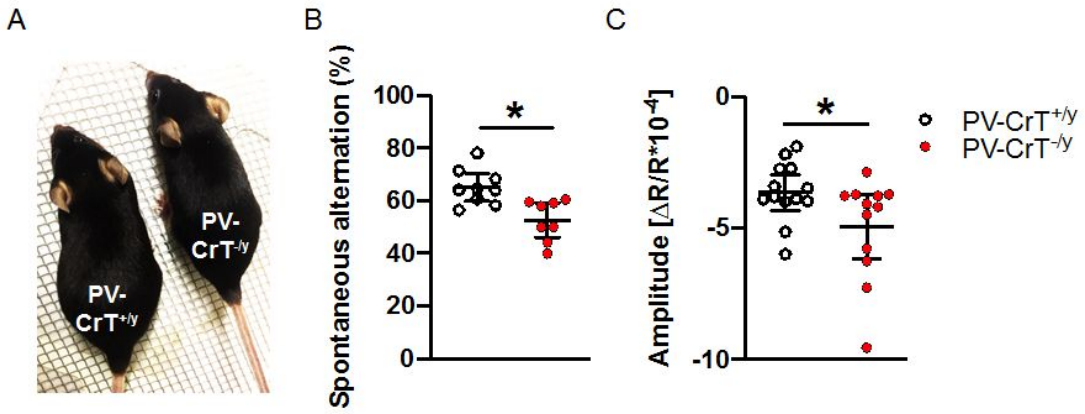


**Fig. 32. CrT$^{-/y}$ biomarkers analysis in PV-CrT$^{-/y}$ reveals common features.** (A) Representative image of PV-CrT$^{+/y}$ and PV-CrT$^{-/y}$ mice. (B) Spontaneous alternation rate is decreased in PV-CrT$^{-/y}$ mice (unpaired t-test, $p < 0.05$). (C) IOS response amplitude is higher in PV-CrT$^{-/y}$ mice (unpaired t-test, $p < 0.05$).

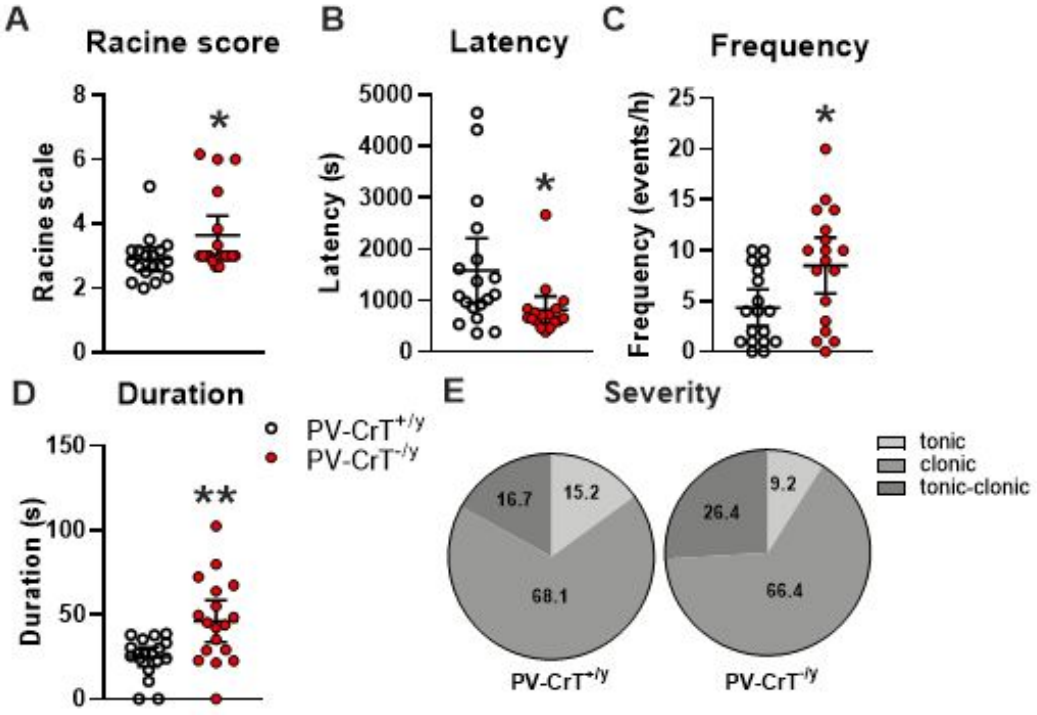


**Fig. 33. Epileptic phenotipe of PV-CrT$^{-/y}$ mice.** PV-CrT$^{-/y}$ mice show a higher susceptibility to KA challenge proved by (A) the increased severity of convulsions scored at behavioural level (Mann-Whitney, $p < 0.05$), (B) shorter latency to first seizure (Mann-Whitney, $p < 0.05$), (C) increased frequency (Mann-Whitney, $p < 0.05$) and (D) duration of epileptic episodes (Mann-Whitney, $p < 0.01$), and a major occurrence of tonic-clonic seizures (E).

# 6. TABLES

| Tissue (nmol/ mg protein) | P30 | | P180 | |
|---|---|---|---|---|
| | $CrT^{+/y}$ | $CrT^{-/y}$ | $CrT^{+/y}$ | $CrT^{-/y}$ |
| Cortex | 76.36 ± 3.16 | 13.61 ± 1.06*** | 92.41 ± 0.66 | 14.15 ± 0.66*** |
| Hippocampus | 83.69 ± 4.37 | 14.14 ± 1.52*** | 88.73 ± 4.97 | 14.79 ± 1.46*** |
| Muscle | 310.20 ± 31.59 | 111.57 ± 21.27*** | 365.38 ± 8.19 | 15.94 ± 5.55*** |
| Heart | 89.92 ± 5.15 | 1.19 ± 0.27*** | 100.91 ± 3.36 | 2.39 ± 0.61*** |
| Kidney | 9.60 ± 0.65 | 1.59 ± 0.13* | 10.36 ± 0.80 | 1.80 ± 0.78** |

**Table 1**: Cr levels (mean ± s.e.m.) in $CrT^{+/y}$ and $CrT^{-/y}$ animals at P30 and P180 (n = 4 per tissue for both groups). Cr levels have been measured by GC/MS. A reduction of Cr content was evident in the brain, muscle, heart and kidney of mutant animals at both P30 and P180 (Two-Way ANOVA on rank transformed data, post hoc Holm-Sidak method). *$p < 0.05$; **$p < 0.01$; ***$p < 0.001$

| Tissue (nmol/ mg protein) | P30 | | P180 | |
|---|---|---|---|---|
| | $CrT^{+/y}$ | $CrT^{-/y}$ | $CrT^{+/y}$ | $CrT^{-/y}$ |
| Cortex | 0.060 ± 0.002 | 0.114 ± 0.016*** | 0.050 ± 0.006 | 0.066 ± 0.005 |
| Hippocampus | 0 | 0.091 ± 0.007 *** | 0.026 ± 0.015 | 0.079 ± 0.009** |
| Muscle | 0.106 ± 0.006 | 0.282 ± 0.068** | 0.026 ± 0.010 | 0.150 ± 0.050** |
| Heart | 0.094 ± 0.010 | 0.060 ± 0.004*** | 0.052 ± 0.007 | 0.033 ± 0.015 |
| Kidney | 10.700 ± 0.627 | 9.758 ± 0.712 | 2.205 ± 0.259 | 2. 411 ± 0.112 |

**Table 2**: GAA levels (mean ± s.e.m.) in $CrT^{+/y}$ and $CrT^{-/y}$ animals at P30 and P180 (n = 4 per tissue for both groups). At P30, a moderate increase of GAA content was evident in the brain and the muscle of mutant animals (Two-Way ANOVA on rank transformed data, post hoc Holm-Sidak method, $p < 0.05$), whereas GAA was decreased in the heart of $CrT^{-/y}$ animals ($p < 0.05$) and no difference was detected in the kidney tissue ($p = 0.359$). At P180, GAA levels were higher in the hippocampus and the muscle of mutant animals (Two-Way ANOVA on rank transformed data, post hoc Holm-Sidak method, $p < 0.01$), whereas no difference was detected in cortex, heart and kidney ($p = 0.175$, $p = 0.320$ and $p = 0.920$, respectively). **$p < 0.01$; ***$p < 0.001$.

# 7. BIBLIOGRAPHY


1. Wyss, M. & Kaddurah-Daouk, R. Creatine and creatinine metabolism. *Physiol. Rev.* **80**, 1107–1213 (2000).
2. Andres, R. H., Ducray, A. D., Schlattner, U., Wallimann, T. & Widmer, H. R. Functions and effects of creatine in the central nervous system. *Brain Res. Bull.* **76**, 329–343 (2008).
3. Almeida, L. S., Salomons, G. S., Hogenboom, F., Jakobs, C. & Schoffelmeer, A. N. M. Exocytotic release of creatine in rat brain. *Synapse* **60**, 118–123 (2006).
4. Brosnan, J. T. & Brosnan, M. E. Creatine: endogenous metabolite, dietary, and therapeutic supplement. *Annu. Rev. Nutr.* **27**, 241–261 (2007).
5. Snow, R. J. & Murphy, R. M. Creatine and the creatine transporter: a review. *Mol. Cell. Biochem.* **224**, 169–181 (2001).
6. Guimbal, C. & Kilimann, M. W. A Na(+)-dependent creatine transporter in rabbit brain, muscle, heart, and kidney. cDNA cloning and functional expression. *J. Biol. Chem.* **268**, 8418–8421 (1993).
7. Iyer, G. S. *et al.* Identification of a testis-expressed creatine transporter gene at 16p11.2 and confirmation of the X-linked locus to Xq28. *Genomics* **34**, 143–146 (1996).
8. Braissant, O. & Henry, H. AGAT, GAMT and SLC6A8 distribution in the central nervous system, in relation to creatine deficiency syndromes: a review. *J. Inherit. Metab. Dis.* **31**, 230–239 (2008).
9. Saunders, A. *et al.* Molecular Diversity and Specializations among the Cells of the Adult Mouse Brain. *Cell* **174**, 1015–1030.e16 (2018).

10. Braissant, O. *et al.* 10.1186/1471-213X-5-9. *BMC Dev Biol* vol. 5 9 (2005).

11. Carducci, C. *et al.* In vitro study of uptake and synthesis of creatine and its precursors by cerebellar granule cells and astrocytes suggests some hypotheses on the physiopathology of the inherited disorders of creatine metabolism. *BMC Neurosci.* **13**, 41 (2012).

12. Dodd, J. R., Birch, N. P., Waldvogel, H. J. & Christie, D. L. Functional and immunocytochemical characterization of the creatine transporter in rat hippocampal neurons. *J. Neurochem.* **115**, 684–693 (2010).

13. Peral, M. J., Vázquez-Carretero, M. D. & Ilundain, A. A. Na(+)/Cl(-)/creatine transporter activity and expression in rat brain synaptosomes. *Neuroscience* **165**, 53–60 (2010).

14. Joncquel-Chevalier Curt, M. *et al.* Creatine biosynthesis and transport in health and disease. *Biochimie* **119**, 146–165 (2015).

15. Braissant, O., Henry, H., Loup, M., Eilers, B. & Bachmann, C. Endogenous synthesis and transport of creatine in the rat brain: an in situ hybridization study. *Molecular Brain Research* vol. 86 193–201 (2001).

16. Braissant, O. *et al.* Ammonium-Induced Impairment of Axonal Growth Is Prevented through Glial Creatine. *The Journal of Neuroscience* vol. 22 9810–9820 (2002).

17. Holtzman, D. *et al.* Brain creatine phosphate and creatine kinase in mice fed an analogue of creatine. *Brain Res.* **483**, 68–77 (1989).

18. Braissant, O. Creatine and guanidinoacetate transport at blood-brain and blood-cerebrospinal fluid barriers. *Journal of Inherited Metabolic Disease* vol. 35 655–664 (2012).

19. Braissant, O. *et al.* Ammonium alters creatine transport and synthesis in a 3D culture of developing brain cells, resulting in secondary cerebral creatine deficiency. *European Journal of Neuroscience* vol. 27 1673–1685 (2008).

20. Ohtsuki, S. *et al.* The Blood–Brain Barrier Creatine Transporter is a Major Pathway for Supplying Creatine to the Brain. *Journal of Cerebral Blood Flow & Metabolism* vol. 22 1327–1335 (2002).

21. Tachikawa, M., Fukaya, M., Terasaki, T., Ohtsuki, S. & Watanabe, M. Distinct cellular expressions of creatine synthetic enzyme GAMT and creatine kinases uCK-Mi and CK-B suggest a novel neuron-glial relationship for brain energy homeostasis. *European Journal of Neuroscience* vol. 20 144–160 (2004).

22. Braissant, O. Ammonia toxicity to the brain: Effects on creatine metabolism and transport and protective roles of creatine. *Molecular Genetics and Metabolism* vol. 100 S53–S58 (2010).

23. Loike, J. D., Zalutsky, D. L., Kaback, E., Miranda, A. F. & Silverstein, S. C. Extracellular creatine regulates creatine transport in rat and human muscle cells. *Proc. Natl. Acad. Sci. U. S. A.* **85**, 807–811 (1988).

24. Li, H. *et al.* Regulation of the creatine transporter by AMP-activated protein kinase in kidney epithelial cells. *Am. J. Physiol. Renal Physiol.* **299**, F167–77 (2010).

25. Strutz-Seebohm, N. *et al.* PIKfyve in the SGK1 mediated regulation of the creatine transporter SLC6A8. *Cell. Physiol. Biochem.* **20**, 729–734 (2007).

26. Stöckler, S. *et al.* Creatine deficiency in the brain: a new, treatable inborn error of metabolism. *Pediatr. Res.* **36**, 409–413 (1994).

27. van de Kamp, J. M., Mancini, G. M. & Salomons, G. S. X-linked creatine transporter deficiency: clinical aspects and pathophysiology. *J. Inherit. Metab. Dis.* **37**, 715–733

(2014).

28. Item, C. B. *et al.* Arginine:glycine amidinotransferase deficiency: the third inborn error of creatine metabolism in humans. *Am. J. Hum. Genet.* **69**, 1127–1133 (2001).
29. Clark, J. F. & Cecil, K. M. Diagnostic methods and recommendations for the cerebral creatine deficiency syndromes. *Pediatr. Res.* **77**, 398–405 (2015).
30. Betsalel, O. T. *et al.* Detection of low-level somatic and germline mosaicism by denaturing high-performance liquid chromatography in a EURO-MRX family with SLC6A8 deficiency. *neurogenetics* vol. 9 183–190 (2008).
31. Clark, A. J. *et al.* X-linked creatine transporter (SLC6A8) mutations in about 1% of males with mental retardation of unknown etiology. *Hum. Genet.* **119**, 604–610 (2006).
32. Mercimek-Mahmutoglu, S. *et al.* Screening for X-linked creatine transporter (SLC6A8) deficiency via simultaneous determination of urinary creatine to creatinine ratio by tandem mass-spectrometry. *Mol. Genet. Metab.* **96**, 273–275 (2009).
33. Newmeyer, A., Cecil, K. M., Schapiro, M., Clark, J. F. & Degrauw, T. J. Incidence of brain creatine transporter deficiency in males with developmental delay referred for brain magnetic resonance imaging. *J. Dev. Behav. Pediatr.* **26**, 276–282 (2005).
34. Puusepp, H. *et al.* The screening of SLC6A8 deficiency among Estonian families with X-linked mental retardation. *J. Inherit. Metab. Dis.* **33 Suppl 3**, S5–11 (2010).
35. Rosenberg, E. H. *et al.* High prevalence of SLC6A8 deficiency in X-linked mental retardation. *Am. J. Hum. Genet.* **75**, 97–105 (2004).
36. Creatine replacement therapy in guanidineoacetate methyltransferase deficiency, a novel inborn error of metabolism. *Lancet* **348**, 789–790 (1996).

37. Almeida, L. S. *et al.* A prevalent pathogenic GAMT mutation (c.59G>C) in Portugal. *Mol. Genet. Metab.* **91**, 1–6 (2007).

38. Schulze, A. *et al.* Therapeutic trial of arginine restriction in creatine deficiency syndrome. *Eur. J. Pediatr.* **157**, 606–607 (1998).

39. Mercimek-Mahmutoglu, S. *et al.* GAMT deficiency: features, treatment, and outcome in an inborn error of creatine synthesis. *Neurology* **67**, 480–484 (2006).

40. Stöckler, S., Marescau, B., De Deyn, P. R., Trijbels, J. M. F. & Hanefeld, F. Guanidino compounds in guanidinoacetate methyltransferase deficiency, a new inborn error of creatine synthesis. *Metabolism* **46**, 1189–1193 (1997).

41. Cross-talk between guanidinoacetate neurotoxicity, memory and possible neuroprotective role of creatine. *Biochimica et Biophysica Acta (BBA) - Molecular Basis of Disease* **1865**, 165529 (2019).

42. Schulze, A. *et al.* Presymptomatic treatment of neonatal guanidinoacetate methyltransferase deficiency. *Neurology* **67**, 719–721 (2006).

43. Schulze, A. & Battini, R. Pre-symptomatic treatment of creatine biosynthesis defects. *Subcell. Biochem.* **46**, 167–181 (2007).

44. Ndika, J. D. T. *et al.* Developmental progress and creatine restoration upon long-term creatine supplementation of a patient with arginine:glycine amidinotransferase deficiency. *Mol. Genet. Metab.* **106**, 48–54 (2012).

45. Nouioua, S. *et al.* Creatine deficiency syndrome. A treatable myopathy due to arginine-glycine amidinotransferase (AGAT) deficiency. *Neuromuscul. Disord.* **23**, 670–674 (2013).

46. Bianchi, M. C. *et al.* Reversible brain creatine deficiency in two sisters with normal blood creatine level. *Ann. Neurol.* **47**, 511–513 (2000).

47. Battini, R. *et al.* Arginine:glycine amidinotransferase (AGAT) deficiency in a newborn: early treatment can prevent phenotypic expression of the disease. *J. Pediatr.* **148**, 828–830 (2006).

48. Cecil, K. M. *et al.* Irreversible brain creatine deficiency with elevated serum and urine creatine: a creatine transporter defect? *Ann. Neurol.* **49**, 401–404 (2001).

49. Salomons, G. S. *et al.* X-linked creatine-transporter gene (SLC6A8) defect: a new creatine-deficiency syndrome. *Am. J. Hum. Genet.* **68**, 1497–1500 (2001).

50. Stockler, S., Schutz, P. W. & Salomons, G. S. Cerebral creatine deficiency syndromes: clinical aspects, treatment and pathophysiology. *Subcell. Biochem.* **46**, 149–166 (2007).

51. deGrauw, T. J. *et al.* Congenital creatine transporter deficiency. *Neuropediatrics* **33**, 232–238 (2002).

52. van de Kamp, J. M. *et al.* Phenotype and genotype in 101 males with X-linked creatine transporter deficiency. *J. Med. Genet.* **50**, 463–472 (2013).

53. Mancini, G. M. S. *et al.* Two novel mutations in SLC6A8 cause creatine transporter defect and distinctive X-linked mental retardation in two unrelated Dutch families. *Am. J. Med. Genet. A* **132A**, 288–295 (2005).

54. Skelton, M. R. *et al.* Creatine transporter (CrT; Slc6a8) knockout mice as a model of human CrT deficiency. *PLoS One* **6**, e16187 (2011).

55. deGrauw, T. J. *et al.* The clinical syndrome of creatine transporter deficiency. *Mol. Cell. Biochem.* **244**, 45–48 (2003).

56. Edvardson, S. *et al.* l-arginine:glycine amidinotransferase (AGAT) deficiency: clinical presentation and response to treatment in two patients with a novel mutation. *Mol. Genet. Metab.* **101**, 228–232 (2010).

57. Mercimek-Mahmutoglu, S. *et al.* Treatment of intractable epilepsy in a female with SLC6A8 deficiency. *Molecular Genetics and Metabolism* vol. 101 409–412 (2010).

58. Hahn, K. A. *et al.* X-linked mental retardation with seizures and carrier manifestations is caused by a mutation in the creatine-transporter gene (SLC6A8) located in Xq28. *Am. J. Hum. Genet.* **70**, 1349–1356 (2002).

59. Kleefstra, T. *et al.* Progressive intestinal, neurological and psychiatric problems in two adult males with cerebral creatine deficiency caused by an SLC6A8 mutation. *Clin. Genet.* **68**, 379–381 (2005).

60. Almeida, L. S. *et al.* Creatine and guanidinoacetate: diagnostic markers for inborn errors in creatine biosynthesis and transport. *Mol. Genet. Metab.* **82**, 214–219 (2004).

61. Salomons, G. S. *et al.* X-linked creatine transporter defect: an overview. *J. Inherit. Metab. Dis.* **26**, 309–318 (2003).

62. Schulze, A. *et al.* Lack of creatine in muscle and brain in an adult with GAMT deficiency. *Annals of Neurology* vol. 53 248–251 (2003).

63. Verhoeven, N. M., Salomons, G. S. & Jakobs, C. Laboratory diagnosis of defects of creatine biosynthesis and transport. *Clin. Chim. Acta* **361**, 1–9 (2005).

64. Cognat, S. *et al.* Determination of guanidinoacetate and creatine in urine and plasma by liquid chromatography-tandem mass spectrometry. *Clin. Chem.* **50**, 1459–1461 (2004).

65. Arias, A., Garcia-Villoria, J. & Ribes, A. Guanidinoacetate and creatine/creatinine levels in controls and patients with urea cycle defects. *Mol. Genet. Metab.* **82**, 220–223 (2004).

66. Verhoeven, N. M. *et al.* Diagnostic enzyme assay that uses stable-isotope-labeled

substrates to detect L-arginine:glycine amidinotransferase deficiency. *Clin. Chem.* **49**, 803–805 (2003).

67. Verhoeven, N. M. *et al.* Enzyme assay for diagnosis of guanidinoacetate methyltransferase deficiency. *Clin. Chem.* **50**, 441–443 (2004).
68. Sijens, P. E., Verbruggen, K. T., Oudkerk, M., van Spronsen, F. J. & Soorani-Lunsing, R. J. 1H MR spectroscopy of the brain in Cr transporter defect. *Mol. Genet. Metab.* **86**, 421–422 (2005).
69. Michaelis, T., Boretius, S. & Frahm, J. Localized proton MRS of animal brain in vivo: Models of human disorders. *Progress in Nuclear Magnetic Resonance Spectroscopy* vol. 55 1–34 (2009).
70. van de Kamp, J. M. *et al.* Clinical features and X-inactivation in females heterozygous for creatine transporter defect. *Clin. Genet.* **79**, 264–272 (2011).
71. Bizzi, A. *et al.* X-linked creatine deficiency syndrome: a novel mutation in creatine transporter gene SLC6A8. *Ann. Neurol.* **52**, 227–231 (2002).
72. Dezortova, M. *et al.* 1H MR spectroscopy as a diagnostic tool for cerebral creatine deficiency. *MAGMA* **21**, 327–332 (2008).
73. Mancardi, M. M. *et al.* Severe epilepsy in X-linked creatine transporter defect (CRTR-D). *Epilepsia* **48**, 1211–1213 (2007).
74. Póo-Argüelles, P. *et al.* X-Linked creatine transporter deficiency in two patients with severe mental retardation and autism. *J. Inherit. Metab. Dis.* **29**, 220–223 (2006).
75. Schiaffino, M. C. *et al.* X-linked creatine transporter deficiency: clinical description of a patient with a novel SLC6A8 gene mutation. *Neurogenetics* **6**, 165–168 (2005).
76. Valayannopoulos, V. *et al.* Treatment by oral creatine, L-arginine and L-glycine in six severely affected patients with creatine transporter defect. *J. Inherit. Metab. Dis.*

**35**, 151–157 (2012).

77. Cheillan, D. *et al.* Screening for primary creatine deficiencies in French patients with unexplained neurological symptoms. *Orphanet J. Rare Dis.* **7**, 96 (2012).
78. Betsalel, O. T. *et al.* Detection of variants in SLC6A8 and functional analysis of unclassified missense variants. *Mol. Genet. Metab.* **105**, 596–601 (2012).
79. Betsalel, O. T. *et al.* Characterization of novel SLC6A8 variants with the use of splice-site analysis tools and implementation of a newly developed LOVD database. *Eur. J. Hum. Genet.* **19**, 56–63 (2011).
80. van de Kamp, J. M. *et al.* Genotype-phenotype correlation of contiguous gene deletions of SLC6A8, BCAP31 and ABCD1. *Clin. Genet.* **87**, 141–147 (2015).
81. Chilosi, A. *et al.* Treatment withl-Arginine improves neuropsychological disorders in a child with Creatine transporter defect. *Neurocase* vol. 14 151–161 (2008).
82. Dunbar, M., Jaggumantri, S., Sargent, M., Stockler-Ipsiroglu, S. & van Karnebeek, C. D. M. Treatment of X-linked creatine transporter (SLC6A8) deficiency: systematic review of the literature and three new cases. *Mol. Genet. Metab.* **112**, 259–274 (2014).
83. Jaggumantri, S. *et al.* Treatment of Creatine Transporter (SLC6A8) Deficiency With Oral S-Adenosyl Methionine as Adjunct to L-arginine, Glycine, and Creatine Supplements. *Pediatr. Neurol.* **53**, 360–363.e2 (2015).
84. Stockebrand, M. *et al.* A Mouse Model of Creatine Transporter Deficiency Reveals Impaired Motor Function and Muscle Energy Metabolism. *Front. Physiol.* **9**, 773 (2018).
85. Baroncelli, L. *et al.* A novel mouse model of creatine transporter deficiency. *F1000Res.* **3**, 228 (2014).

86. Udobi, K. C. *et al.* Deletion of the creatine transporter gene in neonatal, but not adult, mice leads to cognitive deficits. *J. Inherit. Metab. Dis.* **42**, 966–974 (2019).

87. Russell, A. P. *et al.* Creatine transporter (SLC6A8) knockout mice display an increased capacity for in vitro creatine biosynthesis in skeletal muscle. *Front. Physiol.* **5**, 314 (2014).

88. Kurosawa, Y. *et al.* Cyclocreatine treatment improves cognition in mice with creatine transporter deficiency. *J. Clin. Invest.* **122**, 2837–2846 (2012).

89. Molinaro, A. *et al.* A Nervous System-Specific Model of Creatine Transporter Deficiency Recapitulates the Cognitive Endophenotype of the Disease: a Longitudinal Study. *Sci. Rep.* **9**, 62 (2019).

90. Udobi, K. C. *et al.* Cognitive deficits and increases in creatine precursors in a brain-specific knockout of the creatine transporter gene Slc6a8. *Genes Brain Behav.* **17**, e12461 (2018).

91. Kim, D. W. *et al.* Effects of creatine and β-guanidinopropionic acid and alterations in creatine transporter and creatine kinases expression in acute seizure and chronic epilepsy models. *BMC Neurosci.* **11**, 141 (2010).

92. Ullio-Gamboa, G. *et al.* Dodecyl creatine ester-loaded nanoemulsion as a promising therapy for creatine transporter deficiency. *Nanomedicine* **14**, 1579–1593 (2019).

93. Nelson, C. A., 3rd & McCleery, J. P. Use of event-related potentials in the study of typical and atypical development. *J. Am. Acad. Child Adolesc. Psychiatry* **47**, 1252–1261 (2008).

94. Lloyd-Fox, S., Blasi, A. & Elwell, C. E. Illuminating the developing brain: the past, present and future of functional near infrared spectroscopy. *Neurosci. Biobehav. Rev.* **34**, 269–284 (2010).

95. Vanderwert, R. E. & Nelson, C. A. The use of near-infrared spectroscopy in the study of typical and atypical development. *NeuroImage* vol. 85 264–271 (2014).

96. Bowman, L. C. & Varcin, K. J. The Promise of Electroencephalography for Advancing Diagnosis and Treatment in Neurodevelopmental Disorders. *Biol Psychiatry Cogn Neurosci Neuroimaging* **3**, 7–9 (2018).

97. Bosl, W., Tierney, A., Tager-Flusberg, H. & Nelson, C. EEG complexity as a biomarker for autism spectrum disorder risk. *BMC Med.* **9**, 18 (2011).

98. Durand, S. *et al.* NMDA receptor regulation prevents regression of visual cortical function in the absence of Mecp2. *Neuron* **76**, 1078–1090 (2012).

99. LeBlanc, J. J. *et al.* Visual evoked potentials detect cortical processing deficits in Rett syndrome. *Ann. Neurol.* **78**, 775–786 (2015).

100. Boggio, E. M. *et al.* Visual impairment in FOXG1-mutated individuals and mice. *Neuroscience* **324**, 496–508 (2016).

101. Takarae, Y., Sablich, S. R., White, S. P. & Sweeney, J. A. Neurophysiological hyperresponsivity to sensory input in autism spectrum disorders. *J. Neurodev. Disord.* **8**, 29 (2016).

102. Mazziotti, R. *et al.* Searching for biomarkers of CDKL5 disorder: early-onset visual impairment in CDKL5 mutant mice. *Hum. Mol. Genet.* **26**, 2290–2298 (2017).

103. Lupori, L. *et al.* Site-specific abnormalities in the visual system of a mouse model of CDKL5 deficiency disorder. *Hum. Mol. Genet.* **28**, 2851–2861 (2019).

104. Albani, S. H., McHail, D. G. & Dumas, T. C. Developmental studies of the hippocampus and hippocampal-dependent behaviors: insights from interdisciplinary studies and tips for new investigators. *Neurosci. Biobehav. Rev.* **43**, 183–190 (2014).

105. Etherton, M. R., Blaiss, C. A., Powell, C. M. & Sudhof, T. C. Mouse neurexin-1 deletion causes correlated electrophysiological and behavioral changes consistent with cognitive impairments. *Proceedings of the National Academy of Sciences* vol. 106 17998–18003 (2009).

106. Rothwell, P. E. *et al.* Autism-associated neuroligin-3 mutations commonly impair striatal circuits to boost repetitive behaviors. *Cell* **158**, 198–212 (2014).

107. Fuccillo, M. V. Striatal Circuits as a Common Node for Autism Pathophysiology. *Front. Neurosci.* **10**, 27 (2016).

108. Bano, D., Agostini, M., Melino, G. & Nicotera, P. Ageing, neuronal connectivity and brain disorders: an unsolved ripple effect. *Mol. Neurobiol.* **43**, 124–130 (2011).

109. Leuzzi, V., Mastrangelo, M., Battini, R. & Cioni, G. Inborn errors of creatine metabolism and epilepsy. *Epilepsia* **54**, 217–227 (2013).

110. Bernhardi, R. von, von Bernhardi, R., Bernhardi, L. E. & Eugenín, J. Microglial cell dysregulation in brain aging and neurodegeneration. *Frontiers in Aging Neuroscience* vol. 7 (2015).

111. Matt, S. M. & Johnson, R. W. Neuro-immune dysfunction during brain aging: new insights in microglial cell regulation. *Curr. Opin. Pharmacol.* **26**, 96–101 (2016).

112. Hefendehl, J. K. *et al.* Homeostatic and injury-induced microglia behavior in the aging brain. *Aging Cell* **13**, 60–69 (2014).

113. Lee, S. W., Clemenson, G. D. & Gage, F. H. New neurons in an aged brain. *Behavioural Brain Research* vol. 227 497–507 (2012).

114. Dunlop, R. A., Brunk, U. T. & Rodgers, K. J. Oxidized proteins: mechanisms of removal and consequences of accumulation. *IUBMB Life* **61**, 522–527 (2009).

115. Terman, A. & Brunk, U. T. Oxidative stress, accumulation of biological 'garbage',

and aging. *Antioxid. Redox Signal.* **8**, 197–204 (2006).

116. Assunção, M., Santos-Marques, M. J., Carvalho, F., Lukoyanov, N. V. & Andrade, J. P. Chronic green tea consumption prevents age-related changes in rat hippocampal formation. *Neurobiol. Aging* **32**, 707–717 (2011).
117. Baroncelli, L. *et al.* A mouse model for creatine transporter deficiency reveals early onset cognitive impairment and neuropathology associated with brain aging. *Hum. Mol. Genet.* **25**, 4186–4200 (2016).
118. Trotier-Faurion, A. *et al.* Synthesis and biological evaluation of new creatine fatty esters revealed dodecyl creatine ester as a promising drug candidate for the treatment of the creatine transporter deficiency. *J. Med. Chem.* **56**, 5173–5181 (2013).
119. Garbati, P. *et al.* Effects of amide creatine derivatives in brain hippocampal slices, and their possible usefulness for curing creatine transporter deficiency. *Neurochem. Res.* **39**, 37–45 (2014).
120. Adriano, E. *et al.* Creatine salts provide neuroprotection even after partial impairment of the creatine transporter. *Neuroscience* **340**, 299–307 (2017).
121. Trotier-Faurion, A. *et al.* Dodecyl creatine ester and lipid nanocapsule: a double strategy for the treatment of creatine transporter deficiency. *Nanomedicine* **10**, 185–191 (2015).
122. Adriano, E. *et al.* Di-acetyl creatine ethyl ester, a new creatine derivative for the possible treatment of creatine transporter deficiency. *Neurosci. Lett.* **665**, 217–223 (2018).
123. Boehm, E. A., Radda, G. K., Tomlin, H. & Clark, J. F. The utilisation of creatine and its analogues by cytosolic and mitochondrial creatine kinase. *Biochimica et Biophysica Acta (BBA) - Bioenergetics* **1274**, 119–128 (1996).

124. Woznicki, D. T. & Walker, J. B. Formation of a supplemental long time-constant reservoir of high energy phosphate by brain in vivo and in vitro and its reversible depletion by potassium depolarization. *J. Neurochem.* **33**, 75–80 (1979).

125. McLaughlin, A. C., Cohn, M. & Kenyon, G. L. Specificity of creatine kinase for guanidino substrates. Kinetic and proton nuclear magnetic relaxation rate studies. *J. Biol. Chem.* **247**, 4382–4388 (1972).

126. Kawaguchi, Y., Katsumaru, H., Kosaka, T., Heizmann, C. W. & Hama, K. Fast spiking cells in rat hippocampus (CA1 region) contain the calcium-binding protein parvalbumin. *Brain Res.* **416**, 369–374 (1987).

127. Kawaguchi, Y. & Kubota, Y. GABAergic cell subtypes and their synaptic connections in rat frontal cortex. *Cereb. Cortex* **7**, 476–486 (1997).

128. Goldman-Rakic, P. S. The 'psychic' neuron of the cerebral cortex. *Ann. N. Y. Acad. Sci.* **868**, 13–26 (1999).

129. Markram, H. *et al.* Interneurons of the neocortical inhibitory system. *Nature Reviews Neuroscience* vol. 5 793–807 (2004).

130. Kann, O. The interneuron energy hypothesis: Implications for brain disease. *Neurobiol. Dis.* **90**, 75–85 (2016).

131. Somogyi, P. A specific 'axo-axonal' interneuron in the visual cortex of the rat. *Brain Res.* **136**, 345–350 (1977).

132. Hashemi, E., Ariza, J., Rogers, H., Noctor, S. C. & Martínez-Cerdeño, V. The Number of Parvalbumin-Expressing Interneurons Is Decreased in the Prefrontal Cortex in Autism. *Cereb. Cortex* **27**, 1931–1943 (2017).

133. Nakamura, T. *et al.* Relationships among parvalbumin-immunoreactive neuron density, phase-locked gamma oscillations, and autistic/schizophrenic symptoms in

PDGFR-β knock-out and control mice. *PLoS One* **10**, e0119258 (2015).

134. Kobayashi, M., Hayashi, Y., Fujimoto, Y. & Matsuoka, I. Decreased parvalbumin and somatostatin neurons in medial prefrontal cortex in BRINP1-KO mice. *Neurosci. Lett.* **683**, 82–88 (2018).

135. Gogolla, N. *et al.* Common circuit defect of excitatory-inhibitory balance in mouse models of autism. *J. Neurodev. Disord.* **1**, 172–181 (2009).

136. Wöhr, M. *et al.* Lack of parvalbumin in mice leads to behavioral deficits relevant to all human autism core symptoms and related neural morphofunctional abnormalities. *Transl. Psychiatry* **5**, e525 (2015).

137. Jiang, X., Lachance, M. & Rossignol, E. Involvement of cortical fast-spiking parvalbumin-positive basket cells in epilepsy. *Prog. Brain Res.* **226**, 81–126 (2016).

138. Wang, Y. *et al.* Pharmaco-genetic therapeutics targeting parvalbumin neurons attenuate temporal lobe epilepsy. *Neurobiol. Dis.* **117**, 149–160 (2018).

139. Wong, J. C. & Escayg, A. From DREADD to Treatment in Temporal Lobe Epilepsy. *Epilepsy Curr.* **19**, 47–48 (2019).

140. Hippenmeyer, S. *et al.* A developmental switch in the response of DRG neurons to ETS transcription factor signaling. *PLoS Biol.* **3**, e159 (2005).

141. Matthews, R. T. *et al.* Creatine and cyclocreatine attenuate MPTP neurotoxicity. *Exp. Neurol.* **157**, 142–149 (1999).

142. Sullivan, P. G., Geiger, J. D., Mattson, M. P. & Scheff, S. W. Dietary supplement creatine protects against traumatic brain injury. *Ann. Neurol.* **48**, 723–729 (2000).

143. Bender, A. *et al.* Creatine improves health and survival of mice. *Neurobiol. Aging* **29**, 1404–1411 (2008).

144. O'Gorman, E. *et al.* The role of creatine kinase in inhibition of mitochondrial

permeability transition. *FEBS Lett.* **414**, 253–257 (1997).

145. Kempermann, G. Activity Dependency and Aging in the Regulation of Adult Neurogenesis. *Cold Spring Harb. Perspect. Biol.* **7**, (2015).
146. Bartsch, T. & Wulff, P. The hippocampus in aging and disease: From plasticity to vulnerability. *Neuroscience* vol. 309 1–16 (2015).
147. Christian, K. M., Song, H. & Ming, G.-L. Functions and dysfunctions of adult hippocampal neurogenesis. *Annu. Rev. Neurosci.* **37**, 243–262 (2014).
148. Bories, C., Husson, Z., Guitton, M. J. & De Koninck, Y. Differential balance of prefrontal synaptic activity in successful versus unsuccessful cognitive aging. *J. Neurosci.* **33**, 1344–1356 (2013).
149. McQuail, J. A., Frazier, C. J. & Bizon, J. L. Molecular aspects of age-related cognitive decline: the role of GABA signaling. *Trends Mol. Med.* **21**, 450–460 (2015).
150. Torres, L. & Noel, R. J. Astrocytic expression of HIV-1 viral protein R in the hippocampus causes chromatolysis, synaptic loss and memory impairment. *Journal of Neuroinflammation* vol. 11 (2014).
151. Sierra, A. *et al.* Surveillance, phagocytosis, and inflammation: how never-resting microglia influence adult hippocampal neurogenesis. *Neural Plast.* **2014**, 610343 (2014).
152. Ryan, S. M. & Nolan, Y. M. Neuroinflammation negatively affects adult hippocampal neurogenesis and cognition: can exercise compensate? *Neurosci. Biobehav. Rev.* **61**, 121–131 (2016).
153. Lawler, J. M., Barnes, W. S., Wu, G., Song, W. & Demaree, S. Direct antioxidant properties of creatine. *Biochem. Biophys. Res. Commun.* **290**, 47–52 (2002).
154. Sestili, P. *et al.* Creatine as an antioxidant. *Amino Acids* **40**, 1385–1396 (2011).

155. Höhn, A. & Grune, T. Lipofuscin: formation, effects and role of macroautophagy. *Redox Biol* **1**, 140–144 (2013).

156. Brandenstein, L., Schweizer, M., Sedlacik, J., Fiehler, J. & Storch, S. Lysosomal dysfunction and impaired autophagy in a novel mouse model deficient for the lysosomal membrane protein Cln7. *Human Molecular Genetics* vol. 25 777–791 (2016).

157. Kopra, O. *et al.* A mouse model for Finnish variant late infantile neuronal ceroid lipofuscinosis, CLN5, reveals neuropathology associated with early aging. *Hum. Mol. Genet.* **13**, 2893–2906 (2004).

158. Ahmed, Z. *et al.* Accelerated lipofuscinosis and ubiquitination in granulin knockout mice suggest a role for progranulin in successful aging. *Am. J. Pathol.* **177**, 311–324 (2010).

159. Maccarinelli, F. *et al.* A novel neuroferritinopathy mouse model (FTL 498InsTC) shows progressive brain iron dysregulation, morphological signs of early neurodegeneration and motor coordination deficits. *Neurobiol. Dis.* **81**, 119–133 (2015).

160. Head, E., Lott, I. T., Wilcock, D. M. & Lemere, C. A. Aging in Down Syndrome and the Development of Alzheimer's Disease Neuropathology. *Curr. Alzheimer Res.* **13**, 18–29 (2016).

161. Bosl, W., Tierney, A., Tager-Flusberg, H. & Nelson, C. Response: Infant EEG activity as a biomarker for autism: a promising approach or a false promise? *BMC medicine* vol. 9 60 (2011).

162. Jeste, S. S., Frohlich, J. & Loo, S. K. Electrophysiological biomarkers of diagnosis and outcome in neurodevelopmental disorders. *Curr. Opin. Neurol.* **28**, 110–116

(2015).

163. Orekhova, E. V. *et al.* Excess of high frequency electroencephalogram oscillations in boys with autism. *Biol. Psychiatry* **62**, 1022–1029 (2007).

164. Wang, J. *et al.* Resting state EEG abnormalities in autism spectrum disorders. *J. Neurodev. Disord.* **5**, 24 (2013).

165. Sinclair, D., Oranje, B., Razak, K. A., Siegel, S. J. & Schmid, S. Sensory processing in autism spectrum disorders and Fragile X syndrome-From the clinic to animal models. *Neurosci. Biobehav. Rev.* **76**, 235–253 (2017).

166. Arabadzisz, D., Antal, K., Parpan, F., Emri, Z. & Fritschy, J.-M. Epileptogenesis and chronic seizures in a mouse model of temporal lobe epilepsy are associated with distinct EEG patterns and selective neurochemical alterations in the contralateral hippocampus. *Experimental Neurology* vol. 194 76–90 (2005).

167. Bettus, G. *et al.* Enhanced EEG functional connectivity in mesial temporal lobe epilepsy. *Epilepsy Res.* **81**, 58–68 (2008).

168. Milikovsky, D. Z. *et al.* Theta rhythm alterations – a novel predictive biomarker of epilepsy. *Journal of the Neurological Sciences* vol. 381 86 (2017).

169. Pavlides, C., Greenstein, Y. J., Grudman, M. & Winson, J. Long-term potentiation in the dentate gyrus is induced preferentially on the positive phase of θ-rhythm. *Brain Research* vol. 439 383–387 (1988).

170. Klimesch, W., Doppelmayr, M., Pachinger, T. & Ripper, B. Brain oscillations and human memory: EEG correlates in the upper alpha and theta band. *Neurosci. Lett.* **238**, 9–12 (1997).

171. Jensen, O. & Tesche, C. D. Frontal theta activity in humans increases with memory load in a working memory task. *European Journal of Neuroscience* vol. 15 1395–1399

(2002).

172. Wespatat, V., Tennigkeit, F. & Singer, W. Phase sensitivity of synaptic modifications in oscillating cells of rat visual cortex. *J. Neurosci.* **24**, 9067–9075 (2004).

173. Hasselmo, M. E. What is the function of hippocampal theta rhythm?--Linking behavioral data to phasic properties of field potential and unit recording data. *Hippocampus* **15**, 936–949 (2005).

174. Klimesch, W., Sauseng, P., Hanslmayr, S., Gruber, W. & Freunberger, R. Event-related phase reorganization may explain evoked neural dynamics. *Neurosci. Biobehav. Rev.* **31**, 1003–1016 (2007).

175. Guderian, S., Schott, B. H., Richardson-Klavehn, A. & Düzel, E. Medial temporal theta state before an event predicts episodic encoding success in humans. *Proc. Natl. Acad. Sci. U. S. A.* **106**, 5365–5370 (2009).

176. Summerfield, C. & Egner, T. Expectation (and attention) in visual cognition. *Trends in Cognitive Sciences* vol. 13 403–409 (2009).

177. Uhlhaas, P. J. *et al.* Neural synchrony in cortical networks: history, concept and current status. *Front. Integr. Neurosci.* **3**, 17 (2009).

178. Jensen, O. & Mazaheri, A. Shaping functional architecture by oscillatory alpha activity: gating by inhibition. *Front. Hum. Neurosci.* **4**, 186 (2010).

179. Gola, M., Magnuski, M., Szumska, I. & Wróbel, A. EEG beta band activity is related to attention and attentional deficits in the visual performance of elderly subjects. *Int. J. Psychophysiol.* **89**, 334–341 (2013).

180. Güntekin, B., Emek-Savaş, D. D., Kurt, P., Yener, G. G. & Başar, E. Beta oscillatory responses in healthy subjects and subjects with mild cognitive impairment. *Neuroimage Clin* **3**, 39–46 (2013).

181. Palmer, C., Zapparoli, L. & Kilner, J. M. A New Framework to Explain Sensorimotor Beta Oscillations. *Trends Cogn. Sci.* **20**, 321–323 (2016).

182. Willoughby, J. O. Persistent abnormality detected in the non-ictal electroencephalogram in primary generalised epilepsy. *Journal of Neurology, Neurosurgery & Psychiatry* vol. 74 51–55 (2003).

183. Herrmann, C. & Demiralp, T. Human EEG gamma oscillations in neuropsychiatric disorders. *Clinical Neurophysiology* vol. 116 2719–2733 (2005).

184. Maheshwari, A., Marks, R. L., Yu, K. M. & Noebels, J. L. Shift in interictal relative gamma power as a novel biomarker for drug response in two mouse models of absence epilepsy. *Epilepsia* vol. 57 79–88 (2016).

185. Song, D. Y. *et al.* Beta oscillations in the sensorimotor cortex correlate with disease and remission in benign epilepsy with centrotemporal spikes. *Brain Behav.* **9**, e01237 (2019).

186. Mak, C. S. W. *et al.* Immunohistochemical localisation of the creatine transporter in the rat brain. *Neuroscience* **163**, 571–585 (2009).

187. Giusti, L. *et al.* Brain mitochondrial proteome alteration driven by creatine deficiency suggests novel therapeutic venues for creatine deficiency syndromes. *Neuroscience* **409**, 276–289 (2019).

188. Watts, M. E., Pocock, R. & Claudianos, C. Brain Energy and Oxygen Metabolism: Emerging Role in Normal Function and Disease. *Front. Mol. Neurosci.* **11**, 216 (2018).

189. Karbowski, J. Metabolic constraints on synaptic learning and memory. *J. Neurophysiol.* **122**, 1473–1490 (2019).

190. Tronche, F. *et al.* Disruption of the glucocorticoid receptor gene in the nervous

system results in reduced anxiety. *Nat. Genet.* **23**, 99–103 (1999).

191. Lonetti, G. *et al.* Early environmental enrichment moderates the behavioral and synaptic phenotype of MeCP2 null mice. *Biol. Psychiatry* **67**, 657–665 (2010).
192. Moy, S. S. *et al.* Sociability and preference for social novelty in five inbred strains: an approach to assess autistic-like behavior in mice. *Genes Brain Behav.* **3**, 287–302 (2004).
193. Kaidanovich-Beilin, O., Lipina, T., Vukobradovic, I., Roder, J. & Woodgett, J. R. Assessment of Social Interaction Behaviors. *Journal of Visualized Experiments* (2011) doi:10.3791/2473.
194. McFarlane, H. G. *et al.* Autism-like behavioral phenotypes in BTBR T+tf/J mice. *Genes Brain Behav.* **7**, 152–163 (2008).
195. Alessandrì, M. G., Celati, L., Battini, R., Casarano, M. & Cioni, G. Gas chromatography/mass spectrometry assay for arginine: glycine-amidinotransferase deficiency. *Anal. Biochem.* **343**, 356–358 (2005).
196. Ippolito, D. M. & Eroglu, C. Quantifying synapses: an immunocytochemistry-based assay to quantify synapse number. *J. Vis. Exp.* (2010) doi:10.3791/2270.

# ACKNOWLEDGMENTS

I would like to thank Tommaso Pizzorusso and Laura Baroncelli for giving me the opportunity to work in their lab and for having mentoring and followed me throughout all this experience.

I would also like to thank all the personnel and colleagues at CNR as well as all the new friends found along the way, each one of whom contributed one way or another to my professional and personal growth.

Thanks to all the students and trainees I have followed during these years, for learning is always a two-way process.

A special thanks goes to Annalisa, for too many reasons to tell.

As odd as it sounds, I have to thank Nike and Karsa for purring their way through my anxiety.

And obviously, the last (but not least) thank you, goes to my family and friends, for whom I hope to have more time to spend with in the future.